MICROSTRUCTURE AND DIELECTRIC PROPERTIES OF SOLUTION-DERIVED $(Ba,Sr)TiO_3$ THIN FILMS

Tanja Pečnik

Doctoral Dissertation
Jožef Stefan International Postgraduate School
Ljubljana, Slovenia

Supervisor: Prof. Dr. Barbara Malič, Jožef Stefan Institute, Ljubljana, Slovenia

Evaluation Board:
Assoc. Prof. Dr. Vid Bobnar, Chair, Jožef Stefan Institute, Ljubljana, Slovenia

Asst. Prof. Dr. Goran Dražić, Member, Jožef Stefan Institute, Ljubljana, Slovenia, National Institute of Chemistry, Ljubljana, Slovenia

Dr. Theodor Schneller, Member, Rheinisch-Westfälische Technische Hochschule, Institut für Werkstoffe der Elektrotechnik II, Aachen, Germany

MEDNARODNA PODIPLOMSKA ŠOLA JOŽEFA STEFANA
JOŽEF STEFAN INTERNATIONAL POSTGRADUATE SCHOOL



Tanja Pečnik

MICROSTRUCTURE AND DIELECTRIC PROPERTIES OF SOLUTION-DERIVED (Ba,Sr)TiO_3 THIN FILMS

Doctoral Dissertation

MIKROSTRUKTURA IN DIELEKTRIČNE LASTNOSTI TANKIH PLASTI (Ba,Sr)TiO_3, PRIPRAVLJENIH S SINTEZO V RAZTOPINI

Doktorska disertacija

Supervisor: Prof. Dr. Barbara Malič

Ljubljana, Slovenia, July 2016

To my dear ones

Acknowledgments

Undertaking this thesis was a life-changing experience, which would have not been possible without the guidance and support that I received from many people.

First and foremost I would like to express my sincere gratitude to my supervisor Prof. Dr. Barbara Malič for her patient and continuous guidance, support, motivation and the valuable time that she spent for our discussions. Without her immense knowledge I could not have accomplished this thesis and for that I am truly grateful. She gave me the opportunity to work in the Electronic Ceramics Department and to broaden my knowledge by visiting various national and international conferences and foreign laboratories.

My special thanks go to Dr. Sebastjan Glinšek, who helped me during all my PhD years whenever I needed help or advice. Through fruitful discussions he gave me new ideas that helped me during my research work and contribute importantly to the thesis. He is also acknowledged for performing the 2D-XRD analysis of the residual stress in the films.

Brigita Kmet is gratefully acknowledged for her patience and endless help in the laboratory. I also thank her for the preparation of the films for the TEM analysis. My gratitude extends to Jena Cilenšek and Silvo Drnovšek for their help in the laboratory, support and invaluable advice about science and life in general. The help of Asst. Prof. Dr. Andreja Benčan Golob with the TEM analysis and the help of Asst. Prof. Dr. Hana Uršič with the AFM analysis is gratefully acknowledged. I would also like to thank all the other current and former workers at the Electronic Ceramics Department; my current office-mates – Jitka Hreščak, Lovro Fulanović, Maja Makarovič and my former office-mates – Dr. Raluca-Camelia Frunza, Asst. Prof. Dr. Tadej Rojac, Dr. Oleksandr Noschenko. Thanks also to Dr. Katarina Vojisavljević, Aleksander Matavž, Tina Ručigaj, Andraž Bradeško and Evgeniya Khomyakova, as well as to Dr. Alja Kupec, Dr. Tina Bakarič and Dr. Julian Bradley Walker for their discussions and for creating some great memories that I will cherish forever. I also thank the student Maja Peterkovič for all her help with the work in the laboratory and the students Nika Kurinčič, Kristjan Kuhar, Aneja Tuljak and Alen Britvić. I am grateful to all the co-workers at the Electronic Ceramic Department at the Jožef Stefan Institute for being such a good team in terms of work and beyond.

Asst. Prof. Dr. Naonori Sakamoto, Faculty of Engineering/Graduate School of Integrated Science and Technology, Shizuoka University, Japan, is acknowledged for the atomic-resolution STEM analysis.

I would like to thank to Edi Krajnc (National Institute of Chemistry) for the XRD measurements, Prof. Angus I. Kingon (School of Engineering at Brown University, USA) for enabling the use of their 2D-XRD facility, Dr. Andreja Eršte and Assoc. Prof. Dr.

Vid Bobnar (Condensed Matter Physics Department, Jožef Stefan Institute) for the dielectric measurements across a broad frequency range, Dr. Maksim Ivanov and Prof. Dr. Juras Banys (Faculty of Physics, Vilnius University, Lithuania) for their help during my visit to their laboratory and for the dielectric measurements. I also thank to Prof. Dr. Hong Wang and Dr. Feng Xiang (School of Electronic and Information Engineering, Xi'an Jiaotong University, China) for the high-frequency dielectric spectroscopy measurements.

I wish to thank the Slovenian Research Agency, COST SIMUFER Action MP0904 and COST TO-BE Action MP1308 for the funding and to the Centre of Excellence NAMASTE, Condensed Matter Physics Department, Jožef Stefan Institute, Center for Electronic Microscopy at the Jožef Stefan Institute and the National Institute of Chemistry for allowing the use of their laboratory equipment.

The most important acknowledgement goes to my dear ones: to my Marko for his love, endless encouragement and support through the whole of "our" PhD period, to my mother, father and brother, who gave me unconditional love and support and also the opportunity to study and make it that far, and to my auntie and friends for their understanding and patience.
Without all of you none of my professional and personal accomplishments would have been possible.

Abstract

The barium strontium titanate solid solution, $Ba_xSr_{1-x}TiO_3$, is a ferroelectric material suitable for applications in microwave-tunable devices. Its Curie temperature strongly depends on the Ba/Sr ratio, and the compositions that are in the paraelectric phase in the operating temperature range, yet still close to the phase-transition temperature, exhibit high permittivity, high tunability and at the same time also low dielectric losses in the microwave frequency range. But to achieve the above requirements with solution-derived thin films different processing-related film characteristics, i.e., the film thickness, microstructure (grain size and shape, porosity), residual stress, etc., should be considered since they strongly influence the functional response of the films.

The $Ba_{0.5}Sr_{0.5}TiO_3$ (BST 50/50) films with thicknesses in the range from 90 nm to 600 nm were prepared on polycrystalline alumina substrates by repeating the deposition of a hetero-metallic precursor solution by spin-coating, drying, pyrolysis, and rapid thermal annealing steps (multi-step annealing) at 900 °C until the required film thickness has been reached. The microstructure of the films is dense and predominantly columnar. The room-temperature dielectric properties in the kHz and GHz frequency ranges show a non-monotonic film-thickness dependence, which can be divided into three groups. Firstly, for the thicknesses between 90 nm and 170 nm, the dielectric permittivity of the films is controlled by the dielectric grain-size effect; it increases from 650 to 1250 measured at 100 kHz as the grain size increases from ~45 nm to ~80 nm for the 90-nm- and 170-nm-thick films, respectively. For these films a high biaxial tensile stress of ~350 MPa is observed and related to the thermal-expansion mismatch between the film and the substrate. For the film thicknesses between 170 nm and 240 nm, the dielectric permittivity reaches plateau values between 1250 and 1350, corresponding to only a slight change of the grain size from ~80 nm to ~90 nm. In parallel, the tensile stress decreases to 198 MPa. But in the third thickness range the permittivity drops to 770 for the 600-nm-thick film, while the grain size changes only slightly. We ascribe this drop of the permittivity to the existence of intergranular cracks that form as a consequence of the relaxation of the tensile residual stress, which can be explained by the brick-wall model.

In the second part we focus on a study of the crystallization and evolution of the microstructure of BST 50/50 thin films prepared by multi-step annealing at temperatures between 600 °C and 900 °C. The films, consisting of seven layers deposited from the precursor solution, crystallize in a pure perovskite phase after annealing at ~640 °C and have a granular microstructure. The latter forms upon the annealing of individual deposited layers with the individual layer thickness much larger than the grain size, and persists upon annealing up to ~800 °C. Upon annealing at high enough temperatures (≥880 °C) the grain size exceeds the individual layer thickness, resulting in a predominantly columnar microstructure upon repeating the deposition-drying-pyrolysis-annealing steps. The evolution of such a columnar microstructure proceeds via the crystallization and growth of fine, equiaxed grains of 10–20-nm across within an individual, ~40-nm-thick layer on top of pre-existing columnar grains followed by homo-epitaxial overgrowth within each grain.

Povzetek

Feroelektrična trdna raztopina barijevega stroncijevega titanata $Ba_xSr_{1-x}TiO_3$ je primerna za uporabo v mikrovalovnih komponentah, na primer v frekvenčno prilagodljivih antenah. Curiejeva temperatura trdne raztopine je odvisna od razmerja med barijem in stroncijem. Sestave, ki so v paraelektrični fazi pri delovnih temperaturah, vendar še dovolj blizu temperature faznega prehoda, izkazujejo visoko dielektričnost, visoko napetostno prilagodljivost in hkrati tudi nizke dielektrične izgube v mikrovalovnem frekvenčnem območju. Pri tankih plasteh, pripravljenih iz raztopin, moramo upoštevati, da so njihove lastnosti: debelina, mikrostruktura (velikost in oblika zrn, poroznost), napetosti, itd., izrazito odvisne od pogojev priprave, in da močno vplivajo na funkcijski odziv.

Tanke plasti $Ba_{0,5}Sr_{0,5}TiO_3$ (BST 50/50) z debelinami od 90 nm do 600 nm smo pripravili s ponavljanjem stopenj nanašanja tekočega prekurzorja na podlage polikristaliničnega aluminijevega oksida, sušenja, pirolize in hitrega segrevanja pri 900 °C (večstopenjsko segrevanje). Mikrostruktura plasti je gosta in sestavljena iz pretežno stebričastih zrn. Dielektrične lastnosti plasti, izmerjene pri sobni temperaturi v kHz in GHz območju, so nelinearno odvisne od debeline plasti. Dielektričnost plasti z debelinami od 90 nm do 170 nm naraste s 650 na 1250 pri 100 kHz, kar je povezano s povečanjem velikosti zrn s ~45 nm na ~80 nm. Plasti so pod veliko natezno napetostjo, ~350 MPa, ki se razvije med ohlajanjem s temperature segrevanja zaradi razlike v termičnih raztezkih plasti in podlage. V plasteh z debelinami med 170 nm in 240 nm dielektričnost doseže vrednosti med 1250 in 1350, kar je povezano z le majhno spremembo velikosti zrn s ~80 nm na ~90 nm. Hkrati se natezna napetost zmanjša na 198 MPa. Kljub temu, da se velikost zrn v tretji skupini plasti, z debelinami med 240 nm in 600 nm, bistveno ne spreminja, se dielektričnost izrazito zmanjša, za 600 nm debelo plast znaša le 770. Zmanjšanje dielektričnosti pri plasteh z največjimi debelinami pripisujemo prisotnosti razpok med zrni, ki nastanejo kot posledica sproščanja nateznih napetosti, kar lahko razložimo s pomočjo modela opečnatega zidu (angl: »*brick-wall*«).

V drugem delu disertacije smo se osredotočili na študij kristalizacije in razvoja mikrostrukture tankih plasti BST 50/50, pripravljenih z večstopenjskim segrevanjem pri temperaturah od 600 °C do 900 °C. Plasti, pripravljene iz sedmih nanosov, kristalizirajo v čisti perovskitni fazi po segrevanju pri ~640 °C. Mikrostrukturo sestavljajo enakoosna zrna; pri čemer je velikost zrn nekajkrat manjša od debeline posameznega nanosa. Mikrostruktura je značilna za plasti, pripravljene z večstopenjskim segrevanjem pri temperaturah do ~800 °C. Po večstopenjskem segrevanju pri dovolj visokih temperaturah (≥880 °C), ko velikost zrn preseže debelino posameznega nanosa, nastane pretežno stebričasta mikrostruktura. Razvoj takšne mikrostrukture poteka preko kristalizacije in rasti 10-20 nm velikih enakoosnih zrn v posameznem, ~40 nm debelem nanosu na že obstoječem stebričastem zrnu, ki predstavlja podlago za homoepitaksialno preraščanje.

Contents

List of Figures **xv**

List of Tables **xxi**

Abbreviations **xxiii**

Symbols **xxv**

1 Introduction **1**
1.1 Chemical Solution Deposition ... 1
1.1.1 Hybrid process ... 2
1.1.2 Deposition, drying, pyrolysis ... 3
1.1.3 Crystallization and evolution of microstructure ... 4
1.1.4 Grain growth in thin films ... 6
1.1.5 Structural zone model for solution-derived thin films ... 9
1.2 Barium Strontium Titanate ... 12
1.2.1 $Ba_xSr_{1-x}TiO_3$ solid solution ... 12
1.2.2 Thin films ... 14
1.2.2.1 Crystallization and evolution of microstructure ... 16
1.2.2.2 Dielectric properties ... 20

2 Aims and Hypothesis **25**

3 Materials and Methods **27**
3.1 Preparation of the Films ... 27
3.1.1 Synthesis of the solution ... 27
3.1.2 Substrate ... 27
3.1.3 Deposition of the films ... 28
3.1.4 Patterning of planar capacitors by lift-off photolithography ... 29
3.2 Characterization ... 32
3.2.1 X-Ray diffraction ... 32
3.2.1.1 Residual stress analysis ... 32
3.2.2 Scanning electron microscopy ... 33
3.2.3 Atomic force microscopy ... 33
3.2.4 Focused ion beam ... 33
3.2.5 Transmission electron microscopy ... 33
3.2.6 Dielectric spectroscopy ... 34
3.2.6.1 Measurements in the kHz frequency range ... 34
3.2.6.2 Measurements in the GHz frequency range ... 35

4 Results and Discussion **37**
4.1 $Ba_{0.5}Sr_{0.5}TiO_3$ Thin Films with Different Thicknesses ... 37

4.1.1 Microstructure and phase composition 37
4.1.2 Dielectric properties of the films 43
4.2 Crystallization and Evolution of Microstructure of $Ba_{0.5}Sr_{0.5}TiO_3$ Thin Films ... 51
4.2.1 $Ba_{0.5}Sr_{0.5}TiO_3$ Thin Films Prepared at Temperatures between 600 °C and 900 °C 51
4.2.2 Evolution of the Columnar Microstructure of $Ba_{0.5}Sr_{0.5}TiO_3$ Thin Films prepared at 900 °C 61

5 Conclusions **77**

Appendix A Data for structural zone model for solution-derived $BaTiO_3$, $SrTiO_3$ and BST thin films **81**

Appendix B Analysis of the Residual Stress in Thin Films Using 2D XRD Method **83**
B.1 Basic relations 83
B.2 Strain determination by the conventional XRD 84
B.3 Strain and stress determination by the 2D-XRD 87

References **89**

Bibliography **97**

Biography **101**

List of Figures

Figure 1.1:Schematic presentation of the steps of the Chemical Solution Deposition process [7].....2
Figure 1.2: In the case of heterogeneous nucleation the nuclei (orange) grow from the substrate/film or film/atmosphere interfaces, while in the case of homogeneous nucleation the nuclei form randomly in the amorphous matrix of the film (blue).....4
Figure 1.3: Free-energy diagram for homogeneous (blue line) and heterogeneous nucleation (orange line) explaining the existence of a critical nucleus size [12].....5
Figure 1.4: Schematic presentation of prevailing a) homogeneous and b) heterogeneous nucleation and the resulting cross-sectional microstructures.....6
Figure 1.5:Increasing average grain size with time t during the normal grain growth process [19].....7
Figure 1.6: SEM micrographs of TiO_2 thin films with thicknesses of 65 nm and 140 nm annealed at a), b) 700 °C, c), d) 800 °C and e), f) 900 °C [22].....7
Figure 1.7: a) Film roughness of the Au surface plotted as a function of the grain size of the film and annealing temperature.....8
Figure 1.8: a) Evolution of the fine granular microstructure of the films when the nucleation rate is high and the growth rate is low.....9
Figure 1.9: Structural zone model for the films prepared by physical deposition proposed by Thornton [26]. T_M – melting temperature.....9
Figure 1.10:a) ICS plotted as a function of SLT after the model proposed by Schuler et al. [28]. b) 3D graph, where ICS/SLT is plotted as a function of temperature (T_S/T_M)..11
Figure 1.11:Schematic presentation of the changes in a perovskite material which transforms from a paraelectric cubic into the ferroelectric tetragonal phase at the phase-transition temperature T_C.....12
Figure 1.12:Temperature dependence of the dielectric constant of $Ba_xSr_{1-x}TiO_3$ ceramics with different Ba concentration x [38].....13
Figure 1.13:Permittivity dependence versus applied electric field for the paraelectric phase [39].....14
Figure 1.14:XRD spectra of $BaTiO_3$ (BTO), $Ba_{0.7}Sr_{0.3}TiO_3$ (BST 70/30) and $SrTiO_3$ (STO) thin films prepared at 600 °C for BTO and STO and at 550 °C for BST 70/30.....16
Figure 1.15:Granular microstructure of solution-derived, alkaline-earth titanate thin films.....17
Figure 1.16:SEM cross-section and surface microstructures of the $BaTiO_3$ and $SrTiO_3$ thin films prepared from solutions with different concentrations ranging from 0.1 to 0.3 M by the multiple-step annealing process.....18
Figure 1.17: TEM cross-section micrographs of the columnar microstructure of a) $SrTiO_3$ and b) $BaTiO_3$ thin films prepared on $Pt/ZrO_2/SiO_2/Si$ substrates by the multi-step annealing process.....19

Figure 1.18: a) Intrinsic crystallite size (ICS) versus single layer thickness (SLT) and b) ICS/SLT versus T_{anneal}/T_{melt} for different $BaTiO_3$, $SrTiO_3$ and BST thin films according to the model proposed by Schuler et al. [28]. T_{anneal} – annealing temperature (K), T_M – melting temperature (K). The details of the films collected in the figure, are collected in Appendix A. Note that it is assumed that ICS is equal to the grain size. 20

Figure 1.19:a) Temperature dependence of the dielectric permittivity and losses of $BaTiO_3$ ceramics with grain sizes in the range from 0.07 µm to 1.7 µm. b) Schematics of the brick-wall model consisting of the low-permittivity grain-boundary layer and high-permittivity grain interiors [63]. 21

Figure 1.20:Temperature-dependent dielectric permittivity of $BaTiO_3$ thin films with grain sizes from 80 nm to 150 nm, prepared at different annealing temperatures [66]. 22

Figure 1.21:Thickness-dependent grain size (GS) for $Ba_{0.5}Sr_{0.5}TiO_3$ thin films prepared by PLD. Inset of the graph represents the dielectric properties of the films measured at 100 kHz [46]. 23

Figure 1.22:a) Relative dielectric constant measured at 0 kV and 300 kV and b) dielectric tunability under different applied electric field amplitudes for BST 50/50 films deposited on different substrates as a function of the thermal expansion coefficient (TEC) of the substrate [44]. 23

Figure 3.1:XRD pattern of an alumina substrate and BST 50/50 film deposited on such a substrate. 28

Figure 3.2: Schematic presentation of the thin-film deposition. a) In the two-step annealing process the first layer was deposited, dried, pyrolyzed and annealed for 15 min. 29

Figure 3.3: Schematic presentation of the basic processing steps for patterning of the planar capacitor electrodes by lift-off photolithography. Optical micrographs of a part of the planar capacitor structure after the developing step (6.), after sputtering of Cr/Au (7.) and after the final lift-off process (8.). 30

Figure 3.4: a) A photograph of the mask for the photolithography process with the patterns of the planar capacitor electrodes. b) Enlarged optical micrograph of the pattern of the planar capacitor electrodes used in this thesis and c) schematics showing the dimensions of the used electrodes. 31

Figure 3.5: Schematic presentation of a planar thin-film capacitor. h_f and h_s – thickness of the film and the substrate, respectively; s – gap between the electrodes; l – length of the electrodes; w – width of the electrodes. *After* [84]. 34

Figure 4.1: The FE-SEM cross-section and surface micrographs of the BST 50/50 films with the thicknesses between 90 nm and 600 nm. 38

Figure 4.2: XRD patterns of the BST 50/50 films with the thicknesses between 90 nm and 600 nm, prepared on alumina substrates by multi-step annealing at 900 °C. 39

Figure 4.3: The (100), (110), (111) and (200) diffraction peaks of BST 50/50 thin films with thicknesses between 90 nm and 600 nm. 40

Figure 4.4: a) The 2D-XRD frames of the 170-nm-thick BST 50/50 film measured at different tilting ψ-angles, shown in the -62 ° to -116 ° γ-range, where γ is used to define the direction of the diffracted beam on the cone. 41

Figure 4.5: Schematics showing the tensile thermal stress induced in the BST 50/50 film on an alumina substrate due to the difference in the thermal expansion coefficients (TECs) of the film and the substrate. 42

Figure 4.6: FE-SEM surface microstructures of the 310-nm- and 490-nm-thick BST 50/50 films. The arrows mark the cracks in the films. 42

Figure 4.7: The dielectric permittivity ε`and dielectric losses $Tan\delta$ of the BST 50/50 thin films with the thicknesses between 90 nm and 600 nm, measured at 100 kHz, 10 GHz, 15 GHz and at room temperature. 43
Figure 4.8: The average lateral grain size GS, residual stress σ and the kHz-range dielectric permittivity ε`, extracted from Figure 4.7, plotted against the film thickness.....44
Figure 4.9:Temperature dependence of the dielectric permittivity of the BST 50/50 films with thicknesses in the range from a) 90 nm to 240 nm and b) from 310 nm to 600 nm, measured at 5 kHz. 45
Figure 4.10:Temperature dependence of the dielectric permittivity of the a) 90-nm-thick and b) 600-nm-thick BST 50/50 films measured in the frequency range from 3 kHz to 500 kHz.....46
Figure 4.11:Temperature dependence of the a) dielectric permittivity and b) dielectric losses of the 90-, 150-, 240- and 310-nm-thick BST 50/50 films, all measured at 15 GHz. 47
Figure 4.12:The grain size dependence of the dielectric permittivity of $BaTiO_3$ films from the work of Aygün et al. [56] compared to the data from the literature for various $BaTiO_3$, $SrTiO_3$, BST, $BaTi_xHf_{1-x}O_3$ (x=0-25) and $BaTi_{1-x}Zr_xO_3$ (x=0-25) ceramics and thin films. 48
Figure 4.13: Permittivity-voltage curves measured in the +40 V to -40 V range at 100 kHz for the a) 90-, 115-, 150-, 170-, 210-, 240-nm-thick films and for the b) 310-, 400-, 490- and 600-nm-thick films. 50
Figure 4.14:XRD patterns of the BST 50/50 films on alumina substrates annealed at temperatures between 600 °C and 900 °C.....52
Figure 4.15:FE-SEM cross-section micrographs of the BST 50/50 films on alumina substrates annealed at a) 600 °C, b) 640 °C, c) 680 °C, d) 720 °C, e) 760 °C and f) 800 °C. 53
Figure 4.16:a) and d) bright-field TEM cross-section micrographs of the BST 50/50 films on alumina substrates annealed at 700 °C and 800 °C. The grains are encircled with full lines, the dotted lines mark the thickness of individual deposited layers and the arrow marks the pore in the film. 54
Figure 4.17:FE-SEM cross-section and surface micrographs of the BST 50/50 films on alumina substrates annealed at a), b) 840 °C, c), d) 880 °C and e), f) 900 °C.....55
Figure 4.18:The film thickness and average grain size GS of the BST 50/50 films plotted as a function of the annealing temperature (T_{anneal}).....56
Figure 4.19: a) FE-SEM cross-section micrograph of the BST 30/70 thin film prepared by the multi-step annealing process at 700 °C on a Pt/Si substrate from the 0.125-M coating solution. The lines mark the shape of the columns, consisting of many equiaxed grains. b) FE-SEM cross-section micrograph of the BST 50/50 film prepared by the multi-step annealing process at 700 °C from the 0.25-M solution.....58
Figure 4.20: The FE-SEM cross-section micrographs of the BST 50/50 films prepared by the two-step annealing process at a) 700 °C and b) 900 °C. The time in the brackets denotes the annealing time of the six deposited layers. 58
Figure 4.21: The structural-zone model for the solution-derived $BaTiO_3$, $SrTiO_3$ and BST thin films plotted as the intrinsic crystallite size (ICS) versus single-layer thickness (SLT) (open symbols), re-plotted from Figure 1.18.....59
Figure 4.22: XRD patterns of the BST 50/50 1L films on alumina substrates annealed at 900 °C for 1 min to 60 min [95]. 61

Figure 4.23:FE-SEM cross-section and surface micrographs of the 1L BST 50/50 films annealed at 900 °C for a), b) 1 min, c), d) 5 min, e), f) 15 min and g), h) 60 min [95]... 62
Figure 4.24:FE-SEM cross-section and surface micrographs of the a) and b) 2L BST 50/50 film annealed at 900 °C and the time of annealing of the last deposited layer a) and b) 5 min and c) and d) 60 min. 63
Figure 4.25:a) Cross-section bright-field TEM micrograph of the 2L (60 min) film. Individual grains are encircled with dotted lines..... 65
Figure 4.26:FE-SEM cross-section and surface micrographs of the BST 50/50 a), b) 3L (5 min) and c), d) 3L (60 min) films, annealed at 900 °C with different times of the annealing for the last deposited layer..... 66
Figure 4.27:FE-SEM cross-section and surface micrographs of the 6L (5 min) film, annealed at 900 °C with the time of the annealing of the last deposited layer equal to 5 min. 67
Figure 4.28:FE-SEM cross-section and surface micrographs of the BST 50/50 a) 7L (1 s), b) 7L (1 min), c) 7L (5 min) and d) 7L (60 min) films, annealed at 900 °C with different times of annealing for the last deposited layer. 68
Figure 4.29: AFM topography images (left: height, right: deflection) of the template, 7L (1 s), 7L (1 min), 7L (5 min) and 7L (60 min) films. 70
Figure 4.30: AFM surface profiles of the template film, 7L (1 s), 7L (1 min), 7L (5 min) and 7L (60 min) films. Vertical lines represent the grain boundaries. The root-mean-square (RMS) roughness calculated for an area of 1 µm × 1 µm shown in Figure 4.29. 71
Figure 4.31: a) Bright-field TEM cross-section micrograph of the 7L (60 min) BST 50/50 film annealed at 900 °C. The columnar grain is encircled. b) Bright-field STEM and c) dark-field STEM micrographs showing a representative columnar grain. 72
Figure 4.32:The average lateral grain size of the BST 50/50 films plotted as a function of the number of layers and the corresponding thicknesses of the films (FT). The time of the final annealing at 900 °C was, in all cases, 60 min..... 73
Figure 4.33:a) The ratio of the average lateral grain size (GS) and the film thickness (FT) plotted versus the number of deposited BST 50/50 layers. b) GS/SLT ratio plotted as a function of the number of deposited layers. The time of the final annealing at 900 °C was in all cases 60 min. 75
Figure 4.34:FE-SEM cross-section and surface micrographs of the a), b) 2L (60 min + 480 min) and 4L (60 min + 480 min) films, annealed at 900 °C with the time of the annealing for the last deposited layer being 60 min and additionally 480 min. 75

Figure B.1:Stress components (σ_{ij}) in thin film on the substrate. 84
Figure B.2:Schematic presentation of the strain-measurement geometry in the conventional X-ray diffration in the sample coordinates $S_1S_2S_3$ [82]. 85
Figure B.3:Schematics of the XRD pattern of the (110) diffraction peak of the BST 50/50 film, obtained from the measurement by the conventional XRD. Shifting of the peak position due to the a) tensile and b) compressive stress. 85
Figure B.4:The $\varepsilon\phi\psi$- $sin^2\psi$ plot obtained during the XRD-strain measurement of the sample with tensile biaxial residual stress. *After* [82]..... 86
Figure B.5:The $\varepsilon\phi\psi$- $sin^2\psi$ curves for non-ideal situations. In the case a) ψ –splitting occurs due to the shear stress, while in the case b) the curve is non linear due to texture, stress gradient and/or composition gradient within the investigated material. *After* [82]. 86

Figure B.6:Schematic presentation of a 2D-XRD system with diffraction cones from an unstressed polycrystalline sample and the diffraction cones, that are distorted by the stress [100]. 87
Figure B.7:a) Debye diffraction rings collected in a -62 ° to -116 ° γ-range using an area detector for a BST 50/50 film on polycrystalline alumina substrate. b) Conventional XRD pattern in a narrow 2θ region around the (110) diffraction peak obtained with the integration within the shown γ-range. 88

List of Tables

Table 1.1: Overview of the literature reports on CSD of (Ba,Sr)TiO_3 thin films. The selected films were prepared by spin-coating. (C_M – molar concentration of the coating solution, T_P – pyrolysis temperature, T_{anneal} – annealing temperature, two-step – drying and/or pyrolysis for each deposited layer followed by annealing, multi-step – drying and/or pyrolysis and annealing of each individual deposited layer separately, *NA* – not available, MBE – Molecular Beam Epitaxy, 2-EOE– 2-ethoxyethanol). 15

Table 3.1: Chemicals used for the synthesis of the BST 50/50 solution. 27

Table 4.1: Biaxial tensile stress of the BST 50/50 films with thicknesses in the range from 90 nm to 600 nm, as determined with the 2D $sin^2\psi$ technique. 42

Table 4.2: The tunability n, expressed as the ratio of the permittivities at 0 V and 40 V, and the relative tunability n_r of the BST 50/50 films with different film thickness, measured at 100 kHz and room temperature. 50

Table 4.3: The crystallite size and Lotgering factor of the BST 50/50 films annealed at temperatures between 640 °C and 900 °C.....52

Abbreviations

AC	... alternating current
ADF	... annular dark-field
AFM	... atomic force microscope
BST	... $Ba_xSr_{1-x}TiO_3$ (x=0-1)
BST 30/70	... $Ba_{0.3}Sr_{0.7}TiO_3$
BST 40/60	... $Ba_{0.4}Sr_{0.6}TiO_3$
BST 50/50	... $Ba_{0.5}Sr_{0.5}TiO_3$
BTO	... $BaTiO_3$
CSD	... chemical solution deposition
DC	... direct current
DF	... dark-field
EDXS	... energy-dispersive X-ray spectroscopy
FE-SEM	... field-emission scanning electron microscope
FIB	... focused ion beam
FTIR	... Fourier transform infrared spectroscopy
FWHM	... full width at half maximum
HAADF	... high-angle annular dark-field
ICS	... intrinsic crystallite size
IP	... intermediate phase
JCPDS	... Joint committee on powder-diffraction standards
KNN	... $K_{0.5}Na_{0.5}NbO_3$
MBE	... molecular beam epitaxy
MOCVD	... metal-organic chemical vapor deposition
NA	... not available
NMP	... N-methyl-2-pyrrolidone
PCM	... partial capacitance method
PLD	... pulsed-laser deposition
PVD	... physical vapor deposition
PZT	... $Pb(Zr_{0.3}Ti_{0.7})O_3$
RMS	... root-mean-squared roughness
RTA	... rapid thermal annealing
SEM	... scanning electron microscope
SLT	... single layer thickness
STEM	... scanning transmission electron microscope
STM	... scanning tunneling microscope
STO	... $SrTiO_3$
TEC	... thermal expansion coefficient
TEM	... transmission electron microscope
UV	... ultraviolet
XRD	... X-ray diffraction

2-EOE . . . 2-ethoxyethanol
2-MOE . . . 2-methoxyethanol
1L (1 min) . . . films consisting of one deposited layer, annealed for 1 min
1L (5 min) . . . films consisting of one deposited layer, annealed for 5 min
1L (15 min) . . . films consisting of one deposited layer, annealed for 15 min
1L (30 min) . . . films consisting of one deposited layer, annealed for 30 min
1L (60 min) . . . films consisting of one deposited layer, annealed for 60 min
2L (5 min) . . . films consisting of two deposited layers, the last one annealed for 5 min
2L (60 min) . . . films consisting of two deposited layers, the last one annealed for 60 min
3L (5 min) . . . films consisting of three deposited layers, the last one annealed for 5 min
3L (60 min) . . . films consisting of three deposited layers, the last one annealed for 60 min
4L (5 min) . . . films consisting of four deposited layers, the last one annealed for 5 min
4L (60 min) . . . films consisting of four deposited layers, the last one annealed for 60 min
6L (5 min) . . . films consisting of six deposited layers, the last one annealed for 5 min
7L (1 s) . . . films consisting of seven deposited layers, the last one annealed for 1 s
7L (1 min) . . . films consisting of seven deposited layers, the last one annealed for 1 min
7L (5 min) . . . films consisting of seven deposited layers, the last one annealed for 5 min
7L (60 min) . . . films consisting of seven deposited layers, the last one annealed for 60 min

Symbols

C_M	... molar concentration of the coating solution
d	... lattice spacing
d_0	... lattice spacing of an unstressed crystal
E	... Young's modulus
E	... electric field
E_c	... coercive field
FT	... film thickness
$f_{(00l)}$	... Lotgering factor
GS	... average grain size
h_f	... thickness of the film
h_{ij}	... components of the unit vector in the direction of the measured strain
h_s	... thickness of the substrate
K	... constant related to the crystallite shape
L	... crystallite size
l	... length of the electrodes
m	... slope of the $\varepsilon_{\phi\psi}$-$sin^2\,\psi$ plot
n	... tunability
n_r	... relative tunability
P	... polarization
P_r	... remanent polarization
P_s	... spontaneous polarization
P_0	... ratio between the sum of the intensities of (00l) reflections and (hkl) reflections in a certain 2θ range in a non-oriented material
$P_{(00l)}$	... ratio between the sum of the intensities of (00l) reflections and (hkl) reflections in a certain 2θ range in a oriented material
p_{ij}	... stress coefficients
p_{ph}	... pseudohydrostatic stress coefficient
r	... radius of the nucleus
r^*	... critical radius of the nucleus
$S_1S_2S_3$	... sample coordinates
s	... gap between the electrodes
T	... temperature
T_{anneal}	... annealing temperature
T_C	... Curie point
T_M	... melting temperature
T_P	... pyrolysis temperature
T_S	... sintering temperature
t	... time
$tan\delta$	... dielectric losses
U	... voltage

w ... width of the electrode
β ... full width at half maximum, also referred to as FWHM
γ ... surface energy per unit area
γ ... angle that defines the direction of the diffracted beam on the cone
ΔG ... overall excess free energy
ΔG^* ... energy barrier for nucleation
ΔG^*_{hetero} ... energy barrier for heterogeneous nucleation
ΔG^*_{homo} ... energy barrier for homogeneous nucleation
ΔG_S ... surface excess free energy
ΔG_V ... volume excess free energy
ΔG_v ... free-energy change of crystallization per unit volume
ε' ... dielectric permittivity
ε_{ij} ... strain components
$\varepsilon_{\phi\psi}$ ... strain measured at angles ϕ and ψ
Θ ... contact angle
θ ... diffraction angle
θ_0 ... diffraction angle measured from an unstressed material
λ ... X-ray wavelength
ν ... Poisson's ratio
ν ... frequency
σ_{ij} ... stress components
σ_{ph} ... pseudohydrostatic stress
σ_ϕ ... normal stress
τ_ϕ ... shear stress
ϕ ... angle of rotation of the sample along its normal
ψ ... tilting angle

Chapter 1

Introduction

The first chapter of the thesis is divided into two parts. The Chemical Solution Deposition of thin films is described and followed by the theory of the crystallization and evolution of the microstructure of solution-derived thin films. Secondly a review of the barium strontium titanate (BST) solid solution and thin films is given with the emphasis on the crystallization, microstructure and dielectric properties of the BST films.

1.1 Chemical Solution Deposition

Functional oxide thin films are prepared by physical deposition methods such as evaporation, pulsed laser deposition, sputtering, etc. and by chemical methods, which include Chemical Vapor Deposition and Chemical Solution Deposition (CSD) [1]. CSD is very flexible and has been widely used for the production of amorphous and crystalline thin films for different applications in electronics for more than 30 years. The greatest advantages of CSD are an excellent control of the film's composition at the molecular level, a high deposition rate, deposition over large areas and low investment costs. The main disadvantages of CSD are the difficulties in obtaining epitaxial films and ultra-thin films with thicknesses below a few 10 nm [2], [3].

The main steps of the CSD process are schematically presented in Figure 1.1. The fabrication of the films begins with the choice of suitable reagents, which are usually salts, such as carboxylates and metal-organic compounds, such as alkoxides. The reagents are mixed in a stoichiometric ratio corresponding to the composition of the film, and in some cases refluxing and distillation are used. In the next step the coating solution is deposited on a substrate. Spin coating of the solution and dip coating of the substrate in a solution bath are by far the most often used deposition techniques. The as-deposited "gel" film is then heated to intermediate temperatures (200–400 °C) in order to remove the volatile solvents and by-products and to thermally decompose the functional groups, which are bonded to the metal-oxygen network. The as-obtained amorphous oxide thin film is then further heated to achieve crystallization at temperatures between 600 and 1000 °C, either in a conventional furnace or in a rapid thermal annealing furnace. The deposition and heating steps can be repeated in order to prepare thicker films and temperatures higher than the crystallization temperature can be used in order to increase the grain size and the density of the films. On the other hand, the films with dense microstructures can also be obtained by repeating the drying, pyrolysis and crystallization steps for each individual deposit of the coating solution, as will be discussed in later sections [2]–[6].

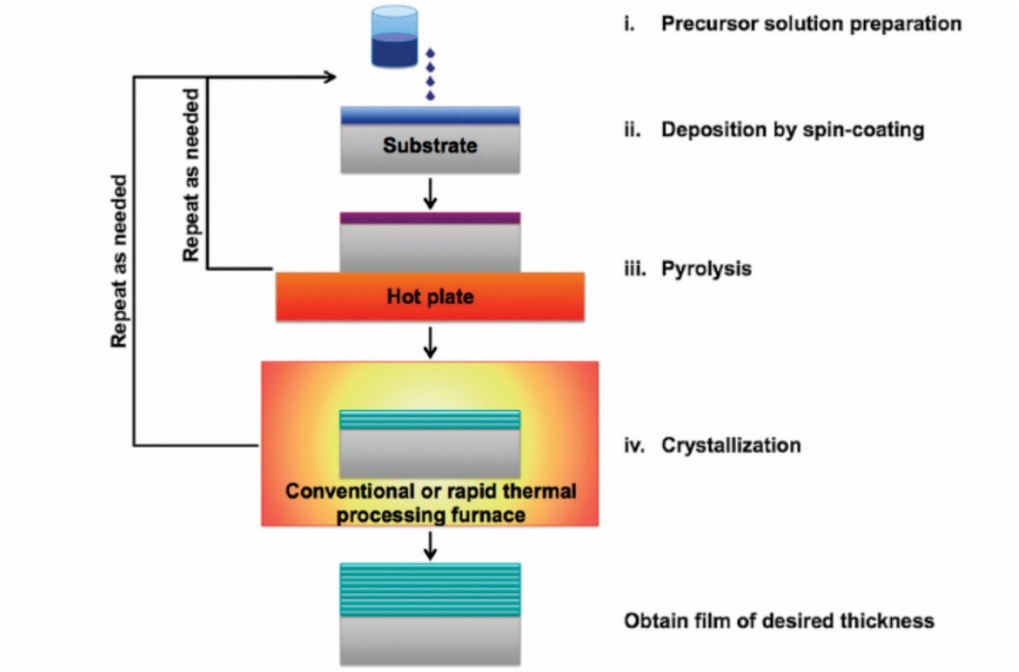


Figure 1.1: Schematic presentation of the steps of the Chemical Solution Deposition process [7].

In order to prepare high-quality thin films using the CSD method:

- the solution should be stable over a long period of time,
- the decomposition of the precursors during heat treatment should proceed without the formation of undesired residues,
- there should be no phase separation of the precursors on the macroscopic and microscopic levels,
- the coating solution should have suitable rheological properties for a selected deposition technique,
- the coating solution should wet the substrate sufficiently,
- there should be minimal degradation of the substrate during processing,
- the formation of cracks or any non-uniformities should be avoided [2]–[6].

The most frequently used CSD processes for the fabrication of functional oxide thin films are divided into three groups: classical sol-gel, metal-organic decomposition and hybrid or chelating processes [3], [6].

1.1.1 Hybrid process

In the hybrid CSD process the coating solution for different perovskites, such as alkaline-earth titanates, is synthesized from metal carboxylates and metal alkoxides. Short-chain carboxylate precursors such as acetates or propionates dissolved in an excess of carboxylic acid are normally used as reagents for the A-site ions in the perovskite lattice while a metal alkoxide is used as the reagent for the B-site ions [2]–[5].

Metal alkoxides are compounds with organic ligands attached to the metal or metalloid atom. Their general chemical formula is $M(OR)_x$, where M is a metal with the valance x and R is an organic group (often a simple alkyl, substituted alkyl or alkenyl group). The transition-metal alkoxides are very reactive and therefore require a dry atmosphere for manipulation and storing. They are often used as precursors for the synthesis of the coating solutions due to their high purity and good solubility in organic solvents. They readily

react with water via a hydrolysis reaction, where a hydroxyl ion becomes attached to the metal ion. The following reactions are shown for one alkoxide group only:

$$-M-OR+HOH \rightarrow -M-OH+R-OH \tag{1.1}$$

Depending on the amount of water the reaction may proceed to completion when all the OR groups are replaced by the OH groups, or it proceeds only partially. Two partially hydrolyzed molecules react during the condensation reaction with the elimination of water:

$$-M-OH+HO-M- \rightarrow -M-O-M-+HOH \tag{1.2}$$

and the partially hydrolyzed and the non-hydrolyzed molecules react through the elimination of alcohol:

$$-M-OH+RO-M- \rightarrow -M-O-M-+R-OH \tag{1.3}$$

The reactions of hydrolysis and condensation are the key reactions of the sol-gel process, where the metal-oxygen-metal bonds are formed, resulting in short-chain polymeric species, which are still soluble in the solvent of the precursor solution.

The alcohols are the most often used solvents, particularly their ether alcohol and polyol derivatives. The alcohols also act as reagents in the alcoholysis reaction (alcohol exchange), which results in a reduced hydrolysis sensitivity of the starting alkoxide reagents:

$$-M-OR+\ R'-OH\ \rightarrow M-OR'+R-OH \tag{1.4}$$

where OR is a reactive alkoxy group and OR' is another, less reactive, alkoxy group such as 2-methoxyethoxy [3], [5]–[8].

Metal carboxylates with the general formula $M(OOCR)_x$ are derivatives of carboxylic acids. The length and chemical nature (single or double bonds, linear or branched shape) of the organic groups determine the polarity and the decomposition behavior of the acid and the corresponding carboxylate. The main reason for the popularity of the metal carboxylates is that they are usually commercially available, cheap and that their parent carboxylic acids can be used as solvents, which are usually less toxic than other organic solvents such as 2-methoxyethanol $CH_3OCH_2CH_2OH$, which is frequently used [3]–[6], [9], [10].

In the hybrid or "chelate" processes the compounds such as acetic acid, acetylacetone or amino compounds are often used because they react readily with alkoxides, resulting in the formation of species that are less sensitive to hydrolysis. The main disadvantage of the hybrid processes is the complexity of the different reactions (hydrolysis, condensation, alcoholysis) that occur during the synthesis of the coating solution, which results in a limited ability to control the precursor structure [3]–[6], [9], [10].

1.1.2 Deposition, drying, pyrolysis

Spin coating is a commonly used technique for the deposition of functional-oxide-based thin films. The coating solution is deposited onto a substrate, which is placed on a spinner and held by vacuum. The coated substrate is then rapidly rotated at a few thousand rotations per minute. The spinning of the film is then held for a set period of time in order to obtain a very thin and uniform layer of the coating material on the substrate. The thickness of a single deposited layer is usually from 50 nm to 100 nm, depending on the molarity and viscosity of the coating solution, the wetting of the substrate and the rate of spinning [2], [3], [11].

Immediately after the deposition the film consists of an inorganic network with bound organic groups with the solvent entrapped within the pores. Prior to the crystallization the organic groups as well as the solvent should be removed, which occurs by heating the film in one or more steps, firstly at temperatures between 100 and 200 °C and later at higher temperatures. The process of the removing the organic species in air or oxygen is called pyrolysis. It includes different chemical reactions, such as the decomposition of the reagents, where the M-O-C and M-O-H bonds are broken, resulting in the formation of the M-O-M network. During these processes an extensive volume shrinkage of the film occurs. The latter is the most extensive at room temperature during deposition and during pyrolysis, when the film can shrink in the thickness direction by 50–70 % [2], [3], [12].

1.1.3 Crystallization and evolution of microstructure

Typically, the film is amorphous after pyrolysis and upon further heating at higher temperatures it transforms to a crystalline phase. The theoretical description of the crystallization in glass is used to describe the nucleation and growth in solution-derived thin films [2]–[4], [6].

The nucleation of a new phase requires the creation of the interface between the amorphous matrix and the nucleus, and this represents a large energy barrier. Since the free energy of the amorphous phase is greater than the free energy of the crystalline phase at a given temperature, there is a strong tendency to decrease the free-energy by crystallization. The driving force for crystallization is therefore the free energy difference per unit volume associated with the amorphous-to-crystalline phase transformation, ΔG_v. It is temperature dependent and decreases at higher temperatures. In the case of homogeneous nucleation, spherical nuclei are formed within the bulk of the amorphous phase, while in the case of the heterogeneous nucleation, cap-shaped nuclei are formed at the interface between the two phases: between the substrate and the film or the film and the vapor phase. A schematic presentation of both nucleation mechanisms is shown in Figure 1.2 [2]–[4], [6].

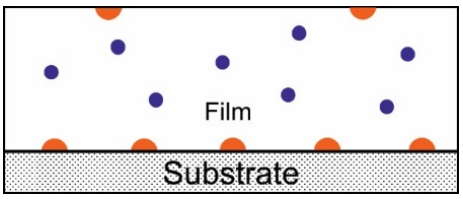


Figure 1.2: In the case of heterogeneous nucleation the nuclei (orange) grow from the substrate/film or film/atmosphere interfaces, while in the case of homogeneous nucleation the nuclei form randomly in the amorphous matrix of the film (blue).

The overall excess free-energy change ΔG, associated with the formation of the spherical nuclei with the radius r in the amorphous matrix, is equal to the sum of the volume excess free energy, ΔG_V, and surface excess free energy, ΔG_S:

$$\Delta G = \Delta G_V + \Delta G_S = -\frac{4}{3}\pi r^3 \Delta G_v + 4\pi r^2 \gamma \tag{1.5}$$

where γ is the surface energy per unit area associated with the formation of the nucleus. The overall excess free energy change of the nucleation ΔG passes through a maximum (ΔG^*) at the critical radius of the nucleus, r^* (see the blue curve in Figure 1.3). Below r^* the newly formed nuclei are not stable, while for $r > r^*$, the nuclei are stable and continue

to grow. The critical energy barrier (ΔG^*_{homo}) that the system must overcome to form stable nuclei via homogeneous nucleation is therefore given by:

$$\Delta G^*_{homo} = \frac{16\pi\gamma^3}{3(\Delta G_v)^2} \tag{1.6}$$

According to Eq. (1.6) the driving force for crystallization and the surface energy are the key thermodynamic variables associated with the crystallization. If the surface energy is increased, the energy barrier for homogeneous nucleation also increases. But if the driving force for the nucleation is increased, the energy barrier decreases and homogenous nucleation is favored.

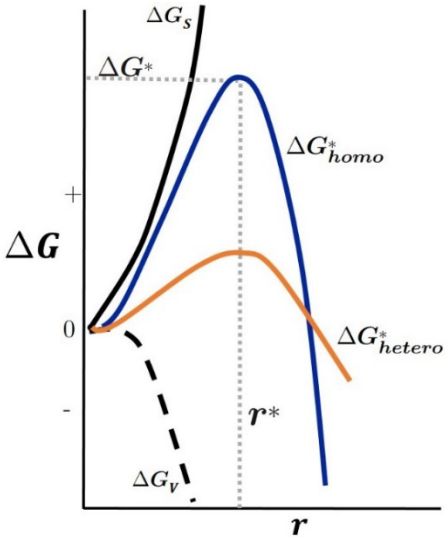


Figure 1.3: Free-energy diagram for homogeneous (blue line) and heterogeneous nucleation (orange line) explaining the existence of a critical nucleus size [12].

In the case of heterogeneous nucleation the expression for ΔG^*_{homo} (Eq. (1.6)) is multiplied by the contact-angle term $f(\Theta)$, which depends on the surface energies of the growing new phase, the solid surface (most often the substrate) and the amorphous phase:

$$\Delta G^*_{hetero} = \Delta G^*_{homo} f(\Theta) \tag{1.7}$$

$$f(\Theta) = \frac{2 - 3cos\Theta + cos^3\Theta}{4} \tag{1.8}$$

The angle Θ is the contact angle between the nucleus and the solid surface, and corresponds to the wetting angle in liquid-solid systems. When the angle Θ is 180 °, the function $f(\Theta)$ is 1 and Eq.(1.7) becomes $\Delta G^*_{hetero} = \Delta G^*_{homo}$ and the energy barriers for both heterogeneous and homogeneous nucleation are the same. But when the contact angle Θ is between 0 ° and 180 °, the function $f(\Theta)$ is less than 1 and heterogeneous nucleation is energetically more favorable than homogeneous nucleation (see Figure 1.3). The behavior of a newly created nucleus, regardless of the nucleation mechanism, depends on its size; it can either grow or re-dissolve, but the process that it undergoes should decrease its total free energy [2]–[4], [6], [13].

When stable nuclei are formed either by homogeneous or heterogeneous nucleation they tend to grow until they impinge on each other and the boundaries between them form. The

driving force for the formation of a boundary between two crystals or grains in a contact is the decrease of the energy. Namely, the newly formed interface, or the grain boundary, has a lower energy than the energies of the free surfaces of the two crystals [14]–[16].

The competition between both nucleation mechanisms influences the initially formed microstructure of the film. Predominantly homogeneous nucleation leads to a granular microstructure consisting of equiaxed grains within the bulk of the film, while heterogeneous nucleation leads to the columnar microstructure, where one grain extends through the whole film thickness, as schematically presented in Figure 1.4. Studies of barium titanate $BaTiO_3$ and lead zirconate titanate $Pb(Zr,Ti)O_3$ thin films have revealed that different microstructures of both systems form as a consequence of different nucleation mechanisms [3]. Figure 1.4 a) shows a granular microstructure of a $BaTiO_3$ thin film prepared on a platinized silicon substrate, which formed via prevailing homogeneous nucleation [17]. A columnar microstructure of a $Pb(Zr_{0.3}Ti_{0.7})O_3$ thin film prepared on a platinized silicon substrate, which developed as a consequence of prevailing heterogeneous nucleation, is presented in Figure 1.4 b) [18].

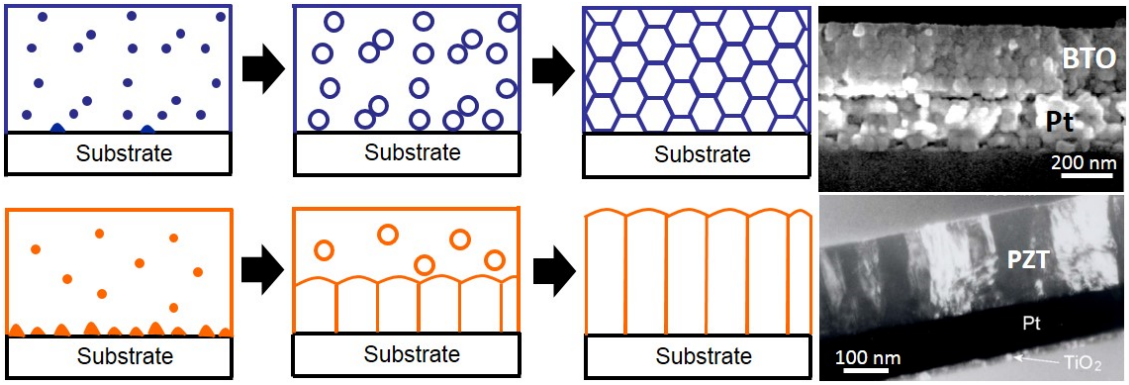


Figure 1.4: Schematic presentation of prevailing a) homogeneous and b) heterogeneous nucleation and the resulting cross-sectional microstructures. The SEM micrograph of the $BaTiO_3$ (BTO) thin film prepared on a platinized silicon substrate [17] is added as an example of a film with a granular microstructure, while the TEM micrograph of the microstructure of the $Pb(Zr_{0.3}Ti_{0.7})O_3$ (PZT) thin film [18] represents an example of a film with a columnar microstructure.

1.1.4 Grain growth in thin films

Grain growth is a process that occurs through the motion of grain boundaries, resulting in the shrinkage and elimination of smaller grains and in the increase in the average grain size. Grain growth is driven by the reduction of the total grain-boundary area and in the corresponding reduction of the total grain-boundary energy. On the microscopic scale this is accomplished when an individual grain boundary moves toward its center of curvature by the movement of atoms across the grain boundary. The grains with six sides in plane-view are in thermodynamic equilibrium, while the grains with less than six sides will shrink and the grains with seven or more sides will continue to grow [16]. The rate of normal grain growth therefore depends on the grain-boundary mobility, energy and curvature. The result of normal grain growth in thin films is an increasing grain size with time and the time-invariant shape of the grain size distribution, as shown in Figure 1.5 [14], [15].

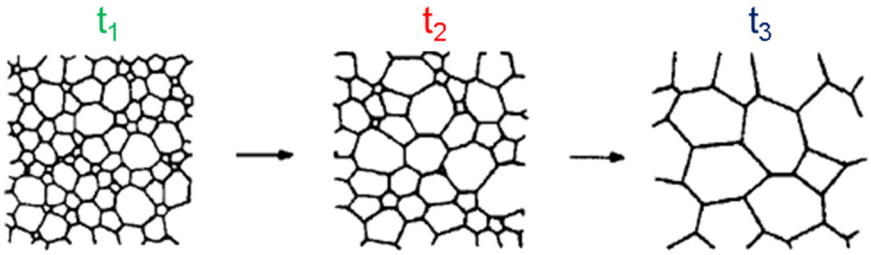


Figure 1.5: Increasing average grain size with time t during the normal grain growth process [19].

The total energy of the grains is associated with the energies of the free surface, the interface and the grain boundaries, as well as with the stresses that arise in the film. The balance between the surface energy of the neighboring grains and the energy of the grain boundaries leads to the formation of grooves where the boundaries intersect the surface of the film. As the grain growth proceeds, the grooves eventually form and suppress or stop further grain-boundary motion, resulting in stagnation of the grain growth [20]–[24]. The phenomenon is also referred to as the specimen-thickness effect [20].

Palmer et al. [21] prepared germanium thin films that consisted of grains smaller than the thickness of the films. As they annealed the films at 900 °C for 5 min the normal grain growth resulted in the evolution of columnar grains. The grain growth slowed down and stopped once a columnar microstructure developed, even when the films were annealed at higher temperatures. The lateral grain sizes were approximately 2.5 times the film thickness. This observation agrees well with the results of the simulation of the grain growth stagnation in thin films, where the estimated ratio of the grain size to film thickness is equal to 2.9 [24]. Stech et al. [22] prepared 65-nm- and 140-nm-thick TiO_2 films and annealed them at temperatures between 700 °C and 900 °C. The grain size of both films increased with increasing temperature, until it reached the film thickness after annealing at 900 °C (see Figure 1.6). By comparing the microstructure of the film with the bulk sample, they observed that the grain growth in the films stopped when the grain size was similar to the film thickness, while in the bulk sample the grain size increased up to 6 times.

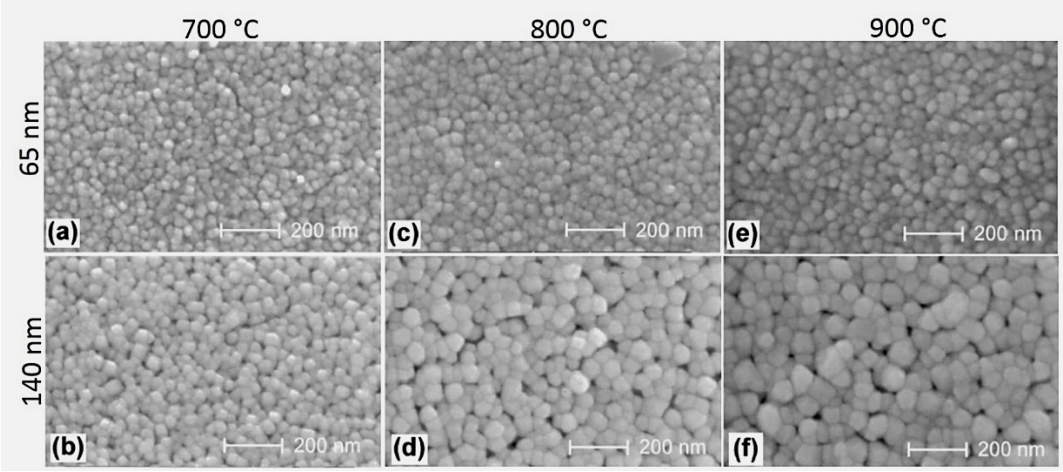


Figure 1.6: SEM micrographs of TiO_2 thin films with thicknesses of 65 nm and 140 nm annealed at a), b) 700 °C, c), d) 800 °C and e), f) 900 °C [22].

Rost et al. [23] investigated the evolution of the grain shape and size during the growth of polycrystalline Au thin films. The 30-nm-thick films were deposited on atomically flat quartz substrates, transferred to the variable-temperature scanning tunneling microscope (STM) and heated from 293 K to 748 K. The films were directly observed with the STM and the change in the root-mean-squared roughness (RMS) of the surface was investigated and connected to the motion of the grain boundaries, the increase of the grain size and the formation of the grooves. The non-monotonic dependence of the RMS on the average grain size is presented in Figure 1.7 a). Firstly, the RMS value dropped, then it remained constant and with a further increase of the grain size it increased again. Typical STM height lines at different stages of the deposition are presented in Figure 1.7 b), where each dome-shaped top corresponds to an individual grain and the vertical lines denote the boundaries between the grains. The as-deposited films with approximately 50-nm-large grains have rough surfaces due to the grain orientations that have a high grain-boundary energy. As the film was annealed at 648 K, the drop of the RMS was explained by the reorientation of the grain boundaries into energetically more favorable orientations, resulting in an increase of the grain size from 50 nm to approximately 100 nm. With a further increase of the temperature to 748 K the grain size increased to approximately 300 nm, resulting in an increase of the RMS value.

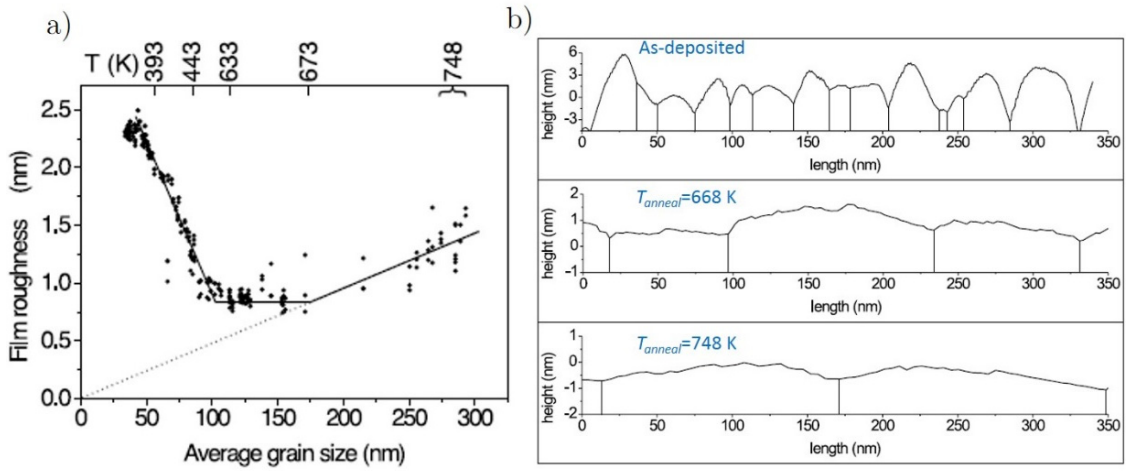


Figure 1.7: a) Film roughness of the Au surface plotted as a function of the grain size of the film and annealing temperature. b) STM height lines of the Au film immediately after deposition, after annealing at 668 K and at 748 K.

The temperature dependence of the nucleation and grain growth rate needs to be considered [25]. When the annealing temperature is low, the nucleation rate is high, resulting in the formation of many nuclei that grow until they impinge on each other. The microstructure of the films thus consists of many small grains, as shown in the case of the granular microstructure in Figure 1.8 a). On the other hand, at high annealing temperatures, fewer nuclei are formed, which grow with higher rates, resulting in a coarse microstructure, as schematically presented in Figure 1.8 b).

In addition to the normal grain growth a small fraction of grains may continue to grow, while the majority of the grains grow at a much lower rate or do not grow at all. Such growth is called abnormal grain growth and results in a bimodal grain size distribution [14]–[16], [20].

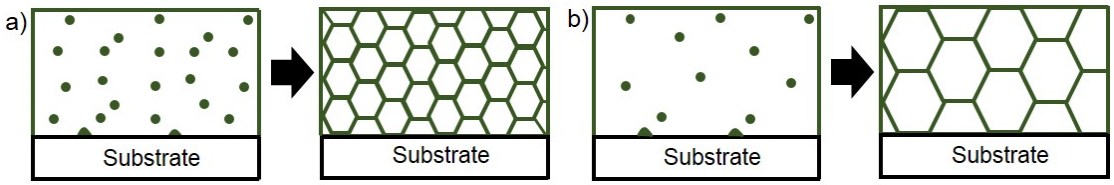


Figure 1.8: a) Evolution of the fine granular microstructure of the films when the nucleation rate is high and the growth rate is low. b) Evolution of the coarse granular microstructure that forms when the nucleation rate is low but the growth rate is high.

1.1.5 Structural zone model for solution-derived thin films

The model to predict the microstructure of the films prepared by physical vapor deposition (PVD) methods was proposed in the early 80s [26], [27]. The films of different metals were prepared on metal or glass substrates by magnetron sputtering. According to the temperature of the substrate and the inert-gas pressure the microstructures of the films were divided into different zones (see Figure 1.9):

- At low temperatures T/T_M<0.2 (T_M - melting temperature) within the *Zone 1* there is no bulk diffusion and only limited surface diffusion. The grains are fibrous and tapered, defined by open boundaries and with the size and orientation determined by the initial random nucleation.
- At intermediate temperatures (0.2<T/T_M<0.3) within the transition *Zone T* the surface diffusion becomes substantial and the voids between the fibrous grains begin to fill, resulting in a dense microstructure. With increasing temperature the width and height of the grains increase.
- At higher temperatures (0.3<T/T_M<0.5) within *Zone 2* the surface diffusion of the atoms increases and the grain boundaries start to migrate, and so recrystallization is possible. The grains are columnar, separated by distinct boundaries and have highly faceted surfaces.
- The columnar microstructure also predominantly persists within *Zone 3* at temperatures T/T_M>0.5, where bulk diffusion dominates. Recrystallization resulting in equiaxed grains is also possible.

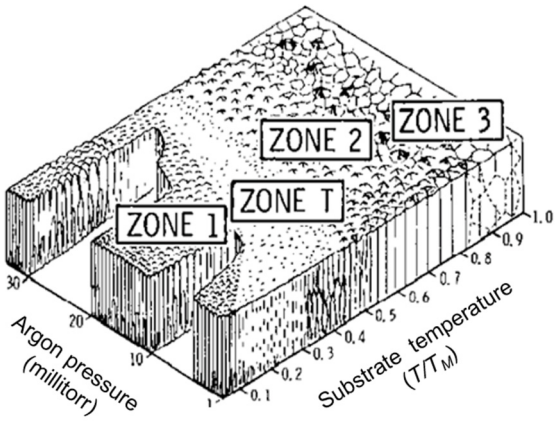


Figure 1.9: Structural zone model for the films prepared by physical deposition proposed by Thornton [26]. T_M – melting temperature.

In 2004 Schuler et al. [28], [29] proposed a model for solution-derived metal-oxide thin films analogous to the one proposed by Thornton for the PVD films (Figure 1.9). The authors investigated the microstructural features of the films as a function of the annealing temperature, intrinsic crystallite size (ICS) and single layer thickness (SLT). Note that the intrinsic crystallite size corresponds to the average grain size of an individual film. Based on the studies of various undoped and doped SnO_2, In_2O_3, ZnO and TiO_2 thin films an empirical ratio between the intrinsic crystallite size and the single layer thickness (ICS/SLT) was introduced. The microstructures of the corresponding films were divided into three zones similar to the structural zone model for the PVD films. The studied films consisted of one or more deposited layers and the thickness of an individual deposited layer was larger than the crystallite size. The thickness of a single deposited layer in the range of the crystallite size or even less was obtained by decreasing the molarity of the solution, by introducing the annealing of each individual deposit (multi-step heating) or by increasing the withdrawal speed in the case of dip-coated films.

The microstructures of the films were divided into three groups depending on the ICS/SLT ratio as a function of the ratio of the annealing temperature and melting temperature:

- For ICS/SLT<0.42, where an individual layer consists of grains significantly smaller than the layer thickness, the corresponding microstructure is *granular* as a result of predominant homogeneous nucleation.
- In the case of a film consisting of a few layers and with the grain size roughly equal to the thickness of an individual deposit, a so-called *layered* microstructure is identified (0.42<ICS/SLT<1). This structure can be explained by the stacking of single layers where both heterogeneous and homogeneous nucleation occur.
- When the film consists of very thin deposited layers, i.e., for ICS<SLT, a *columnar* microstructure developed. A low thickness for an individual layer increases the probability of heterogeneous nucleation on the underlying crystalline material due to the increased surface-to-volume ratio (ICS/SLT>1).

The proposed model with the TEM micrographs as examples of the corresponding types of microstructures for selected solution-derived films is presented in Figure 1.10. [28].

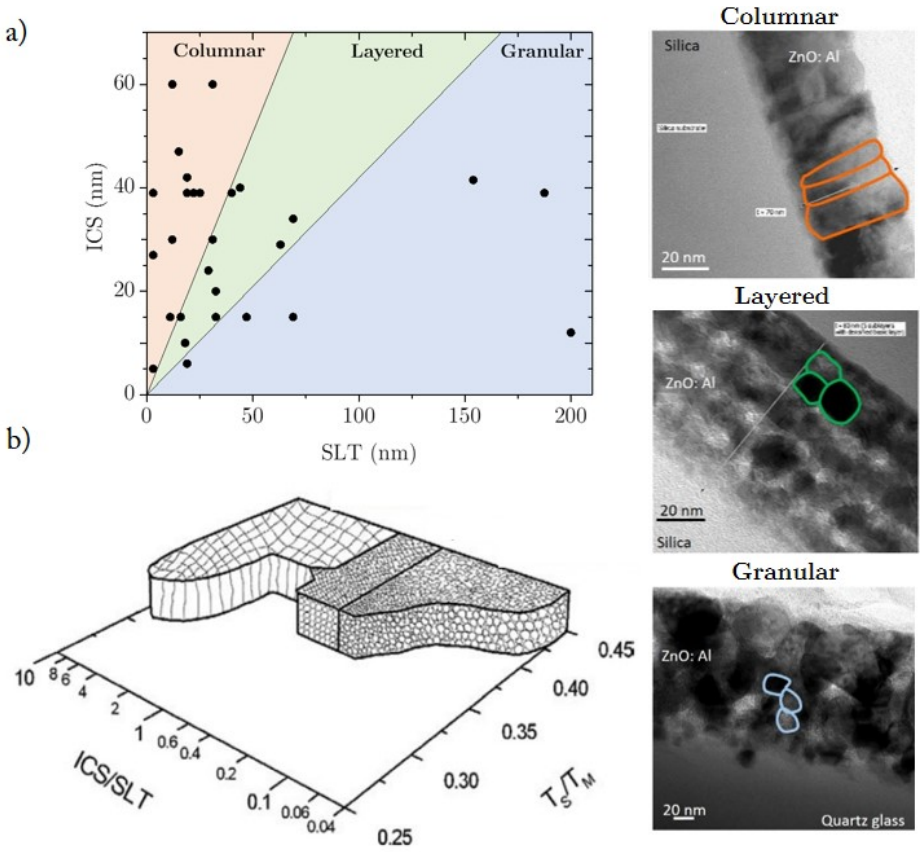


Figure 1.10: a) ICS plotted as a function of SLT after the model proposed by Schuler et al. [28]. b) 3D graph, where ICS/SLT is plotted as a function of temperature (T_S/T_M). TEM cross-section micrographs of different types of microstructures for Al-doped ZnO thin films prepared by dip-coating are added. The granular microstructure was obtained when the 0.47-M solution was deposited by dip-coating with a withdrawal speed of 5 mm/s and annealed at 600 °C. The layered microstructure resulted from five deposits of 0.2-M solution with a withdrawal speed 1 mm/s. The columnar microstructure was obtained from 20 deposits of 0.05-M solution with a withdrawal speed of 1 mm/s, and when the films were annealed at 450 °C. In the case of the layered and columnar microstructures the films were annealed after each individual deposit. ICS – intrinsic crystallite size, SLT – single layer thickness, T_S – sintering temperature, T_M – melting temperature. *After* [28].

1.2 Barium Strontium Titanate

1.2.1 $Ba_xSr_{1-x}TiO_3$ solid solution

Barium strontium titanate $Ba_xSr_{1-x}TiO_3$, x=0-1 (BST) is a solid solution of barium titanate $BaTiO_3$ and strontium titanate $SrTiO_3$. The melting point of the BST solid solution varies between 1618 °C for $BaTiO_3$ and 2080 °C for $SrTiO_3$ [30].

$BaTiO_3$ is a prototype ferroelectric with a perovskite unit cell. Above the phase-transition temperature T_C ($T > \sim$130 °C) the unit cell of $BaTiO_3$ is cubic (see Figure 1.11). The phase above the T_C is referred to as the paraelectric phase, where the polarization dependence on the applied electric field is a nonlinear function, but without a hysteresis loop as shown in Figure 1.11 [31], [32].

Below the phase-transition temperature or the Curie point T_C (0 °C<T<130 °C) the unit cell of $BaTiO_3$ is tetragonal with the polar axis in the direction of the tetragonal deformation (Figure 1.11) [33]. The polarization–electric-field dependence for the material in the ferroelectric phase is nonlinear and described by the hysteresis loop (see Figure 1.11). At a low electric field the polarization linearly increases due to the orientation of the domains, i.e., the regions of the crystal with uniformly oriented spontaneous polarization, in the direction of the applied field. When the field is high enough the domains with the directions of polarization, which are less easy to reorient, will start to switch in the direction of the field until saturation occurs. When the field starts to decrease, some domains will back-switch and at zero field the polarization is non-zero (remanent polarization P_r). A further decrease of the electric field in the negative direction will cause a new alignment of the domains and saturation in the direction of the applied electric field. The field necessary to bring the polarization back to zero is called the coercive field, E_c. The ferroelectric phase in the case of the tetragonal unit cell therefore possesses two equilibrium orientations of the spontaneous polarization, which can be switched by an external electric field [32].

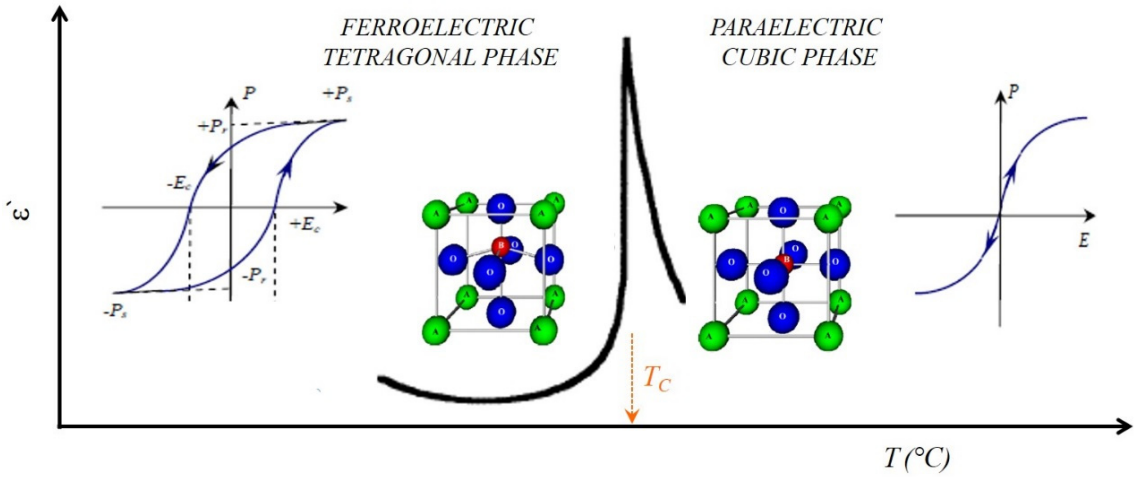


Figure 1.11: Schematic presentation of the changes in a perovskite material which transforms from a paraelectric cubic into the ferroelectric tetragonal phase at the phase-transition temperature T_C. P – polarization, $\pm P_s$ – spontaneous polarization, $\pm P_r$ – remanent polarization, E – electric field, E_c – coercive field. *After* [31], [32].

$SrTiO_3$ has a cubic perovskite unit cell. It is an incipient ferroelectric, meaning that it is in paraelectric phase at all temperatures. Note that some incipient ferroelectrics in the form of thin films may show a peak in the dielectric constant, which was explained as a consequence of the stresses in the films [34], [35].

The crystal structure of the BST solid solution at room temperature is tetragonal for Ba-rich compositions and transforms to cubic as the Sr content increases at $x \geq 0.30$ [36]. The Curie point of the BST solid solution decreases from ~130 °C for the case of pure $BaTiO_3$ down to the virtual Curie point of $SrTiO_3$ at -273 °C for ≈3.7 °C per mole % as shown in Figure 1.12 [33]. The dependence of dielectric properties on the composition of the BST solid solution allows tailoring of the Curie point and consequently its dielectric properties [37].

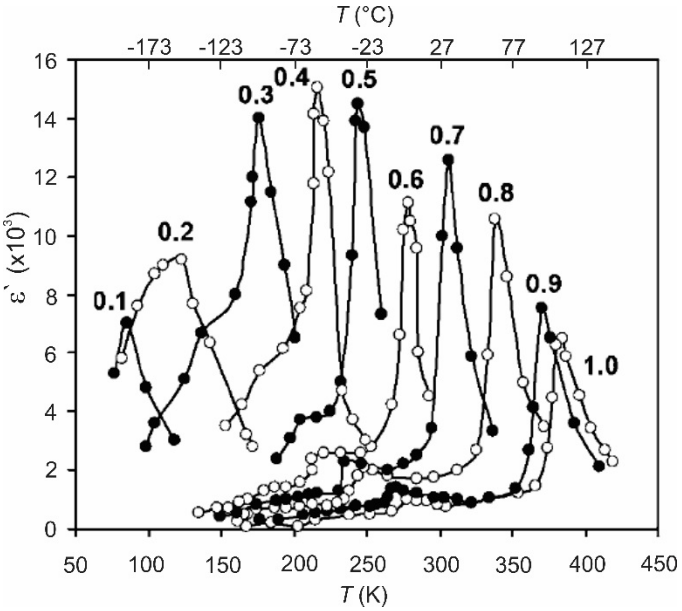


Figure 1.12: Temperature dependence of the dielectric constant of $Ba_xSr_{1-x}TiO_3$ ceramics with different Ba concentration x [38].

The non-linear dependence of the permittivity on the applied electric field bias (see Figure 1.13) is described by the tunability n defined as the ratio of the dielectric permittivity of a material at zero electric field to its permittivity at some non-zero electric field [38]:

$$n = \frac{\varepsilon(0)}{\varepsilon(E)} \tag{1.9}$$

The tunability is often also expressed as the relative tunability:

$$n_r = \frac{\varepsilon(0) - \varepsilon(E)}{\varepsilon(0)} = 1 - \frac{1}{n} \tag{1.10}$$

Both ferroelectric and paraelectric phases may be used in tunable microwave devices provided that they have low losses and a reasonable tunability ($n \geq 2$) [38].

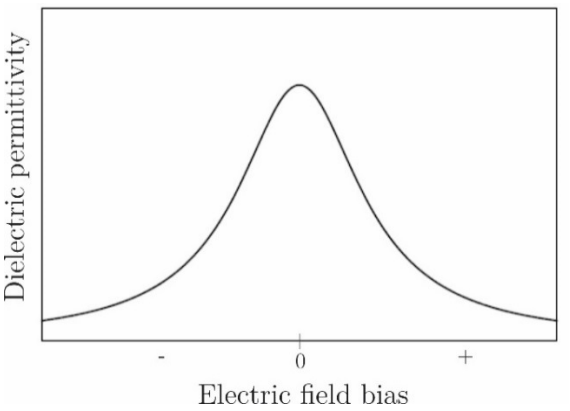


Figure 1.13: Permittivity dependence versus applied electric field for the paraelectric phase [39].

1.2.2 Thin films

BST thin films of various compositions were prepared by different deposition methods such as magnetron sputtering [40]–[44], metal-organic chemical vapor deposition (MOCVD) [45], pulsed-laser deposition (PLD) [46]–[48] and CSD [17], [49]–[57]. Selected reports on CSD-derived BST thin films with the details of the preparation procedures are collected in Table 1.1.

In the case of solution-derived BST thin films the hybrid process is well established. First, the A-site precursor solution is prepared by dissolving barium and/or strontium carboxylates, mostly acetates or propionates in their parent carboxylic acid. The B-site precursor solution is prepared by weighing the titanium alkoxide, usually titanium n-butoxide in a flask and dissolving with 2-methoxyethanol. The alkoxide is usually stabilized by chelating with two moles of acetylacetone per one mole of alkoxide. The precursor solutions are mixed together at room temperature and the final concentration of the solution is adjusted with the solvent [10], [17], [58].

The most widely used technique to deposit BST thin films is spin coating. The films are usually spin-coated at 2000–5000 rpm for 30 s to 60 s and dried and/or pyrolyzed at temperatures between 200 °C and 400 °C for 2 min to 20 min. The deposition-drying/pyrolysis steps are usually repeated for each deposit followed by the annealing of the film (two-step annealing process). It was shown by Hoffmann et al. [50] that repeating the annealing of each individual, thin enough deposit (multi-step annealing process) leads to dense BST films with a columnar microstructure and with enhanced dielectric properties, as will be discussed later in the text [50].

Table 1.1: Overview of the literature reports on CSD of (Ba,Sr)TiO_3 thin films. The selected films were prepared by spin-coating. (C_M – molar concentration of the coating solution, T_P – pyrolysis temperature, T_{anneal} – annealing temperature, two-step – drying and/or pyrolysis for each deposited layer followed by annealing, multi-step – drying and/or pyrolysis and annealing of each individual deposited layer separately, *NA* – not available, MBE – Molecular Beam Epitaxy, 2-EOE– 2-ethoxyethanol).

Material	*Substrate*	*Precursors*	*Solvents*	C_M	*Heat treatment*	T_P *[°C/min]*	T_{anneal} *[°C/min]*	*Ref.*
$BaTiO_3$	$Pt/TiO_2/SiO_2/Si$	Ba-Ti methoxypropoxide	Butanol	0.25	Multi-step	350/5	700/30	[51]
	MBE $BaTiO_3/Si$	Ba-Ti methoxypropoxide	Methoxypropanol	0.25	Two-step	350/5	700/330	[49]
	(100)Si	Ba-Ti methoxypropoxide	Methoxypropanol	0.25	Two-step	350/5	750/60	[49]
	$Pt/ZrO_2/SiO_2/Si$	Ba-propionate, Ti-tetra-n-butoxide	Propionic acid, butanol	0.1	Multi-step	/	750/*NA*	[50]
				0.3	Two-step	400-500/*NA*	750/*NA*	[50]
	$Pt/TiO_2/SiO_2/Si$	Ba acetate, Ti butoxide	Acetic acid, methanol	0.3	Multi-step	300/5	750/*NA*	[17]
	$(100)LaAlO_3$	Ba acetate, Ti butoxide	Acetic acid, methanol	0.3	Multi-step	300/5	750/*NA*	[17]
	$Pt/TiO_2/SiO_2/Si$	Ba acetate, Ti butoxide	Acetic acid, methanol	0.05-0.10	Multi-step	300/5	750/*NA*	[17]
$SrTiO_3$	$Pt/ZrO_2/SiO_2/Si$	Sr-propionate, Ti-n-butoxide	Propionic acid, butanol	0.1	Multi-step	/	750/*NA*	[50]
$Ba_{0.7}Sr_{0.3}TiO_3$	Pt/(100)MgO	Ba, Sr acetates, Ti-isopropoxide	Acetic acid, 2-EOE	0.3	Multi-step	350/3	650/20	[55]
							750/20	
							800/20	
	$Pt/BaTiO_3/(100)Si$	Ba, Sr acetates, Ti-isopropoxide	Acetic acid, 2-EOE	0.3	Multi-step	350/3	650/20	[55]
							750/20	
							800/20	
	Pt100/(100)MgO	Ba, Sr acetates, Ti-isopropoxide	Acetic acid, 2-EOE	0.3	Multi-step	350/3	650/20	[55]
							750 /20	
							800/20	

1.2.2.1 Crystallization and evolution of microstructure

Hasenkox et al. [58] studied the influence of the length of the carboxylate chain of alkaline-earth carboxylates on the crystallization temperature, microstructure and dielectric properties of $BaTiO_3$, $Ba_{0.7}Sr_{0.3}TiO_3$ (BST 70/30) and $SrTiO_3$ films. The films were prepared by hybrid process from Ba- and Sr-carboxylates and a Ti-alkoxide precursor, which was either stabilized or not by 2,4-pentandione. They found that long-chain Ba-carboxylates, such as 2-ethylhexanoate, decompose at temperatures lower than 550 °C and transform to the pure perovskite phase at 600 °C. In the case of short-chain carboxylates, such as acetate or propionate, the decomposition temperature is approximately 600 °C and the pure perovskite phase is formed at 650 °C for propionate or 700 °C for acetate. The X-ray diffraction (XRD) analysis confirmed the presence of a barium and/or strontium titanium oxo-carbonate phase with the stoichiometry $(Ba,Sr)_2Ti_2O_5CO_3$ upon annealing of $BaTiO_3$ and $SrTiO_3$ films at 600 °C and at 550 °C for BST 70/30 films, respectively. The intermediate phase was present in the $BaTiO_3$, $Ba_{0.7}Sr_{0.3}TiO_3$ and $SrTiO_3$ thin films regardless of the titanium alkoxide precursor, see Figure 1.14. The oxo-carbonate phase was later also confirmed by other groups [49], [51], [54].

Based on the Fourier-transform infrared spectroscopy (FTIR) and XRD analysis it was proposed that amorphous films firstly crystallize into intermediate phase and secondly into the perovskite phase [58]. Since the temperature of decomposition of the thermodynamically stable intermediate phase is high (up to 650 °C) the authors assumed that the crystallization of the perovskite phase is shifted to higher temperatures. Note, however, that high crystallization temperatures (>600° C) of the perovskite phase were also observed for the case of BST films prepared from a non-carboxylate precursor solution, where the formation of an oxo-carbonate intermediate phase was avoided [59], [60].

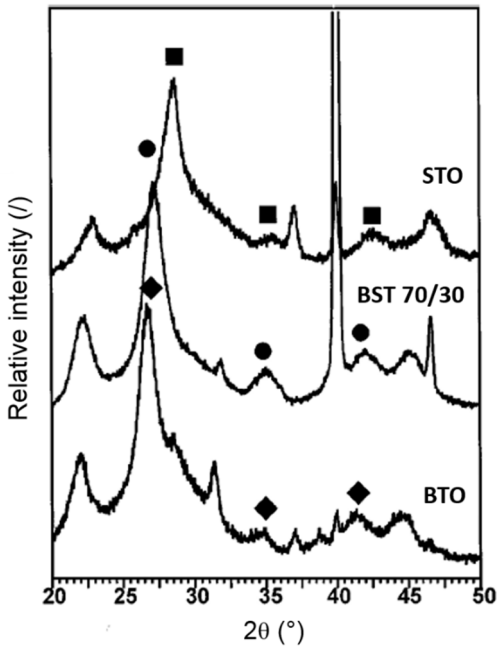


Figure 1.14: XRD spectra of $BaTiO_3$ (BTO), $Ba_{0.7}Sr_{0.3}TiO_3$ (BST 70/30) and $SrTiO_3$ (STO) thin films prepared at 600 °C for BTO and STO and at 550 °C for BST 70/30. Symbols denote the diffraction peaks that belong to the intermediate oxo-carbonate phase $(Ba,Sr)_2Ti_2O_5CO_3$ [58].

For most solution-derived BST thin films the granular microstructure is observed as presented in Figure 1.15. Schwartz et al. [17] prepared $BaTiO_3$ thin films by the hybrid CSD method on $LaAlO_3$ single-crystal substrates, which would facilitate heterogeneous nucleation due to the structure match of the pseudo-cubic perovskite lattice of the substrate and the film. Similar to the films prepared on the Pt/Si substrate, the homogeneous nucleation dominated and resulted in a granular microstructure with equiaxed grains. Even when the $BaTiO_3$ film was prepared on an underlying MBE-deposited $BaTiO_3$ thin film with excellent crystal matching, the resulting microstructure consisted again of equiaxed grains. These results show that in the case of BST thin films, a predominantly homogeneous nucleation prevails and even a structural match between the film and the substrate or the underlying MBE deposited $BaTiO_3$ layer cannot induce heterogeneous nucleation at the substrate/film and film/MBE $BaTiO_3$ layer interphases. [49].

Although a granular microstructure is characteristic for BST thin films, a columnar microstructure may be obtained through a successful manipulation of the processing conditions, as reported by Hoffmann et al. [50] and further discussed in a review paper by Schwartz et al. [3]. A few-100-nm-thick columnar films were prepared by the multi-step annealing process [50]. The deposition-annealing steps were repeated for each individual deposit. When the thickness of an individual deposit was reduced by decreasing the concentration of the coating solution to approximately 10 nm, a predominantly heterogeneous nucleation occurred at the film/substrate or film/underlying perovskite layer interfaces, leading to the evolution of columnar grains that extend through the whole film thickness. Corresponding SEM microstructures of $BaTiO_3$ and $SrTiO_3$ thin films prepared from solutions with different concentrations are presented in Figure 1.16. Columnar BST films were also prepared by other groups [55], [56], [58].

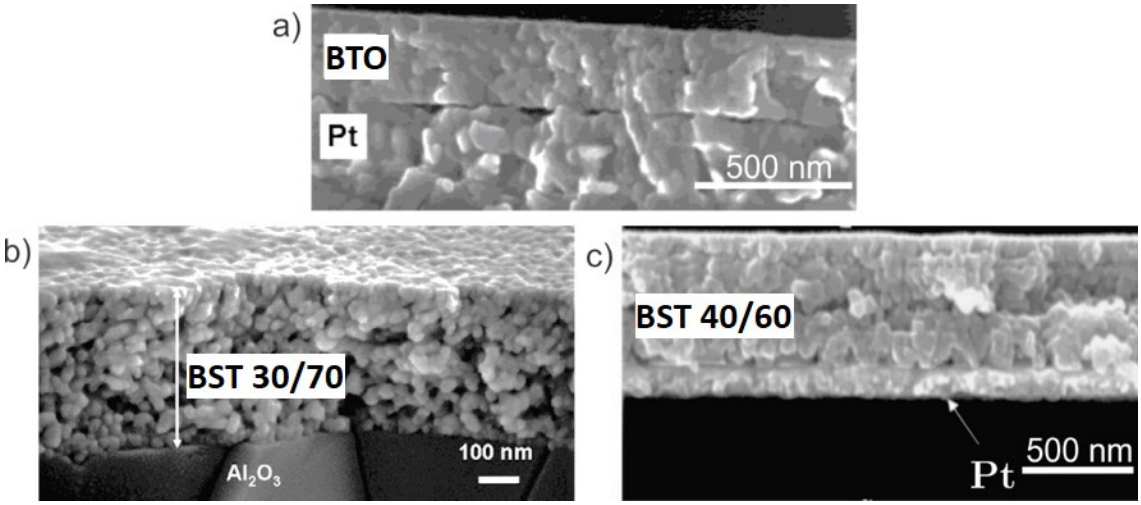


Figure 1.15: Granular microstructure of solution-derived, alkaline-earth titanate thin films. a) $BaTiO_3$ (BTO) thin film prepared at 800 °C on platinized silicon substrate [17], b) $Ba_{0.3}Sr_{0.7}TiO_3$ (BST 30/70) prepared at 700 °C on Al_2O_3 substrate [53] and $Ba_{0.4}Sr_{0.6}TiO_3$ (BST 40/60) film prepared at 800 °C on platinized silicon substrate [61].

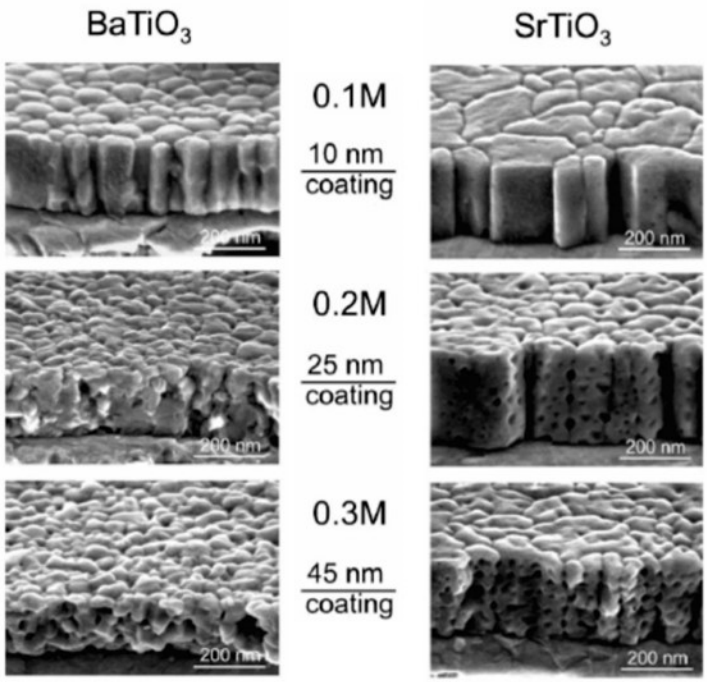


Figure 1.16: SEM cross-section and surface microstructures of the $BaTiO_3$ and $SrTiO_3$ thin films prepared from solutions with different concentrations ranging from 0.1 to 0.3 M by the multiple-step annealing process. The corresponding thicknesses of each individual layer are given in the middle column [3].

Jia et al. [62] performed a detailed TEM analysis of solution-derived $BaTiO_3$ and $SrTiO_3$ thin films with columnar microstructures, with the emphasis on the orientation relationship, the grain boundary, and lattice defects such as dislocations and twin boundaries. The coating solutions were deposited on a $Pt/ZrO_2/SiO_2/Si$ substrate by the multi-step annealing process. Each deposited layer was annealed at 750 °C for 15 min in oxygen until a thickness of about 150 nm was achieved, followed by a final annealing at 800 °C for 1h in oxygen for $BaTiO_3$ films. In the case of $SrTiO_3$ films the intermediate and the final annealing were performed at 700 °C, 30 min and 750 °C, 5h.

The TEM cross-section micrographs of columnar $SrTiO_3$ and $BaTiO_3$ thin films are shown in Figure 1.17. In the case of the 200-nm-thick $SrTiO_3$ film the thickness of an individual layer is approximately 10 nm. The grains have straight boundaries that extend through the whole film thickness with an average lateral size between 200 nm and 300 nm. On the top of the film, grooves are clearly observed. The pores are located at the grain boundaries as well as inside the grains. A detailed TEM analysis shows that the film is predominantly (111) oriented and that a cube-to-cube relationship exists between the $SrTiO_3$ grains and the Pt grains. Additionally, dislocations with lines parallel to (111) crystal planes were frequently found.

In the 150-nm-thick $BaTiO_3$ film the average lateral grain size is approximately 100 nm and the grain boundaries are less straight than in the $SrTiO_3$ film. Some smaller grains are observed near the interface with the Pt electrode. Most of the grain boundaries are free of pores and there is no amorphous or secondary phase at the interface between the film and the electrode. The perovskite phase is not preferentially oriented in contrast to the $SrTiO_3$ film. In Figure 1.17 c) a low-magnification lattice micrograph of a representative columnar grain is shown. The arrows mark individual deposits with a thickness of approximately 10 nm. Each individual deposit adopts the same orientation as the pre-existing deposit.

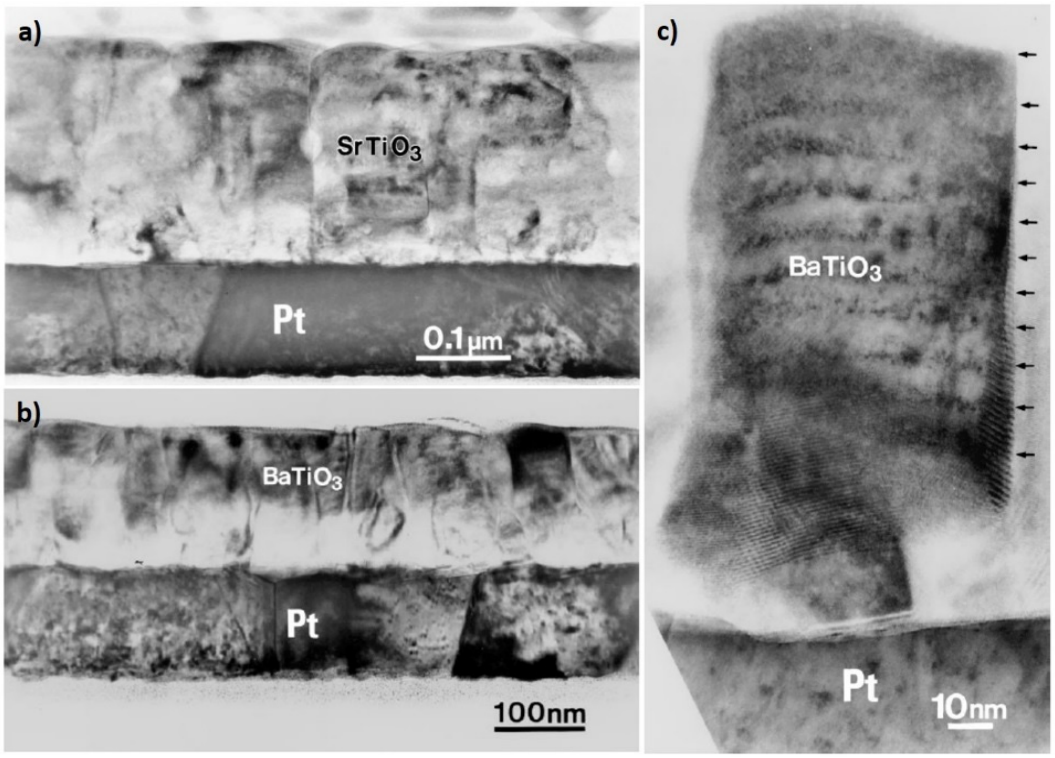


Figure 1.17: TEM cross-section micrographs of the columnar microstructure of a) $SrTiO_3$ and b) $BaTiO_3$ thin films prepared on $Pt/ZrO_2/SiO_2/Si$ substrates by the multi-step annealing process. In c) a low-magnification lattice image of a columnar grain of a $BaTiO_3$ thin film is presented [62].

Therefore, there is no disturbance of the boundaries between the individual deposits. The analysis shows that the growth mechanism that leads to such a microstructure is the layer-by-layer epitaxial growth within individual grains, which was achieved by using a diluted coating solution and a multi-step annealing process.

According to the model proposed by Schuler et al. [28] we collected the results for different solution-derived $BaTiO_3$, $SrTiO_3$ and BST thin films (see Appendix A) and plotted them in Figure 1.18. The films consisting of one or multiple deposited layers were considered, with the intrinsic crystallite size much smaller than the single layer thickness (ICS$\ll$SLT) in the case of one- or two-step annealing or with the ICS$\geq$SLT in the case of multi-step annealing.

In Figure 1.18 a) the regions corresponding to the granular and columnar microstructures are clearly observed. The layered microstructure could not be unambiguously determined from the micrographs with the exception of a few cases. We may assume that the layered microstructure thus forms only in a rather narrow ICS/SLT window.

In Figure 1.18 b) the ICS/SLT ratio is plotted versus $T_{anneal}/T_{M.}$ Three regions corresponding to different types of microstructure are distinguished. The granular microstructure develops when ICS/SLT<1, although we note that the exact boundary is presumably temperature dependent. At ICS/SLT$>$2.5 the columnar microstructure develops. The ICS/SLT range for the layered microstructure is between $\approx$1 and $\approx$2. The boundaries between each type of microstructure are slightly shifted towards higher values compared to the model by Schuler et al., see Figure 1.10.

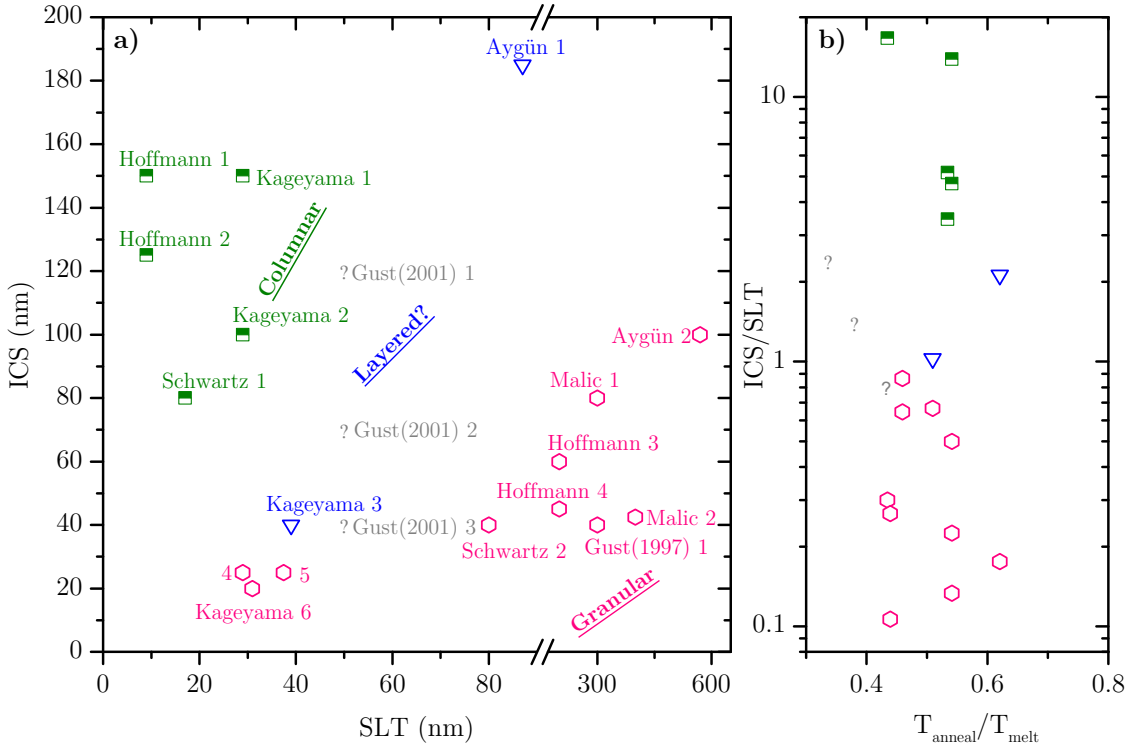


Figure 1.18: a) Intrinsic crystallite size (ICS) versus single layer thickness (SLT) and b) ICS/SLT versus T_{anneal}/T_{melt} for different $BaTiO_3$, $SrTiO_3$ and BST thin films according to the model proposed by Schuler et al. [28]. T_{anneal} – annealing temperature (K), T_M – melting temperature (K). The details of the films collected in the figure, are collected in Appendix A. Note that it is assumed that ICS is equal to the grain size.

1.2.2.2 Dielectric properties

The dielectric grain-size effect, i.e., the change of the dielectric permittivity with the grain size was studied in detail by Frey et al. [63] for $BaTiO_3$ ceramics and later on reviewed by Petzelt [64] for other materials such as $SrTiO_3$, $Pb(Zr,Ti)O_3$, $Pb(Mg_{1/3}Nb_{2/3})O_3$ and $Pb(Mg_{1/3}Nb_{2/3})O_3$-$PbTiO_3$. Frey et al. [63] prepared the $BaTiO_3$ powder with a 30-nm particle size, which was consolidated at high pressure (8 GPa) and low temperature in order to obtain ceramics with ultrafine grains. A subsequent heat treatment at higher temperatures was used to increase the grain size of the ceramics from 70 nm to 1.7 µm. The dielectric properties of the ceramics with different grain sizes were measured in the temperature range between −25 °C and 200 °C. With a decreasing grain size the broadening and the decrease of the temperature-dependent permittivity maximum and the decrease of the dielectric permittivity for the temperatures above T_C were observed (see Figure 1.19 a)).

The reduced dielectric properties were explained in terms of the brick-wall model, which was used to represent the distribution of different dielectric phases in a diphasic dielectric material. The authors suggested that $BaTiO_3$ ceramics consist of the grain interiors or isolated grains, which are separated by a continuous grain-boundary layer, as schematically shown in Figure 1.19 b). The interior of the grains undergoes a ferroelectric transition in the presence of a disordered low-permittivity grain-boundary layer. It was experimentally and theoretically shown that the grain boundary layer with a width of 8 Å and a

permittivity of 130 is already sufficient to effectively reduce the dielectric permittivity of $BaTiO_3$ ceramics with grain sizes below 2 µm. As the grain size decreases the grain-boundary area becomes significant and the influence of the low-permittivity grain boundaries becomes more pronounced, resulting in a lower permittivity of the ceramics.

The dielectric grain-size effect was also studied in ceramic thin films by different groups [40], [45], [46], [50], [65]–[67]. For example, Ihlefeld et al. [66] prepared solution-derived $BaTiO_3$ thin films on Cu foils. The films were prepared at annealing temperatures in the range from 750 °C to 900 °C. The annealing temperature was increased to promote the mass transport and consequently to increase the grain size of the films. The number of deposits was varied in order to obtain films with similar thicknesses, i.e., ~600 nm. The resulting microstructure of the films was granular in all cases. As the annealing temperature increased from 750 °C to 900 °C, the grain size increased from 80 nm to 150 nm. Simultaneously, the maximum dielectric permittivity increased from 750 to approximately 1800 in the kHz frequency range, see Figure 1.20. The dielectric permittivity of the films increased with an increasing grain size over the entire temperature range. The dependence of the permittivity on the grain size of the films was explained by the brick-wall model, as proposed for $BaTiO_3$ ceramics [63]. The influence of the grain size on the dielectric properties was also investigated in the solution-derived $Ba_{0.5}Sr_{0.5}TiO_3$ (BST 50/50) films [40].

Levasseur et al. [57] prepared BST 50/50 films on platinized silicon substrates by Chemical Solution Deposition and a single annealing. By increasing the annealing temperature from 600 °C to 800 °C the grain size of the approximately 250-nm-thick films increased from 30 nm to 150 nm. Consequently, the kHz-range dielectric permittivity increased from 170 to 280.

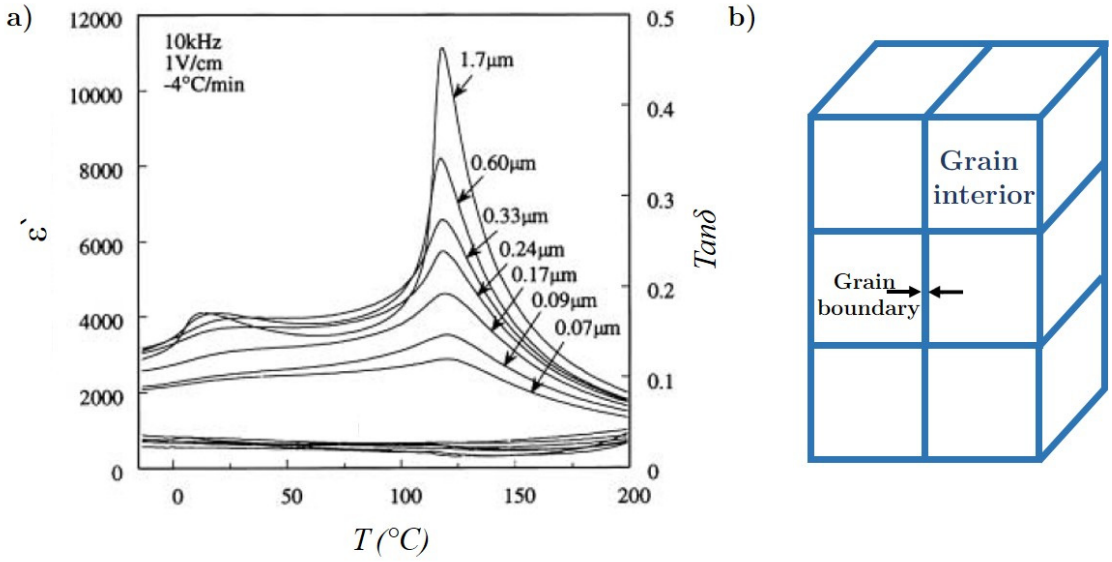


Figure 1.19: a) Temperature dependence of the dielectric permittivity and losses of $BaTiO_3$ ceramics with grain sizes in the range from 0.07 µm to 1.7 µm. b) Schematics of the brick-wall model consisting of the low-permittivity grain-boundary layer and high-permittivity grain interiors [63].

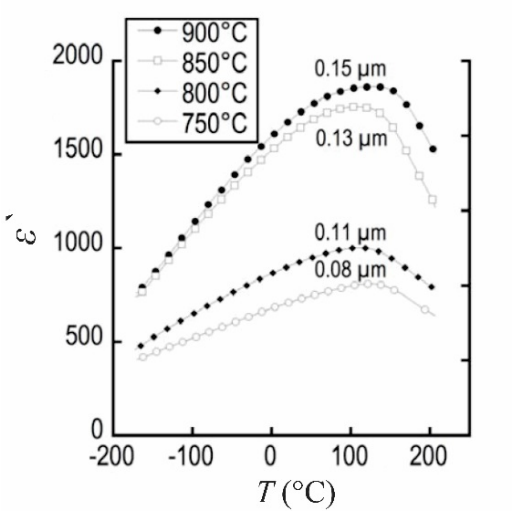


Figure 1.20: Temperature-dependent dielectric permittivity of $BaTiO_3$ thin films with grain sizes from 80 nm to 150 nm, prepared at different annealing temperatures [66].

In the case of thin films the grain-size effect is strongly connected to the film thickness [40], [45], [46], [56], [65], [68]. Sinnamon et al. [46] prepared columnar BST 50/50 thin films on $SrRuO_3$/MgO substrates by pulsed-laser deposition. As the film thickness increased from ~15 nm to ~1 µm the grain size increased from ~80 nm to ~460 nm. Such an increase resulted in an increased room-temperature dielectric permittivity from approximately 50 to 750, as presented in Figure 1.21. A lower dielectric permittivity of the thinner films is explained by the existence of a low-permittivity layer at the grain boundaries [63] rather than at the interface between the film and the electrode. The results of the proposed model showed a good correlation with the experimental data. The same trend of increasing grain size with increasing film thickness was also observed for the BST 50/50 films prepared by sputtering. As the film thickness increased from 50 nm to 300 nm, the grain size also increased from 32 nm to 80 nm. Consequently, the kHz-range dielectric permittivity increased from 348 to 758 [40] .

In addition to the grain size and film thickness other factors such as the interaction with the electrodes (i.e., the electrode effect [38]), porosity [69], chemical homogeneity [70], texture [47], [52], [71] and the type of microstructure [50] as well as interactions with the substrates causing residual stresses [42], [48], [72], [73] should also be considered when designing ferroelectric thin films.

The presence of residual stress is an important parameter that distinguishes thin films from their bulk counterparts. The stress may originate from specific growth conditions (growth stresses), defects present in the film, lattice mismatch between the film and the substrate (epitaxial stress) and the mismatch in the thermal expansion coefficients (TECs) between both (thermal stress) [74].

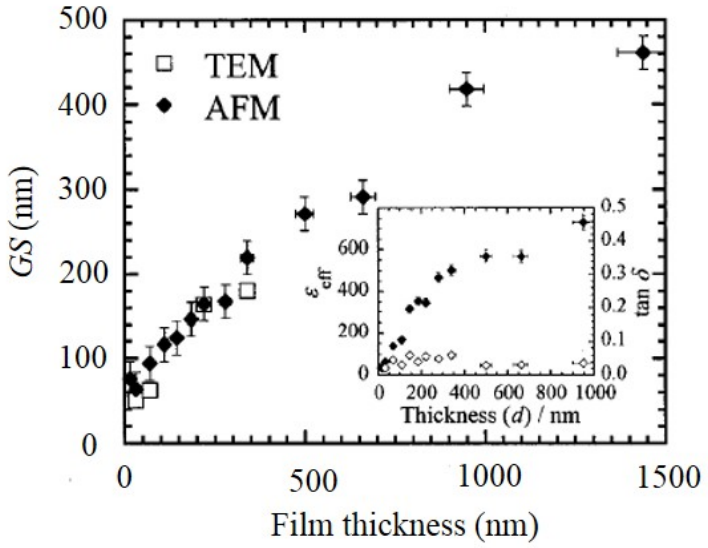


Figure 1.21: Thickness-dependent grain size (GS) for $Ba_{0.5}Sr_{0.5}TiO_3$ thin films prepared by PLD. Inset of the graph represents the dielectric properties of the films measured at 100 kHz [46].

The stress dependence of the tunable dielectric properties of ferroelectric thin films has also attracted attention. In particular, Ito et al. [44] prepared 200-nm-thick (100)-oriented BST 50/50 thin films on different substrates with different thermal expansion coefficients, where all of the substrates had a $SrRuO_3$ bottom electrode. A linear increase in the kHz permittivity with an increasing thermal expansion coefficient of the substrate was observed, as shown in Figure 1.22 a). In Figure 1.22 b) a similar dependence was also observed for the tunability [44]. Interestingly, the result is not in agreement with the phenomenological calculations, from which a non-monotonic tunability stress dependence is predicted due to an electric-field-induced paraelectric-ferroelectric phase transformation [75].

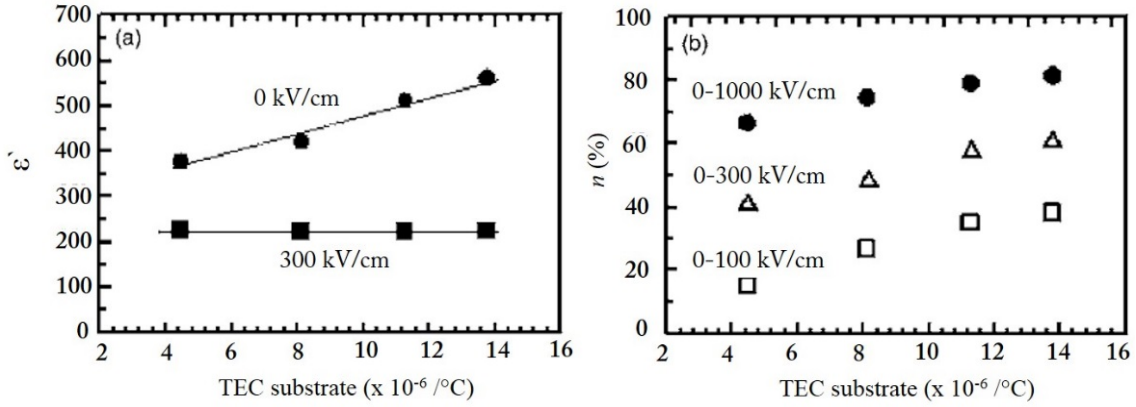


Figure 1.22: a) Relative dielectric constant measured at 0 kV and 300 kV and b) dielectric tunability under different applied electric field amplitudes for BST 50/50 films deposited on different substrates as a function of the thermal expansion coefficient (TEC) of the substrate [44].

Chapter 2

Aims and Hypothesis

In functional oxide thin films different effects, such as the grain size, film thickness, residual stress, porosity, interaction with the electrodes, etc., strongly affect their functional properties. Due to the complexity of the respective influences, it is still difficult to predict the exact functional response of the films. For this reason the relationship between the processing-related film characteristics and the functional properties of the films, with an emphasis on the evolution of the microstructure, are addressed in this thesis.

The grain size is coupled with the film thickness and it usually increases with an increasing thickness, resulting in improved dielectric, piezoelectric and ferroelectric properties of the films. Our main hypothesis for the first part of the thesis has been that the dielectric permittivity and the voltage tunability of the $Ba_{0.5}Sr_{0.5}TiO_3$ (BST 50/50) films can be tuned by the film thickness in a selected thickness range. In addition to the film thickness and the grain size, also the residual thermal stress, which develops upon cooling from the high processing temperatures, importantly impacts on the functional properties of the films. Therefore, our aims for the first part are:

- To investigate the influence of the film thickness and consequently also the grain size on the dielectric properties of the films in the kHz and GHz frequency ranges.
- To study the influence of the residual thermal stress in BST 50/50 thin films on their dielectric properties.

Since the microstructure is one of the factors that strongly influence the functional properties of the films, we focus on the crystallization and evolution of the microstructure of BST 50/50 films in the second part of the thesis. The evolution of the microstructure was followed after multi-step annealing the films for different temperatures and times. The main hypothesis for this part is that the granular microstructure evolves when the films are prepared by annealing the individual deposited layers of a given thickness with the layer thickness being much larger than the grain size at lower annealing temperatures ($\leq$800 °C in our case), while the columnar microstructure forms only at sufficiently high temperatures ($\geq$880 °C) when the grain size exceeds the individual layer thickness.
The principal aims of this part of the thesis are:

- To investigate the crystallization and microstructural evolution of BST 50/50 thin films on polycrystalline alumina substrates upon multi-step annealing at different temperatures and times.
- To establish the relationship between the processing conditions (layer thickness, crystallization temperature) and a specific type of film microstructure.
- To verify whether our results are in agreement with the structural zone model for solution-derived thin films. The latter relates the type of the microstructure, i.e., granular, layered and columnar, to the intrinsic crystallite or grain size, single layer thickness and annealing temperature.

Chapter 3

Materials and Methods

3.1 Preparation of the Films

3.1.1 Synthesis of the solution

For the synthesis of the $Ba_{0.5}Sr_{0.5}TiO_3$ (BST 50/50) solution barium acetate, strontium acetate and titanium butoxide were used as the reagents, and acetic acid and 2-methoxyethanol were used as the solvents. All the chemicals were stored and manipulated in the glove-box with a dry nitrogen atmosphere. Their characteristics are collected in Table 3.1.

Table 3.1: Chemicals used for the synthesis of the BST 50/50 solution.

Name	*Chemical Formula*	*Purity (%)*	*Supplier*
Barium acetate	$Ba(CH_3COO)_2$	99.999	Alfa-Aesar
Strontium acetate	$Sr(CH_3COO)_2$	99.81	Alfa-Aesar
Titanium(IV) butoxide	$Ti(OCH_2CH_2CH_2CH_3)_4$	99.61	Fluka
Acetic acid	CH_3COOH	100	Merck
2-methoxyethanol	$CH_3OCH_2CH_2OH$	99.3+	Sigma Aldrich

The synthesis began with the dissolution of 20 mmoles of alkaline-earth acetates in 24 ml of acetic acid in an erlenmeyer flask and 20 mmoles of titanium butoxide in 16 ml of 2-methoxyethanol in another flask. The flask with the titanium butoxide solution was connected to a modified Schlenk apparatus [76] and purged with dry nitrogen for 15 min under constant stirring with a magnetic stirrer. When the acetates were completely dissolved they were added to the titanium butoxide solution. The solution was than stirred for 2 h at room temperature and its concentration was adjusted to 0.4 M with a mixture of 2-methoxyethanol and acetic acid in a 2:3 volume ratio. The solution was stored in a refrigerator and remained clear for months. The concentration of the coating solution was finally adjusted to 0.25 M.

3.1.2 Substrate

The polycrystalline alumina substrates (Coorstek, Golden, USA) were 266 µm thick with a relative density above 97 % and a grain size below 1 µm [77]. Prior to the deposition each substrate was ultrasonically cleaned in acetone, isopropanol and deionized water and dried by a flow of N_2.

The X-ray diffraction (XRD) pattern of an alumina substrate is presented in Figure 3.1. The peaks at $2\theta \approx 19.0$ °, 25.5 °, 31.3 °, 35.2 °, 36.9 °, 37.7 °, 41.7 °, 43.4 °, 44.9 ° and 46.2 ° correspond to the reflections of the substrate [78]. The XRD pattern of a BST 50/50 film on the alumina substrate is also added. The BST 50/50 perovskite phase was identified using the crystallographic card from the JCPDS (Joint Committee on Powder Diffraction Standards) database [79]. Since the intensities of the diffraction peaks that correspond to the substrate are much higher than the intensities of the perovskite BST 50/50 phase, the peaks of the substrate were subtracted and are subsequently denoted by *.

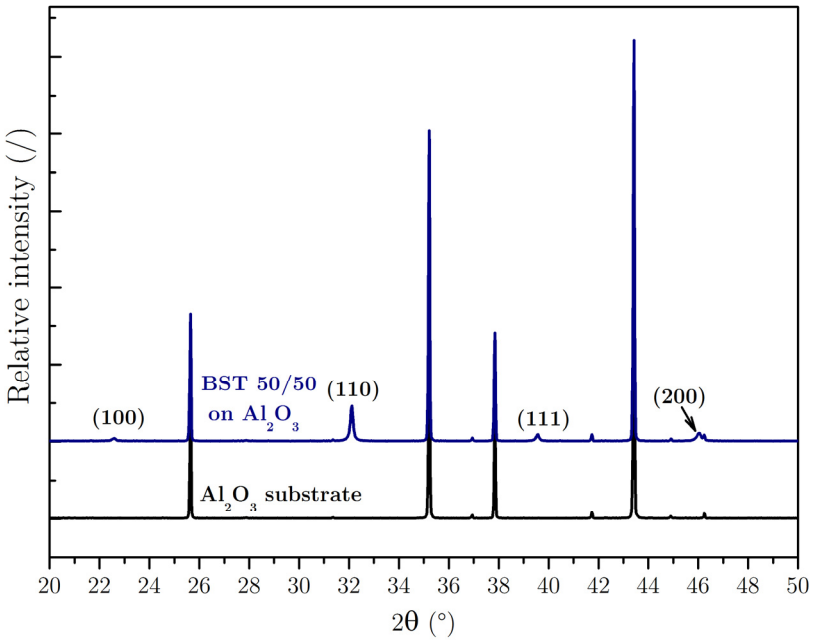


Figure 3.1: XRD pattern of an alumina substrate and BST 50/50 film deposited on such a substrate. The reflections of the perovskite phase are denoted with Miller indices [79].

3.1.3 Deposition of the films

In a typical experiment the solution was deposited on a 1 inch × 1 inch polished polycrystalline alumina substrate. The 0.25-M solution was passed through a 0.2-µm filter and spin coated on the substrate for 30 s at 3000 rpm using a Headway Research 1-EC101D-R485 photoresist spinner. The as-deposited film was firstly heated at 200 °C for 2 min on a hot plate to remove the solvents. Secondly, the film was pyrolyzed at 350 °C for 2 min on a hot plate in order to remove the organics. The final annealing was performed at temperatures from 600 °C to 900 °C in an LPT Industries Europe TM 100-BT, RTA furnace with a heating rate of 15 K/s and a cooling time of ~10 min in a constant flow of N_2 and O_2 in a 4:1 ratio.

The films were prepared by two different annealing processes. In the case of the two-step annealing process the first deposit was dried, pyrolyzed and annealed for 15 min. Then the deposition-drying-pyrolysis steps were repeated six times, followed by the final annealing for 60 min (see Figure 3.2 a)). The final thickness of the films was approximately 300 nm.

In the case of the multi-step annealing process the deposition-drying-pyrolysis-annealing steps were repeated for each individual deposit (see Figure 3.2 b)). The time of annealing of the first deposit was 15 min (in selected cases also 1, 5, 30 and 60 min), the intermediate

deposits were annealed for 5 min and the final deposit for 1 s to 60 min, resulting in film thicknesses from 40 nm to 600 nm, depending on the number of the deposition-drying-pyrolysis-annealing steps.

As a reference the BST 50/50 solution was dried at 60 °C overnight to yield a gel, which was heated in air to 900 °C with a rate of 10 K/min (STA 409, Netzsch, Selb, Germany). The sample is referred to as the bulk-gel.

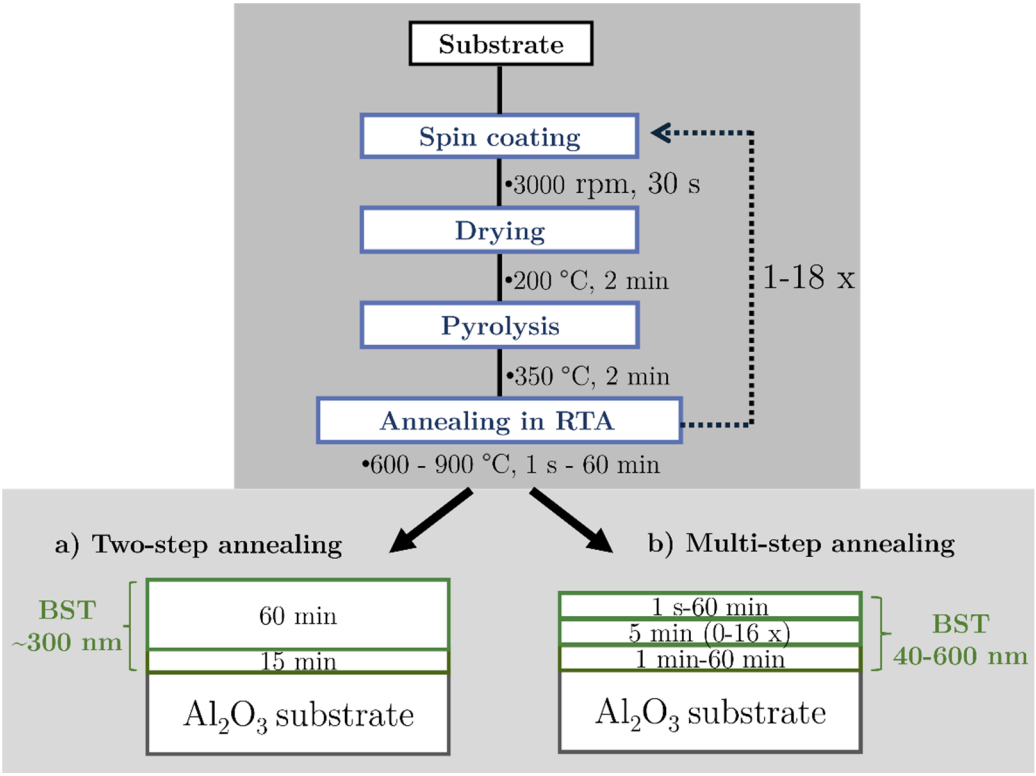


Figure 3.2: Schematic presentation of the thin-film deposition. a) In the two-step annealing process the first layer was deposited, dried, pyrolyzed and annealed for 15 min. Then the deposition-drying-pyrolysis steps were repeated for six deposited layers and finally the films were annealed for 60 min. b) In the multi-step annealing process the deposition-drying-pyrolysis-annealing steps were performed for each individual deposit for different times and repeated until the required thickness was reached.

3.1.4 Patterning of planar capacitors by lift-off photolithography

A schematic presentation of the main processing steps of the planar capacitor electrodes by lift-off photolithography is presented in Figure 3.3. The BST 50/50 films were firstly cleaned in H_2O, NH_3 and H_2O_2 solution with the volume ratio 6:1:1 and heated at 50 °C for 10 min. Then the films were rinsed by deionized water and dried on a hot plate at 200 °C for 10 min.

In the next step a 3.5-µm-thick layer of the negative photoresist (AZ nLOF 2035, Microchemicals GmbH, Germany) was spin-coated on the surface of the film with an increasing rotation speed from 500 to 5000 rpm for a duration of 60 s. The photoresist was dried on a hot plate at 105 °C for 90 s.

Then the film, covered with the photoresist layer, was exposed to ultraviolet (UV) light through a mask, which included the patterns of the planar capacitor electrodes, as shown in Figure 3.4. The exposure step was concluded by drying on a hot plate at 105 °C for 60 s.

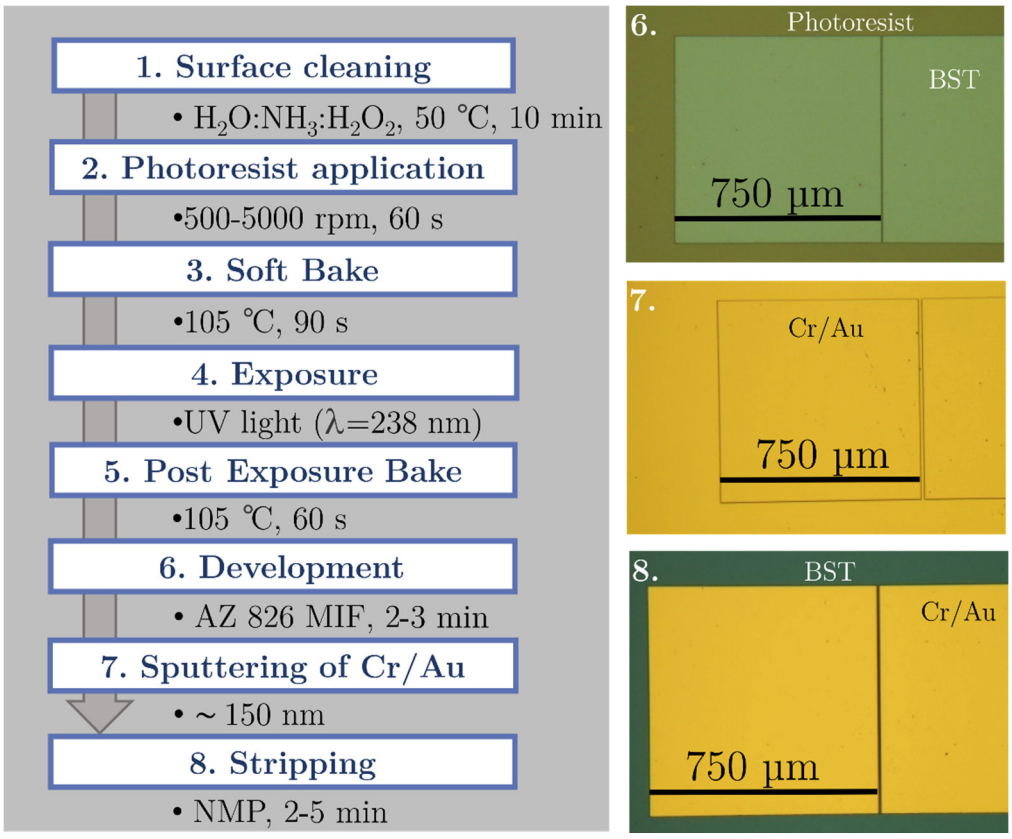


Figure 3.3: Schematic presentation of the basic processing steps for patterning of the planar capacitor electrodes by lift-off photolithography. Optical micrographs of a part of the planar capacitor structure after the developing step (6.), after sputtering of Cr/Au (7.) and after the final lift-off process (8.).

The next step was to develop the desired structure by UV activation. According to the pattern of the planar capacitor only selected regions of the structure were exposed to UV-light. In such regions the negative photoresist was dissolved in the developer (AZ 826 MIF, Microchemicals GmbH, Germany). In the regions where the photoresist had not been exposed to the UV-light it remained on the sample surface, as presented in the optical micrograph of the part of the structure after the developing step in Figure 3.3, step 6.

In the next step, the about 150-nm-thick layer of Cr and Au (30 nm Cr, 120 nm Au) was deposited by magnetron sputtering (5 Pa, Milano, Italy) over the entire surface of the film, as shown in Figure 3.3, step 7. Finally, in the stripping step the residual metallized photoresist was dissolved in the stripper (N-Methyl-2-pyrrolidone, NMP, Microchemicals GmbH, Germany) for 2 min to 5 min. The metal deposited directly on the BST 50/50 surface remained, yielding the desired structure of the planar capacitor electrodes with a 3-µm-sized gap. An optical micrograph of a part of the final structure is presented in Figure 3.3, step 8.

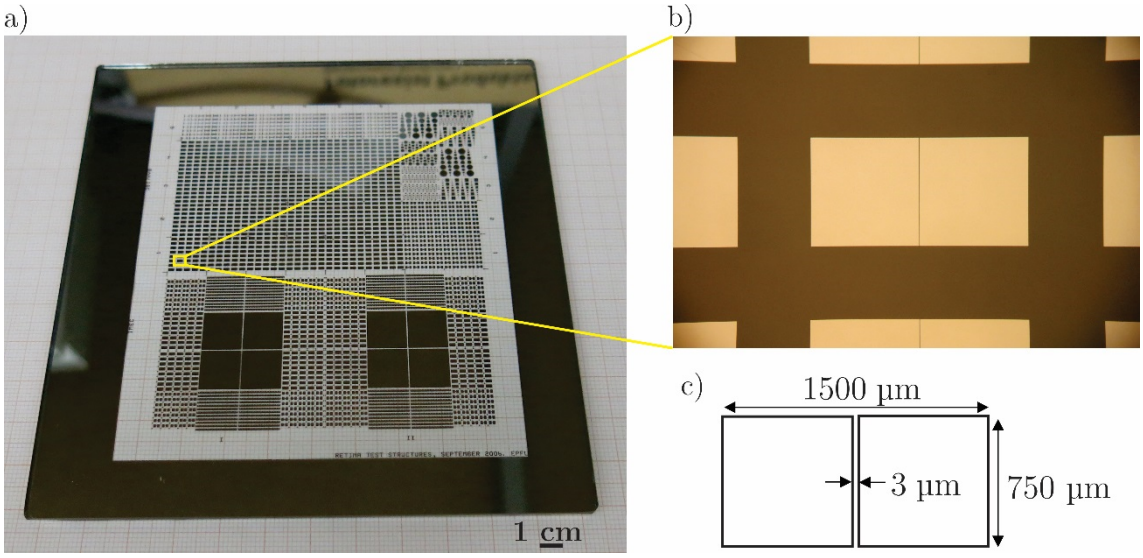


Figure 3.4: a) A photograph of the mask for the photolithography process with the patterns of the planar capacitor electrodes. b) Enlarged optical micrograph of the pattern of the planar capacitor electrodes used in this thesis and c) schematics showing the dimensions of the used electrodes.

3.2 Characterization

3.2.1 X-Ray diffraction

The phase composition of the thin films was analyzed with an X-ray diffractometer (X'Pert PRO MPD, PANalytical, Almelo, Netherlands) using Cu–Kα_1 radiation. The XRD patterns were recorded in the diffraction angle (2θ) region from 10 ° to 70 ° using a 1D detector (X'Celerator, PANalytical, Almelo, Netherlands) with a capture angle of 2.122 °. The exposure time for each step was 100 s and the interval between the obtained data points was 0.017 °. The phases were identified with the X'Pert HighScore software (Version 2.1b, PANalytical, Almelo, Netherlands) using the PDF-2 database [80].

The crystallite sizes (L) of the BST 50/50 thin films were determined using the Scherrer equation:

$$L = \frac{K\lambda}{\beta \cos\theta}, \tag{3.1}$$

where K is a constant related to the crystallite shape, normally taken as 0.9, λ is the X-ray wavelength and β is the full width at half maximum. For the determination of the β of the diffraction peaks the profile fitting software Peakoc was used and the Pseudo-Voigt function was used to refine the peak profiles.

The preferential orientation of the films can be quantified using the Lotgering factor $f_{(00l)}$ [81]:

$$f_{(00l)} = \frac{P_{(00l)} - P_0}{1 - P_0}, \tag{3.2}$$

where $P_{(00l)}$ and P_0 represent the ratios of the sum of the intensities of the (00l) reflections and the (hkl) reflections in a certain 2θ range in the oriented material ($P_{(00l)}$) and in a non-oriented material (P_0), respectively. The Lotgering factor ranges from 0 for a randomly oriented material to 1 for a fully oriented material.

For the calculation of the Lotgering factor for BST 50/50 thin films, the sum of the intensities of the peaks belonging to the same family of crystal planes was defined using the profile-fitting Software Peakoc. The Pseudo-Voigt function was used to refine the peak profiles.

3.2.1.1 Residual stress analysis

The residual-stress analysis was performed using a Bruker D8 Discover diffractometer with Cu–Kα_1 radiation (Bruker Corporation, Billerica, USA) equipped with a VÅNTEC-500 two-dimensional (2D) detector in collaboration with Brown University, Providence, USA. The measurements were performed in the ∼17 ° to 47 ° and ∼-62 ° to -116 ° 2θ and γ regions, respectively. The films were tilted in the ψ-range from 0 ° to 60° with a step of 6 °. At each ψ-angle the samples were rotated around their normal (ϕ-angle) by 360 ° with a step of 45 °. The acquisition time for each measurement was 100 s.

A quantitative analysis of the residual stress was performed using the LEPTOS Software (Bruker Corporation, Billerica, USA). The measured γ-range was divided into ten sub-ranges and the (110) peaks of the BST, obtained by integration, were fitted with the Pseudo-Voigt function. In this way ∼800 points were generated for each sample. The final stress values were calculated from the set of fundamental equations linking the stress-

tensor components to the diffraction-cone distortions using a least-squares regression [82]. A Young's modulus E of 80 GPa [83] and a Poisson's ratio ν of 0.3 were used.

The residual stress analysis using the 2D-XRD method is summarized in Appendix B and further details of the analysis can be found in Ref. [82].

3.2.2 Scanning electron microscopy

The surface and cross-section microstructures of the films were analyzed with a Field-Emission Scanning Electron Microscope (FE-SEM, JSM-7600F, JEOL, Tokyo, Japan). For the plane-view analysis the films were cut into ~2 mm × 2 mm pieces and mounted with graphite paste on top of the brass holders, while for the cross-sectional analysis the fracture surfaces were positioned in parallel with the surface of the holder. Approximately 5 nm of carbon was deposited on the top of the films using a Gatan Precision Etching Coating System (PECS) Model 682A.

The average lateral grain sizes of the films, calculated as the Feret's diameter, and their standard deviations were determined with a stereological analysis of the surface micrographs on ~350 grains using the ImageTool software (University of Texas Health Science Center at San Antonio, USA).

3.2.3 Atomic force microscopy

Atomic Force Microscope (AFM, Asylum Research Molecular Force Probe 3D, MFP-3D-S™, Santa Barbara, California) was used to analyze the surface morphology of the films. The topography (height and deflection images) was investigated in the contact mode using Pt/Ir-coated silicon tips (NANOSENSORS™, Neuchatel, Switzerland). The AFM surface profiles were taken from the height images of the surfaces.

The vertical surface roughness of the thin films was calculated for an area of 1 µm × 1 µm in terms of the root-mean-squared roughness (RMS) using AFM software (Igor Pro 6.34A).

3.2.4 Focused ion beam

A Focused Ion Beam (FIB, Helios NanoLab 600i, FEI, Oregon, USA) was used to prepare the films for the cross-sectional analysis by Transmission Electron Microscopy. The film was glued on a holder with carbon paste and the surface was sputtered with a thin layer of carbon using a Gatan Precision Etching Coating System (PECS) Model 682A. The FIB instrument was then used firstly to deposit the about 100-nm-thick layer of Pt with the electron beam followed, by the deposition of an about 2-µm-thick Pt layer with the ion beam. Next, the lamella was milled from the bulk surface of the film and then removed from the film. An approximately 2 µm × 3 µm electron-transparent lamella was transferred and attached to the copper TEM grid. Finally, the lamella was thinned to a thickness of approximately 100 nm and cleaned using the ion beam at a low voltage.

3.2.5 Transmission electron microscopy

For the microstructural analysis two Transmission Electron Microscopes were used. The Jeol 2010F (Jeol, Tokyo, Japan) equipped with ISIS 300 EDS (Oxford Instruments, Abingdon, United Kingdom) EDXS detector, subsequently referred to as a TEM. For the TEM analysis of the cross-section microstructure of thin films, the films were cut with a diamond saw (Well Diamond Wire Saws, Norcross, Georgia, USA), glued face-to-face and mounted in Ti-rings with epoxy. Then conventional grinding, polishing and dimpling were performed, followed by the final Ar^+ ion milling with liquid-nitrogen cooling.

The Cs-corrected JEM-ARM200CF (Jeol, Tokyo, Japan) was used for the high-angle annular dark-field scanning transmission electron microscopy (HAADF-STEM) imaging at the atomic level in collaboration with the National Institute of Chemistry, Ljubljana, Slovenia. For the HAADF-STEM analysis the thin-film lamella was prepared with the FIB instrument (see Section 3.2.4).

3.2.6 Dielectric spectroscopy

3.2.6.1 Measurements in the kHz frequency range

For the kHz-range dielectric characterization, the 750 × 750 µm^2 planar capacitors with 3-µm gaps were patterned using the lift-off photolithography, as explained in 3.1.3. A schematic presentation of the structures is shown in Figure 3.4 and Figure 3.5. The 150-nm-thick Cr/Au electrodes were deposited using magnetron sputtering (5Pascal, Milano, Italy).

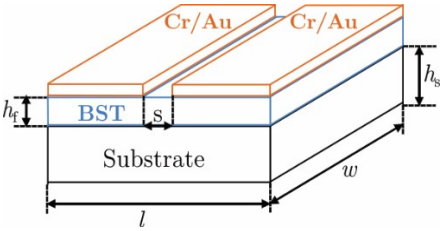


Figure 3.5: Schematic presentation of a planar thin-film capacitor. h_f and h_s – thickness of the film and the substrate, respectively; s – gap between the electrodes; l – length of the electrodes; w – width of the electrodes. *After* [84].

The room-temperature capacitance and dielectric losses of the films were measured using an impedance analyzer (HP 4284 A, Keysight, Santa Rosa, USA) in the frequency range from 100 Hz to 1 MHz with an amplitude of the probing AC signal equal to 0.5 V. The capacitance-voltage characteristics at 100 kHz were determined with the following DC-biasing scheme: 0 V → + 40 V → 0 V → - 40 V → 0 V.

Dielectric properties were measured as a function of a DC-electric field at 5 kHz in the temperature range between 298 K and 503 K using a TF Analyzer 2000 E (AixaCCT, Aachen, Germany), in collaboration with the Faculty of Physics, Vilnius University. The heating rate was 7 K/min and the amplitude of the probing AC signal was 0.5 V. The electric field, approximated as the voltage divided by the gap between the two planar electrodes, was applied with the following scheme: 0 kV/cm → 80 kV/cm → 0 kV/cm → - 80 kV/cm → 0 kV/cm.

The temperature dependence of the capacitance and the dielectric losses of the films in the frequency range between 100 Hz and 1 MHz was measured using the Alpha High-Resolution Dielectric Analyzer (Novocontrol Technologies GmbH & Co. KG, Montabaur, Germany), in collaboration with the Condensed Matter Physics Department, Jožef Stefan Institute. The films were cooled from 400 to 100 K with a rate of 1 K/min and the amplitude of the probing AC signal was 0.5 V.

To evaluate the dielectric properties of the films the modified partial capacitance method (PCM) [84], [85] was employed, where the dielectric permittivity ε_f of the films was calculated from the measured capacitance as:

$$\varepsilon_f = \varepsilon_s + (\frac{s}{h_f} + \frac{4}{\pi} ln2)(\frac{C_m}{\varepsilon_0 w} - \frac{2}{\pi} \ln\left(\frac{4l}{s}\right) - \frac{\varepsilon_s - 1}{\pi} \ln\left(16 \frac{h_s + h_f}{\pi s}\right)) \tag{3.3}$$

where ε_s is the permittivity of the alumina substrate, s is the gap between the electrodes, h_f is the thickness of the film, ε_0 is the permittivity of vacuum, w is the length of the electrode, l is the width of the electrode and h_s is the thickness of the substrate.

3.2.6.2 Measurements in the GHz frequency range

Split-post dielectric resonators (QWED, Warsaw, Poland) connected to a network analyzer (HP 8720 ES, Keysight, Santa Rosa, USA) were used for the analysis of the dielectric properties of the BST 50/50 films at 10 GHz and 15 GHz in collaboration with the Condensed Matter Physics Department, Jožef Stefan Institute. Firstly, the resonator was measured, then the resonator with the substrate and finally the resonator with the film on the substrate.

The dielectric permittivity and dielectric losses of the thin films were evaluated from the resonant frequency and the quality factor by numerical calculations based on the electrodynamic analysis [86] using the software provided by the resonator's supplier.

The temperature dependence of the microwave dielectric properties of the films were measured at 15 GHz on cooling from 375 K to 170 K with a rate of 3 K/min, in collaboration with the School of Electronic and Information Engineering, Xi'an Jiaotong University, China. The 15-GHz resonator was placed in a Delta Design 9023 chamber (Cohu, San Diego, California) and was connected to an HP 8720 ES network analyzer (Keysight, Santa Rosa, USA).

Chapter 4

Results and Discussion

4.1 $Ba_{0.5}Sr_{0.5}TiO_3$ Thin Films with Different Thicknesses

In the first part of this chapter we study the BST 50/50 films that were prepared by the multi-step annealing process at 900 °C on polycrystalline alumina substrates. The thicknesses of the films were in the range from 90 nm to 600 nm. Firstly, the microstructures and phase compositions of the films are shown, and secondly, the dielectric properties of the films measured in the kHz and GHz frequency ranges are discussed.

4.1.1 Microstructure and phase composition

The FE-SEM cross-section and surface micrographs of representative BST 50/50 films with different thicknesses are shown in Figure 4.1. The cross-section microstructure of the thinnest, 90-nm-thick film, consists predominantly of one grain through the film thickness. The surface microstructure is uniform with an average lateral grain size of approximately 45 nm. Fine pores between the grains are also observed.

The columnar microstructure of the BST 50/50 films is, to a large extent, retained as the thickness increases to 170 nm, and further to 600 nm, as shown in Figure 4.1. However, some equiaxed grains are also observed in all the films. The surface microstructures of the 170-, 310-, 400- and 600-nm-thick films are dense and uniform. The average lateral grain size increases with the film thickness from approximately 75 nm for 170-nm-thick films, to ~100 nm for 600-nm-thick films. Note that some intergranular nano-cracks are observed in the thicker films and are marked with arrows on the surface the FE-SEM micrographs of the films.

Further details on the evolution of the columnar microstructure of the BST 50/50 films on alumina substrates prepared by a multi-step annealing process at 900 °C are discussed in the next sub-Chapter.

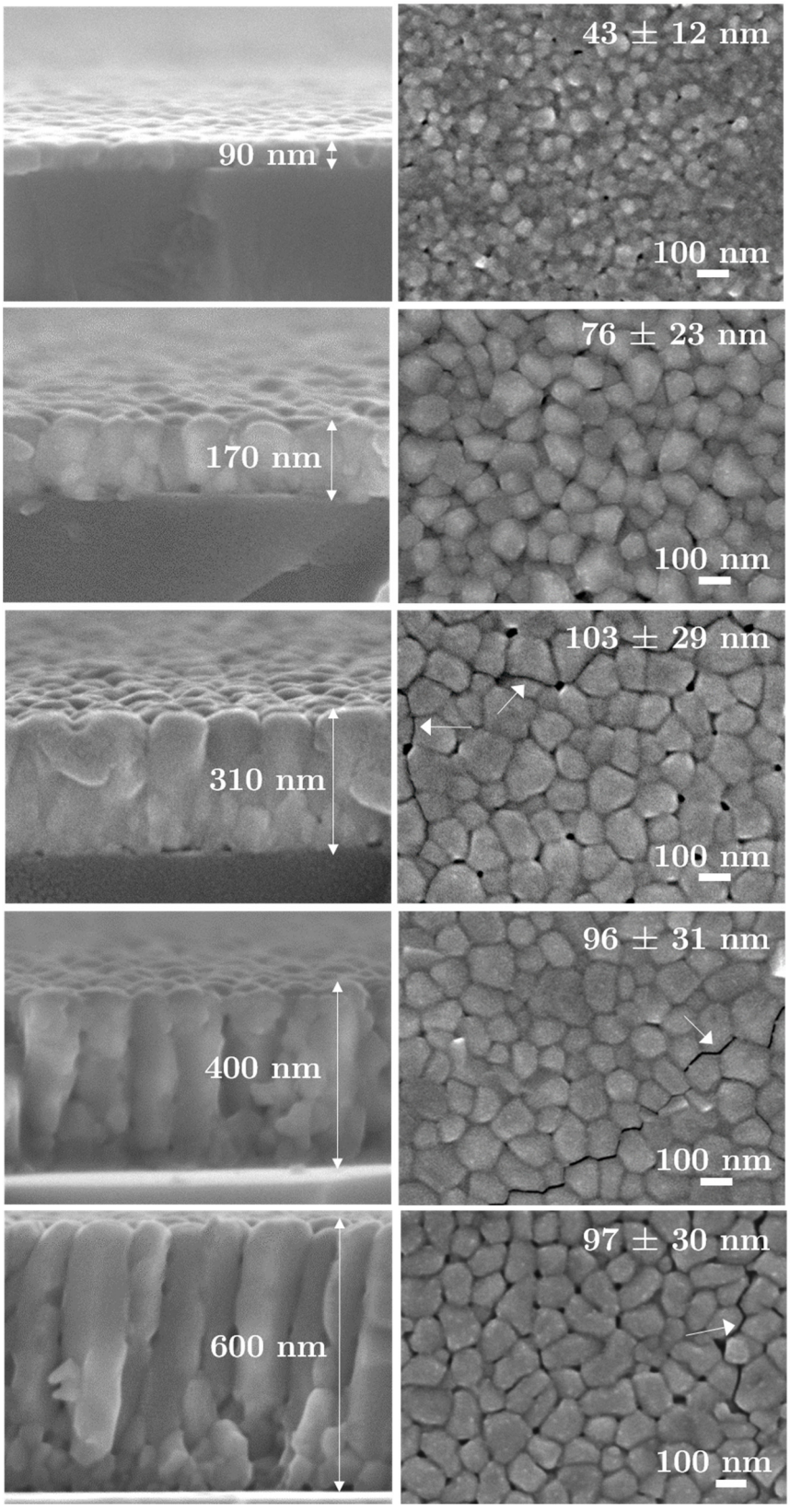


Figure 4.1: The FE-SEM cross-section and surface micrographs of the BST 50/50 films with the thicknesses between 90 nm and 600 nm. The average lateral grain sizes are included. The arrows in the surface micrographs mark nano-cracks in the thicker films.

The XRD patterns of BST 50/50 films with thicknesses in the range from 90 nm to 600 nm are presented in Figure 4.2. According to the XRD analysis all the BST 50/50 films crystallize in a pure perovskite phase upon annealing at 900 °C. The perovskite peaks were indexed according to the JCPDS database [79].

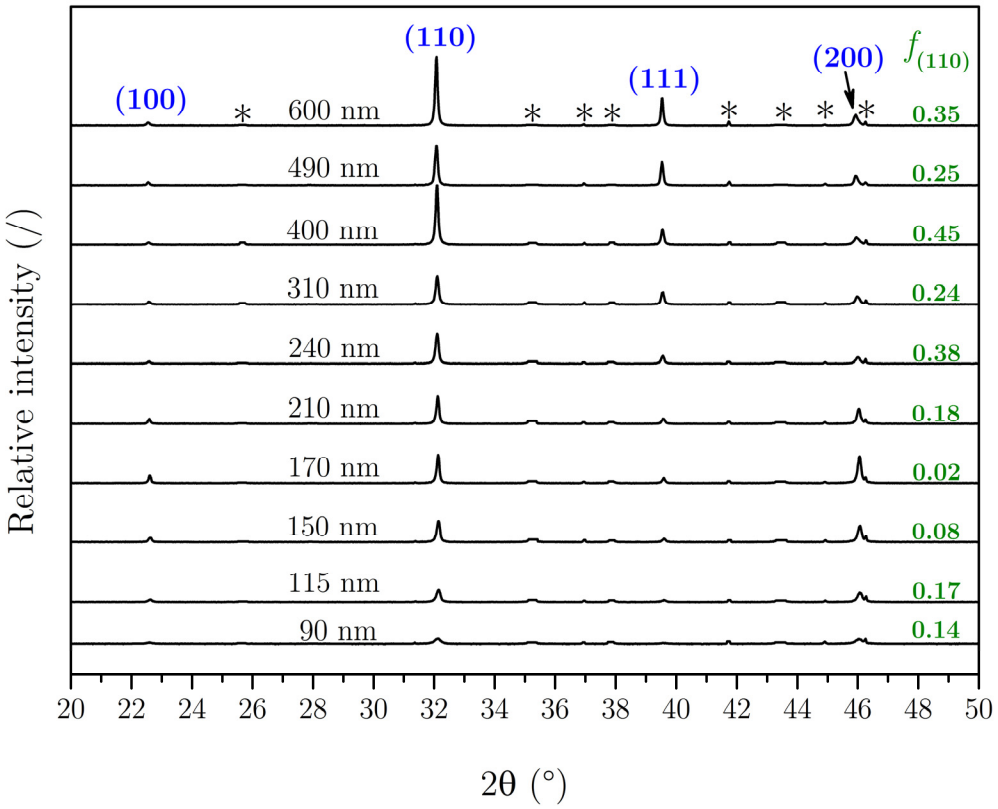


Figure 4.2: XRD patterns of the BST 50/50 films with the thicknesses between 90 nm and 600 nm, prepared on alumina substrates by multi-step annealing at 900 °C. The peaks corresponding to the perovskite phase are denoted with the Miller indices [79]. * - subtracted peaks of the alumina substrate. $f_{(110)}$ is the Lotgering factor, which expresses the degree of the preferential orientation of the BST 50/50 films.

A careful comparison of the intensities of the (110) and (200) diffraction peaks reveals a change in the degree of the preferred orientation with the increasing thickness of the films, which was quantified with the Lotgering factor $f_{(110)}$ for the (110) family of crystal planes, see Figure 4.2. The Lotgering factor is about 0.15 for the thinnest films and decreases to almost 0 for the 170-nm-thick film. With a further increase in the film thickness the Lotgering factor increases again, reaching 0.35 for the 600-nm-thick film. The Lotgering factors of the 240-nm- and 400-nm-thick films are relatively high.

The diffraction peaks of the perovskite BST 50/50 phase in a narrower 2θ range are shown in Figure 4.3. The dotted lines mark the peaks of the reference BST 50/50 bulk-gel sample heated in air at 900 °C. We can clearly observe that as the film thickness increases from 90 nm to 170 nm, the perovskite peaks shift towards higher 2θ angles relative to the positions of the peaks of the bulk-gel sample. But with a further increase in the thickness the shifting occurs in the opposite direction.

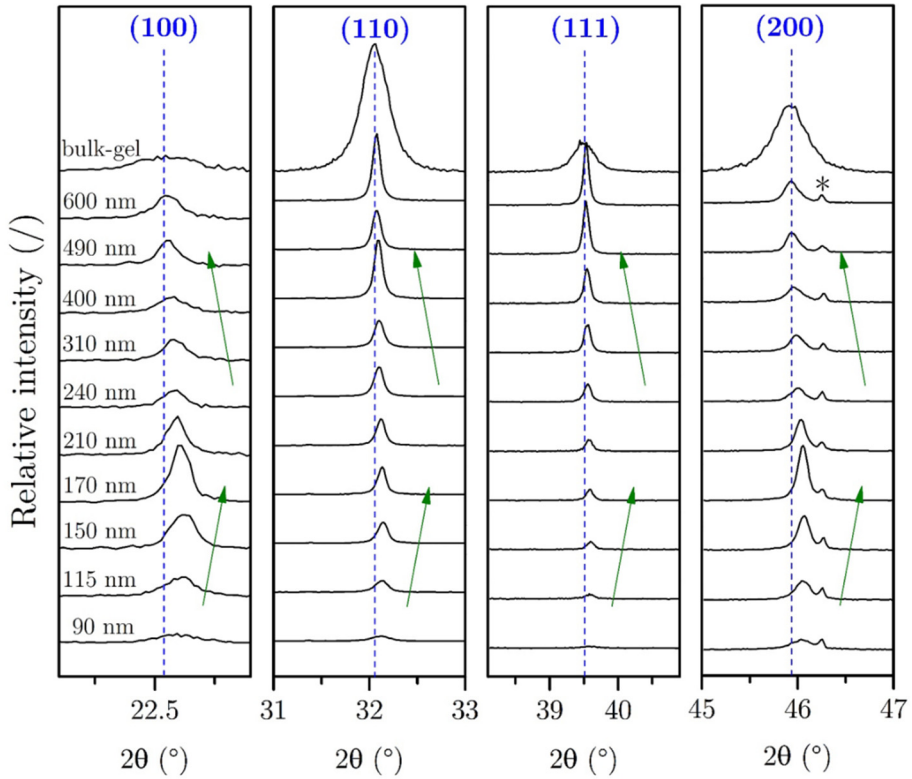


Figure 4.3: The (100), (110), (111) and (200) diffraction peaks of BST 50/50 thin films with thicknesses between 90 nm and 600 nm. Diffraction peaks of the BST 50/50 bulk-gel sample heated to 900 °C are added as a reference. The arrows indicate the shifting of the perovskite diffraction peaks. * - subtracted peaks of the alumina substrate.

As the films were processed under the same conditions, we relate the shifting of the peaks to the residual stresses that could be present in the BST 50/50 films. Therefore, a more detailed residual-stress analysis of the BST 50/50 films was performed.

The observed shifts of the perovskite peaks in Figure 4.2 and Figure 4.3 are rather small, making quantification of the residual stresses using the 1D XRD geometry unreliable, while an XRD method with a 2-dimensional detector (2D-XRD) offers improved statistics for the measurement. The 2D-XRD frames of the 170-nm-thick BST 50/50 film measured at different tilting ψ-angles, i.e., 0 °, 18 ° and 36 °, are shown in Figure 4.4 a). The (110) diffraction ring of the film is distinct in all the frames. Note that other strong rings correspond to the polycrystalline alumina substrate. The frames were integrated around this peak to obtain the conventional intensity-2θ diffraction patterns and the result is shown in Figure 4.4 b). The shift of the peak maxima towards a lower 2θ-angle with increasing ψ-angle is apparent. To evaluate the exact positions, the peaks were fitted with the Pseudo-Voigt function and the obtained lattice parameter d vs. $\sin^2\psi$ plot is shown in Figure 4.4 c). A linear increase of the in-plane lattice parameter with increasing ψ-angle is observed, indicating the tensile residual stress in the 170-nm-thick BST 50/50 film [82].

As described in detail in Section 3.2.1.1, the films were measured in the 0-60 ° ψ-range and in the 0-360 ° ϕ-range, where ϕ is the angle of rotation of the sample along its normal. Approximately 800 experimental points per sample were produced for the quantitative analysis of the stress. We did not observe any differences in the frames collected at different ϕ-angles, indicating that the biaxial stress was equal in all the BST 50/50 films with different thicknesses.

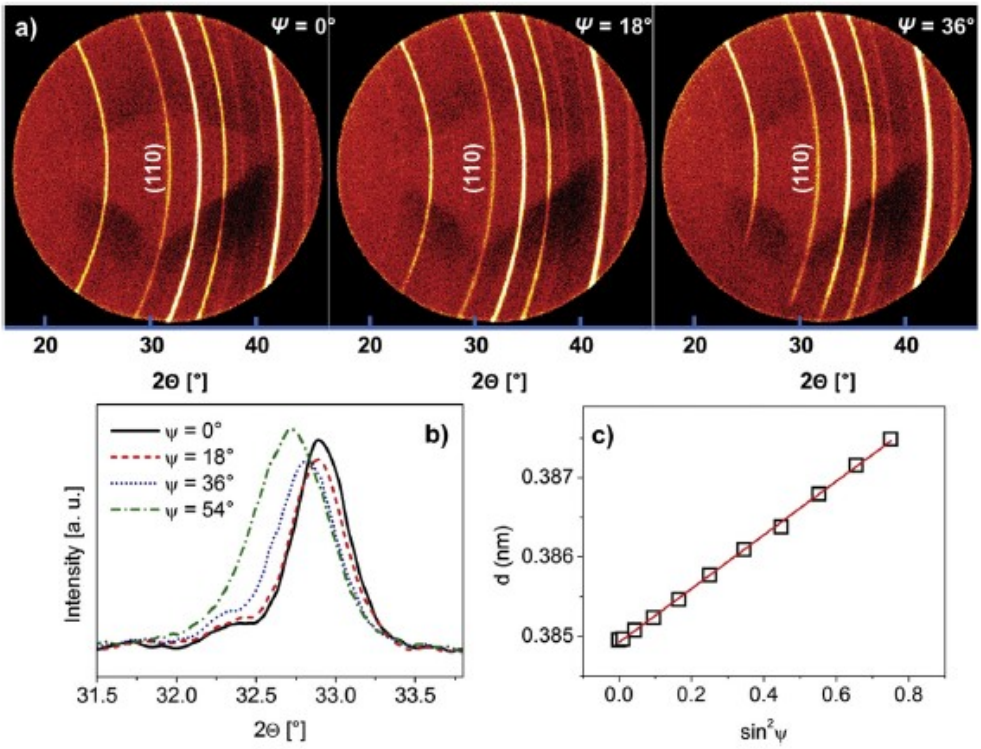


Figure 4.4: a) The 2D-XRD frames of the 170-nm-thick BST 50/50 film measured at different tilting ψ-angles, shown in the -62 ° to -116 ° γ-range, where γ is used to define the direction of the diffracted beam on the cone. The angle of the rotation (ϕ) of the sample along its normal was, in all cases, 0 °. The (110) diffraction rings of the BST 50/50 films are denoted and the other strong rings correspond to the Al_2O_3 substrate. b) The conventional XRD diffractograms around the (110) diffraction peaks obtained by the integration of the 2D frames in the γ-range from -73 ° to -107 °. c) The d vs. $\sin^2\psi$ plot obtained from the positions of the peaks calculated from the 2D frames. The red line is a linear fit to the experimental points.

The results of the 2D XRD stress analysis are collected in Table 4.1. All BST 50/50 films are under a significant tensile stress. The value is the highest in the thinner films, reaching 344 MPa in the 90-nm-thick film and 380 MPa in the 170-nm-thick film, respectively. The determined values of the tensile stress in the BST 50/50 films between 344 MPa and 378 MPa at 900 °C agree well with the literature. Taylor et al. [42] prepared BST 30/70 films on sapphire substrates by sputtering and annealing at 750 °C in oxygen. The thermal stress in the 100-nm-thick film was approximately 380 MPa, which agrees well with our results for 90-nm- and 170-nm-thick films.

With a further increase in the film thickness, the magnitude of the stress in BST 50/50 films sharply decreases to 198 MPa for the 240-nm-thick films and further to ~120 MPa in the 400- and 600-nm-thick films, respectively.

The tensile stress in the BST 50/50 thin films on polycrystalline alumina substrates is a consequence of the mismatch in the thermal expansion coefficients (TECs) of the substrate and the film, with values of ~8×10^{-6} /K [77] for the substrate and 10.5×10^{-6} /K [87] for the films. During cooling from the annealing temperature, the substrate shrinks less than the film, because the TEC of the substrate is lower than the TEC of the film.

Since the film is constrained by the substrate, the difference in TECs produces a tensile stress in the BST 50/50 film, as schematically shown in Figure 4.5.

When the film thickness reaches a critical value, the internal stresses frequently relax as a result of the deformation processes induced by the thermally activated motion of the atoms and the defects, resulting in hillock formation, cracking of the film or in delamination [74]. In our case, the stress relaxation occurs via the formation of intergranular cracks, as is evident from the surface micrographs of the thicker BST 50/50 films ($\geq$ 310 nm), shown in Figure 4.1 and at a lower magnification in Figure 4.6. Note that the cracks extend along many grains, extending up to the micron range. With an increasing film thickness from 310 nm to 600 nm the volume fraction of the cracks increases.

Table 4.1: Biaxial tensile stress of the BST 50/50 films with thicknesses in the range from 90 nm to 600 nm, as determined with the 2D $\sin^2\psi$ technique.

Film thickness (nm)	*Biaxial stress (MPa)*
90	344 ± 10
170	378 ± 7
240	198 ± 7
310	171 ± 7
400	120 ± 3
600	129 ± 5

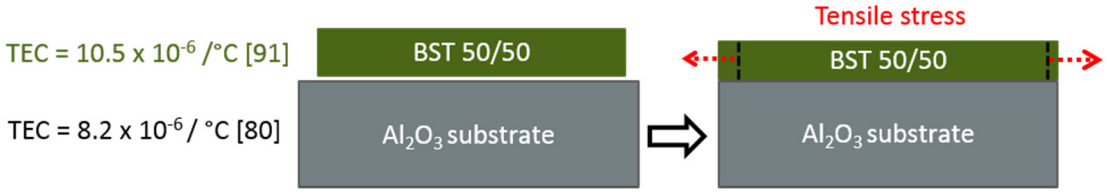


Figure 4.5: Schematics showing the tensile thermal stress induced in the BST 50/50 film on an alumina substrate due to the difference in the thermal expansion coefficients (TECs) of the film and the substrate.

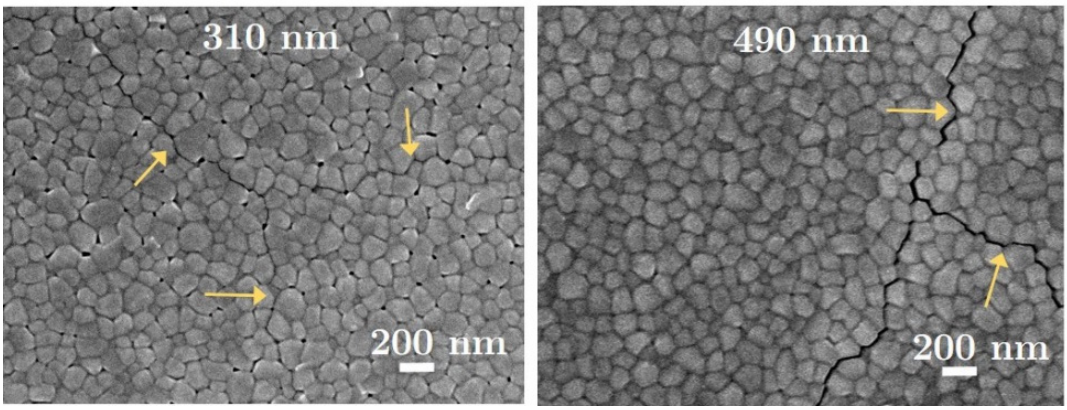


Figure 4.6: FE-SEM surface microstructures of the 310-nm- and 490-nm-thick BST 50/50 films. The arrows mark the cracks in the films.

4.1.2 Dielectric properties of the films

The room-temperature dielectric properties of BST 50/50 films with thicknesses in the range from 90 nm to 600 nm, measured at 100 kHz, 10 GHz and 15 GHz, are shown in Figure 4.7. The dielectric permittivity of the 90-nm-thick film is 650 at 100 kHz, and increases to 1300 as the film thickness increases to 170 nm. The permittivity remains approximately constant up to a thickness of 240 nm. With a further thickness increase to 600 nm the permittivity drops to 770. The kHz-losses of all the BST 50/50 films are below 0.02.

The GHz-permittivity follows a similar trend, although the values are slightly lower. The highest value of approximately 1300 at 15 GHz is observed for the 210-nm- and 240-nm-thick films. The GHz-losses range between 0.07 for the thinnest films and 0.16 at 15 GHz for the 210-nm-thick films. With a further increase of the film thickness the dielectric losses decrease to approximately 0.10 for the 600-nm-thick film.

The non-monotonic thickness dependence of the permittivity, shown in Figure 4.7 indicates that different effects control the permittivity value at different film thicknesses. In Figure 4.8 we plotted the average lateral grain size, the residual stress and the permittivity, measured at 100 kHz, as functions of the film thickness. The permittivity increases almost linearly in the thickness range between 90 nm and 170 nm from 650 to 1300, where the lateral grain size increases from 45 nm to 75 nm, respectively. The trend

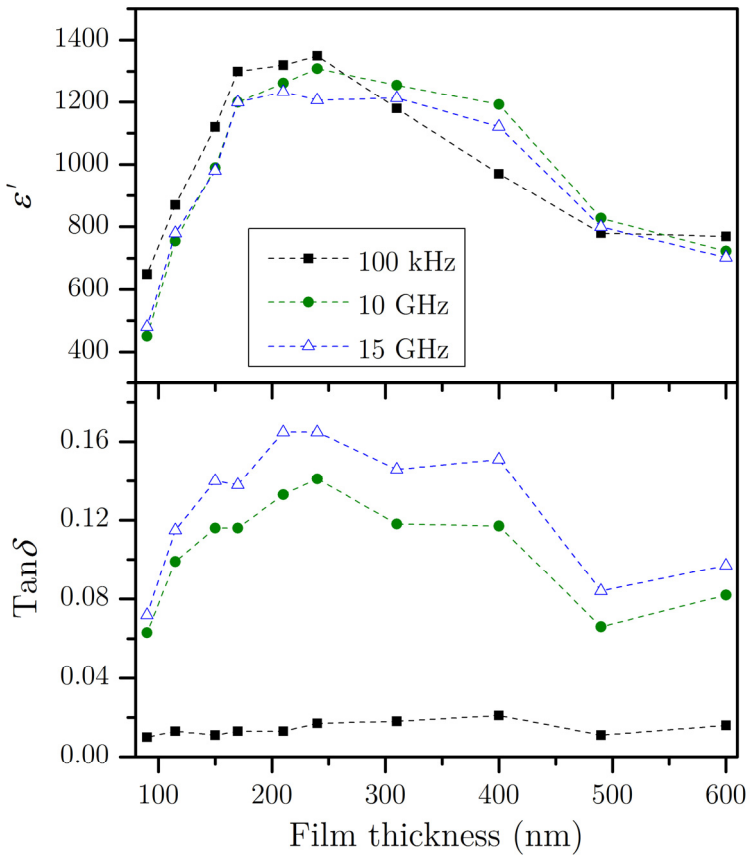


Figure 4.7: The dielectric permittivity ε`and dielectric losses $Tan\delta$ of the BST 50/50 thin films with the thicknesses between 90 nm and 600 nm, measured at 100 kHz, 10 GHz, 15 GHz and at room temperature. Lines between the experimental points are guides to the eyes only.

of permittivity increase is similar to the one observed in BST 30/70 thin films on alumina substrates, i.e., a grain-size increase from 40 nm to 80 nm results in a doubling of the dielectric permittivity, meaning that the grain size clearly controls the dependence of the dielectric permittivity [53]. The relationship between the dielectric permittivity- and the grain size is known as the grain-size effect [63], [64] as explained in the Introduction, Section 1.2.2.2. The residual tensile stress in this thickness range is the highest, between 344 MPa and 378 MPa for the 90-nm- and 170-nm-thick films, respectively.

As the thickness and grain size increase from 170 nm to 240 nm and from 75 nm to 90 nm, respectively, only a slight change in the permittivity is observed (Figure 4.7 and Figure 4.8), which indicates a deviation from the previously observed grain-size effect. Note that a strong decrease of the residual stress is observed in the same thickness range.

A further increase of the thickness from 240 nm to 600 nm is accompanied by a stagnation of the grain size, a drop of the permittivity and reduced values of the residual tensile stress in the films. As explained above the stress relaxation occurred in our BST 50/50 films with thicknesses around or above 240 nm via the formation of intergranular cracks. A drop of the permittivity in thicker films is therefore connected to the formation of cracks, which behave as an additional low-permittivity phase. It was shown that a volume fraction of even less than 1 % of the intergranular cracks in $PbZrO_3$ ceramics strongly reduced the permittivity [69]. Such a decrease of the permittivity can be explained by the brick-wall model, where pores, filled with air, represent the low-permittivity material, while the interior of the grains represents the real permittivity of the BST 50/50 film [69], [88]. Based on the stress decrease we can reasonably assume that nano-cracks are present in the films with thicknesses between 170 nm and 240 nm, where a plateau of the permittivity is observed.

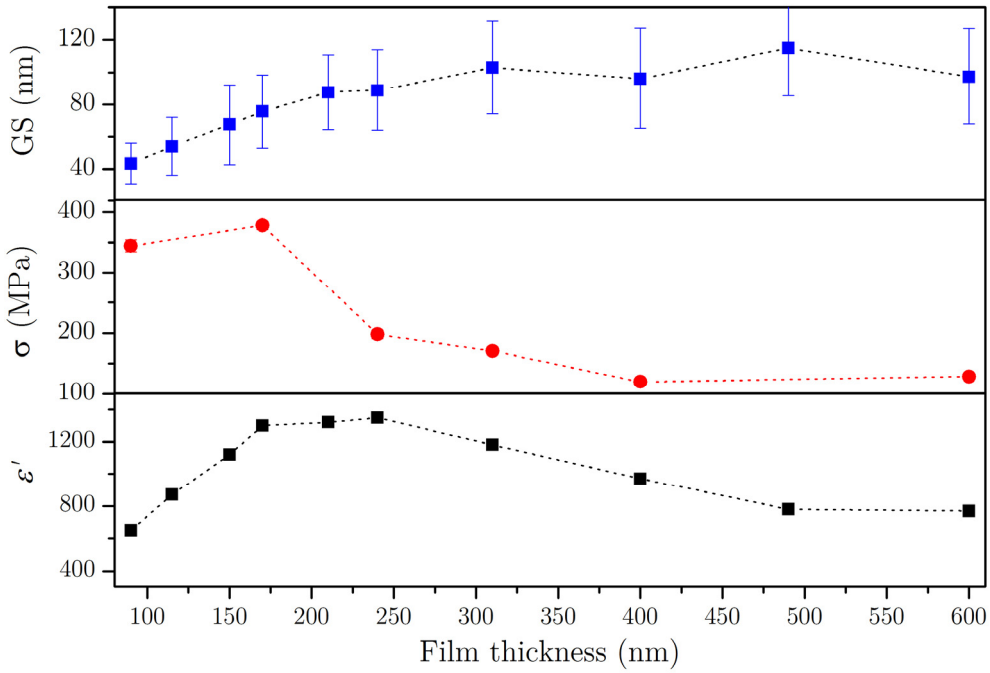


Figure 4.8: The average lateral grain size GS, residual stress σ and the kHz-range dielectric permittivity ε`, extracted from Figure 4.7, plotted against the film thickness. Lines between the experimental points are guides to the eye only. Note that the error bar for the residual stress is in the range of the symbol size.

In Figure 4.9 the temperature dependence of the 5-kHz dielectric permittivity of selected BST 50/50 films with different thicknesses is shown. A broad permittivity maximum between ~300 K and 150 K is present in the 90-nm-thick film (see Figure 4.9 a)). The maximum becomes more pronounced with an increasing film thickness. The temperature of the permittivity maximum decreases from 277 K for the 170-nm-thick film to 250 K for the 600-nm-thick film (Figure 4.9 b)). Note that the peak permittivity reported for the BST 50/50 ceramics is at 240 K [89].

In Figure 4.10 the temperature-dependent dielectric permittivity of the 90-nm- and 600-nm-thick films measured in the frequency range from 100 Hz to 500 kHz is shown. A small dispersion in which the permittivity decreases with increasing frequency is observed at ~375 K in the case of the thinnest film, indicating a long-range movement of the charged species in the material. The dispersion becomes even more pronounced in the 600-nm-thick film.

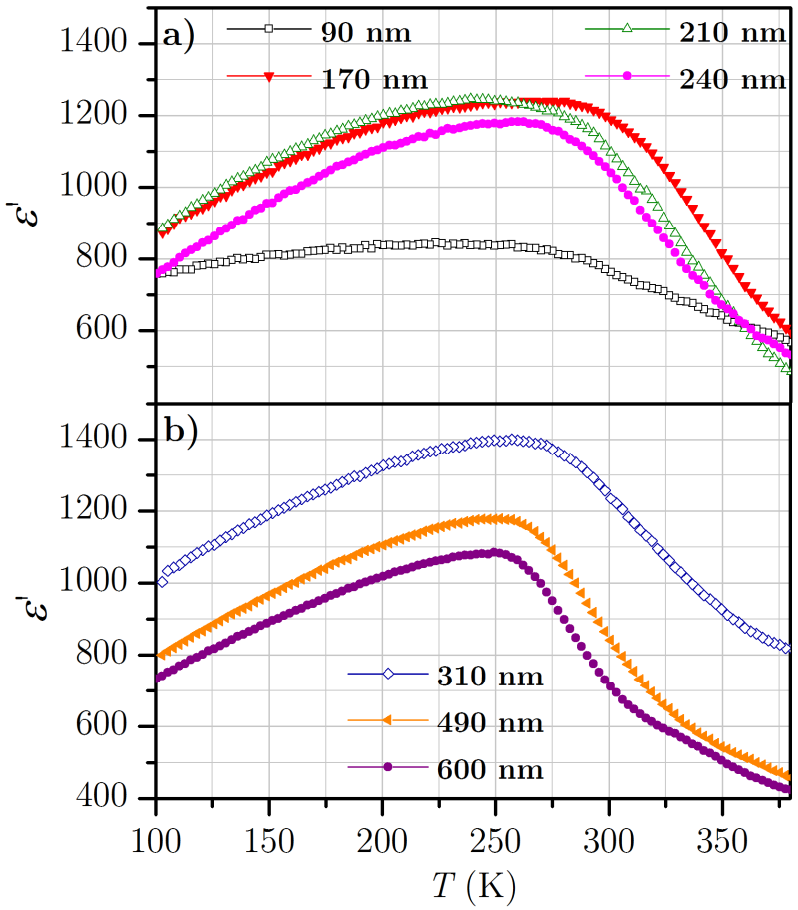


Figure 4.9: Temperature dependence of the dielectric permittivity of the BST 50/50 films with thicknesses in the range from a) 90 nm to 240 nm and b) from 310 nm to 600 nm, measured at 5 kHz.

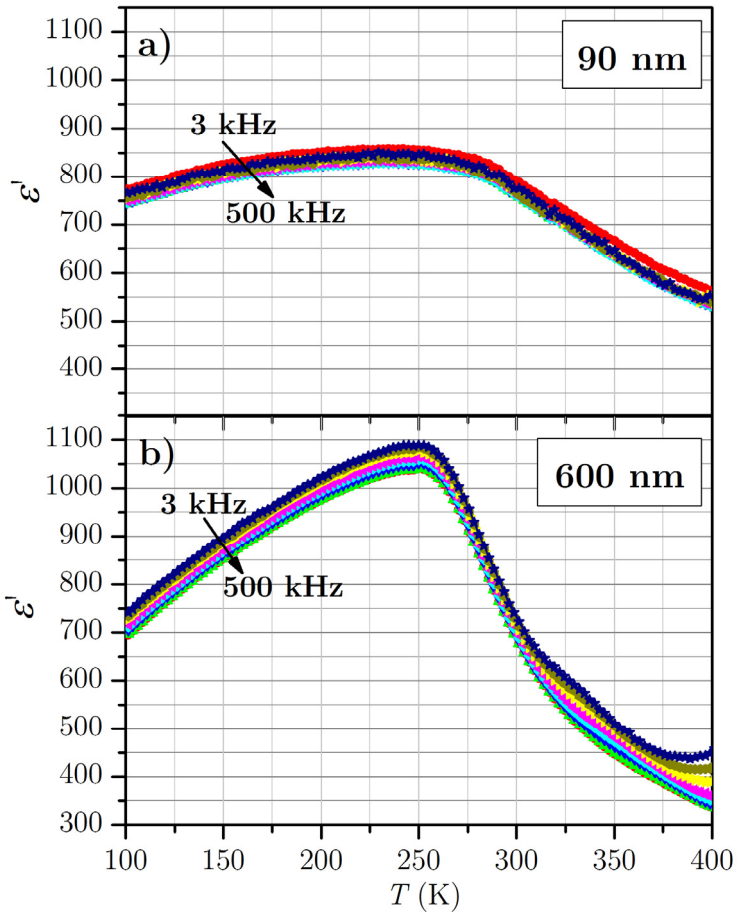


Figure 4.10: Temperature dependence of the dielectric permittivity of the a) 90-nm-thick and b) 600-nm-thick BST 50/50 films measured in the frequency range from 3 kHz to 500 kHz.

The temperature dependence of the dielectric permittivity of selected BST 50/50 films with thicknesses between 90 nm and 310 nm, measured at 15 GHz, is shown in Figure 4.11 a). A similar behavior is observed as in the kHz-range, but with slightly smaller absolute values. The room-temperature permittivity value of the 90-nm-thick film is 550, and it reaches 1120 in the 310-nm-thick film. The temperature of the permittivity maximum of the 150-nm-thick film is 298 K, and it shifts to 282 K in the 310-nm-thick film. The dielectric losses of these films (Figure 4.11 b)) increase with decreasing temperature; however, no maximum is observed. The room-temperature losses are the lowest in the 310-nm- and 90-nm-thick films, with the value of 0.05, and an increase to approximately 0.08 in the 150-nm- and 240-nm-thick films.

Shifting of the position of the permittivity maximum observed in the kHz- and GHz-ranges to lower values with increasing thickness is clearly observed, and it bears a strong resemblance to the decrease of the residual thermal stress (see Figure 4.8). A strong dependence of the Curie point on biaxial strain has been predicted by a phenomenological theory for (100) epitaxial monodomain $BaTiO_3$ films and also experimentally observed in the polycrystalline films of the same material [90], [91]. A broad permittivity maximum can be related to the strain gradients within the films and/or to the small grain size. The consequences of the latter are the increased fraction of the low-permittivity grain boundaries [64] as well as shifting of the low-temperature tetragonal-orthorhombic phase

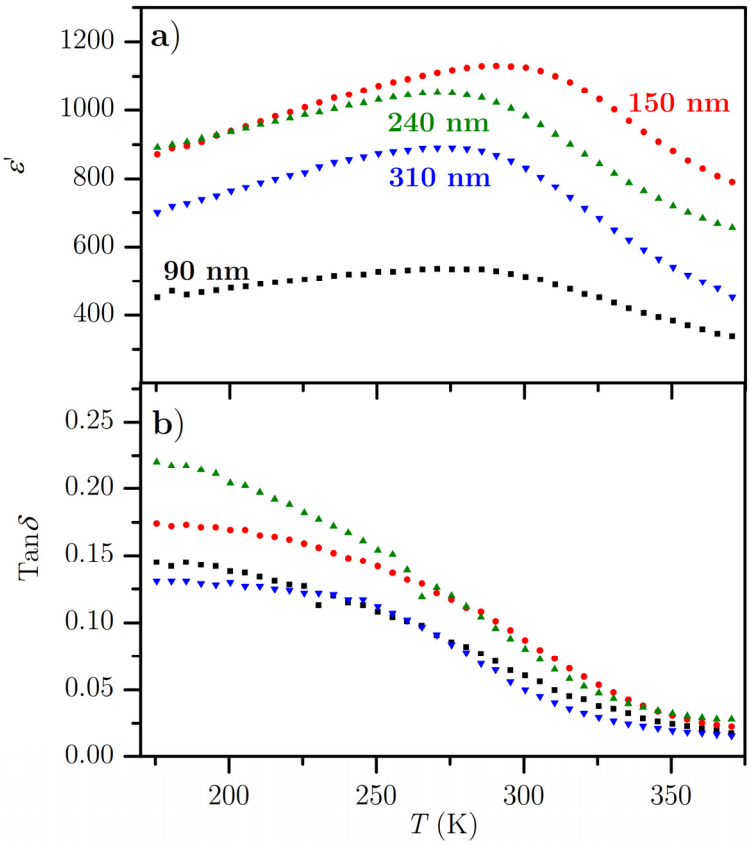


Figure 4.11: Temperature dependence of the a) dielectric permittivity and b) dielectric losses of the 90-, 150-, 240- and 310-nm-thick BST 50/50 films, all measured at 15 GHz.

transition to higher temperatures, which can appear rather close to the cubic-tetragonal transition [63].

The dielectric permittivity of the studied BST 50/50 films in the thickness range between 170 nm and 240 nm is high, above 1200, at all frequencies. The peak value of 1350 (100 kHz) was measured in the 240-nm-thick film with a grain size of ~90 nm. This value is higher than the values reported for BST films with a similar composition and grain size, regardless of the deposition method and the electrode configuration. The reported room-temperature permittivity of ~300-nm-thick sputtered BST 50/50 films with metal-insulator-metal geometry is 760 at 100 kHz. The films were prepared at 600 °C on platinized silicon substrates and had 82-nm grains [40]. The permittivity of PLD-deposited 200-nm-thick $Ba_{0.6}Sr_{0.4}TiO_3$ films with planar capacitor electrodes is 830 at 10 GHz for the films with the 50–100-nm grains prepared on r-sapphire and annealed at 700 °C [48].

In terms of the absolute kHz-permittivity value of the BST 50/50 films it is interesting to compare the present values to the data set created by Aygün et al. [56], who divided the $BaTiO_3$, $SrTiO_3$, BST, $BaTi_xHf_{1-x}O_3$ (x=0-25) and $BaTi_{1-x}Zr_xO_3$ (x=0-25) films and ceramics into three groups, based on their grain size and the permittivity values 100 K below the permittivity maximum (see Figure 4.12). Each group shows a similar trend of increasing permittivity with increasing grain size but at different absolute values of the permittivity as a function of the annealing temperature. In the first group the data correspond to the films processed at temperatures lower than 750 °C. In the second group the films were processed at temperatures higher than 900 °C and the final density of the materials is ~90 %. In the third group the studied materials were also annealed at

temperatures higher than 900 °C, but are almost fully dense. The results show a clear permittivity-grain size relation for each group, which can be explained by the brick-wall model that was used for bulk ceramics by Frey et al. [63].

By comparing the BST 50/50 films obtained in this investigation with the study by Aygün et al. [56], we find that the thinnest film, i.e., the 90-nm-thick film, with a grain size of approximately 45 nm and the permittivity value of 820 at ~150 K and 5 kHz (inset of Figure 4.12), can be placed near the group of films which are characterized by the highest permittivity values and are comparable to the bulk ceramics with similar grain sizes. The films with the thicknesses between 170 nm and 600 nm with the permittivity values between 900 and 1100 (~150 K and 5 kHz) and grain sizes between 80 nm and 105 nm, respectively, are placed into the second group of the results.

In agreement with the study by Aygün et al. [56] we ascribe the good dielectric properties of the thinnest film to the optimized processing conditions, i.e., the separation of the drying/pyrolysis/annealing steps for the efficient removal of the organics, the high heating rate and the annealing temperature of 900 °C, which resulted in a dense and predominately columnar microstructure. As the thickness of the BST 50/50 films increases above 310 nm the data points shift slightly towards the bottom boundary between the second and first group, meaning that the dielectric permittivity of the films is decreasing at similar values of the grain size. We explain this shift with the presence of cracks, which are an additional factor that is strongly influencing the dielectric properties of the films.

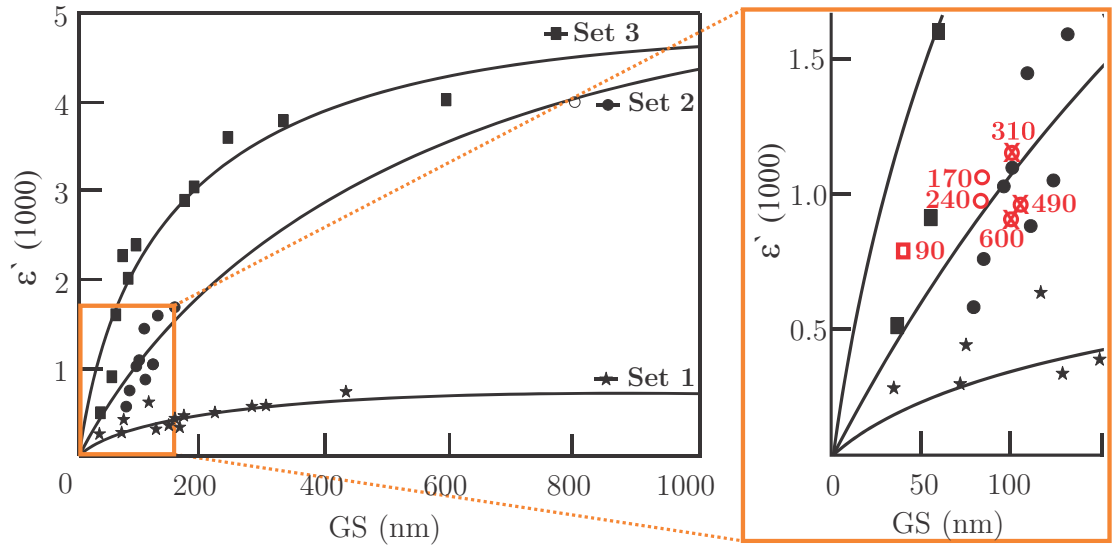


Figure 4.12: The grain size dependence of the dielectric permittivity of $BaTiO_3$ films from the work of Aygün et al. [56] compared to the data from the literature for various $BaTiO_3$, $SrTiO_3$, BST, $BaTi_xHf_{1-x}O_3$ (x=0-25) and $BaTi_{1-x}Zr_xO_3$ (x=0-25) ceramics and thin films. The permittivity was measured 100 °C below the Curie point for each sample. The data is divided into three sets according to the annealing temperature and the final density of the films and ceramics. Set 1: $T_{anneal} < 750$ °C, Set 2: $T_{anneal} > 900$ °C, ~90% density, and Set 3: $T_{anneal} > 900$ °C, full density of the investigated films and ceramics. A narrower range of the grain sizes is enlarged on the right. The results for our BST 50/50 films are included in the inset and the numbers next to the symbols denote the thicknesses of the films measured in nm.

The permittivity-voltage curves measured in the +40 V to -40 V range and 100 kHz for selected BST 50/50 films are shown in Figure 4.13. In Table 4.2 the tunability n, calculated as the ratio of the permittivity at 0 V and 40 V and the relative tunability n_r (see Eq. (1.10)), are collected for all the films. The 90-nm-thick film shows a low DC-voltage dependence and its tunability is 2.22, and with increasing thickness, n steeply increases. The highest value of almost 4.0 is obtained for the 170-nm-thick film. With a further thickness increase the tunability decreases and for the 240-nm-thick film it is 3.33, and it further drops to 1.87 for the thickest, i.e., 600-nm-thick film.

In all the films the voltage dependences are symmetrical, although a slight hysteresis, which is more evident in the films with a higher thickness, can be observed. A slight hysteresis was also observed in various solution-derived BST thin films with compositions in the paraelectric phase at room temperature [44], [57], [92], [93]. The origin of the hysteresis observed in the films with a high dielectric permittivity is not completely explained, but could be related to the presence of nano-polar regions [94] or to the presence of oxygen vacancies and the space charges at the interface between the film and the substrate and/or at the grain boundaries [92], [93].

The high dielectric permittivity of the BST 50/50 films obtained with the improved microstructure, i.e., high density and predominantly columnar grains, leads to an enhanced voltage tunability, consistent with the literature [38]. The tunability of the BST 50/50 films is high, especially in the thickness range between 115 nm and 170 nm, compared to the values for the solution-derived BST 50/50 films taken from the literature. For example, the relative room-temperature tunability of the 240-nm-thick BST 50/50 film obtained in this investigation was 70 % at 133 kV/cm. Levasseur et al. [57] prepared 280-nm-thick BST 50/50 film by CSD and annealing at 800 °C. The films have a comparable grain size, i.e., approximately 100 nm, but a higher level of porosity. The dielectric permittivity measured at 10 kHz and at room temperature was 280 and the tunability calculated at a similar applied electric field, i.e., 150 kV/cm, was 40 %. Dawley et al. [52] prepared polycrystalline BST 50/50 thin film on Ni foils by CSD at 900 °C. The dielectric permittivity of the film was 365, measured at 10 kHz and room-temperature. The tunability of the film was 44 %, measured with the applied electric field of 250 kV/cm. Note that in both cases the dielectric permittivity of the films was almost four times lower than for our films, which also resulted in lower values of the tunability.

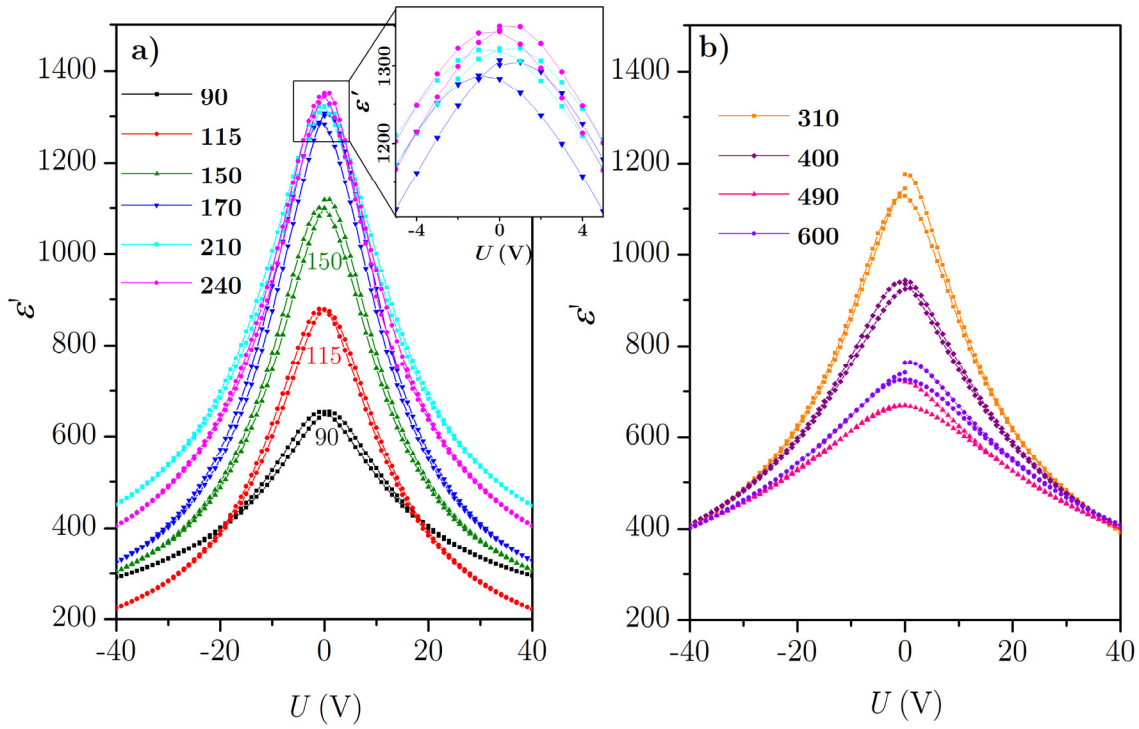


Figure 4.13: Permittivity-voltage curves measured in the +40 V to -40 V range at 100 kHz for the a) 90-, 115-, 150-, 170-, 210-, 240-nm-thick films and for the b) 310-, 400-, 490- and 600-nm-thick films. Note that the numbers on the graphs denote the thicknesses of the films measured in nm.

Table 4.2: The tunability n, expressed as the ratio of the permittivities at 0 V and 40 V, and the relative tunability n_r of the BST 50/50 films with different film thickness, measured at 100 kHz and room temperature.

Film thickness (nm)	n	n_r (%)
90	2.22	55
115	3.95	75
150	3.65	73
170	3.98	75
210	3.10	68
240	3.33	70
310	2.99	67
400	2.42	59
490	1.90	47
600	1.87	46

4.2 Crystallization and Evolution of the Microstructure of $Ba_{0.5}Sr_{0.5}TiO_3$ Thin Films

This sub-chapter is divided into two parts. In the first part the BST 50/50 films prepared by the multi-step annealing process are studied. The crystallization and the evolution of the microstructure of the films consisting of seven deposited layers are investigated upon annealing at temperatures between 600 °C and 900 °C. The microstructures of the BST 50/50 films are then included in the structural zone model for solution-derived thin films.

In the second part, the evolution of a columnar microstructure in the BST 50/50 films prepared by the multi-step annealing process at 900 °C is discussed.

4.2.1 $Ba_{0.5}Sr_{0.5}TiO_3$ Thin Films Prepared at Temperatures between 600 °C and 900 °C

The XRD patterns of the BST 50/50 films prepared by multi-step annealing of seven deposited layers at temperatures between 600 °C and 900 °C are presented in Figure 4.14. In the case of the film annealed at 600 °C we observe a sharp peak at 2θ =28 °, which corresponds to the substrate and a broad peak between 2θ =27 ° and 28 °. The latter could correspond to the intermediate phase identified as the nano-crystalline, alkaline-earth titanium oxo-carbonate phase, which has been reported to form in the case when short-chain carboxylates such as acetates are used for the synthesis of BST precursor solutions [17], [50], [51], [58]. According to the literature the intermediate phase forms at approximately 450 °C and is stable up to 600 °C or 650 °C in the case of $SrTiO_3$ and $BaTiO_3$, respectively.

As the annealing temperature increases to 640 °C and 680 °C the peak attributed to the intermediate phase disappears and the peaks at approximately 2θ =22.5 °, 32.0 °, 39.5 ° and 45.9 ° appear. According to the JCPDS database [79] these peaks belong to the BST 50/50 perovskite phase with the pseudo-cubic unit cell. This result indicates that the crystallization of BST 50/50 thin films into the pure perovskite phase occurs at or slightly below 640 °C. The reported temperature agrees well with the literature, where the crystallization temperature for perovskite $BaTiO_3$ and $SrTiO_3$ films, prepared from the alkaline earth acetates and Ti-n-butoxide, was reported to be between 650 °C and 700 °C [50], [58].

With an increasing annealing temperature from 640 °C to 900 °C the relative intensity of the perovskite peaks gradually increases and their full width at half maximum (FWHM) decreases, indicating an improved crystallinity. The crystallite sizes were calculated using the Scherrer equation (see Eq. (3.1)) for the diffraction peak of the (110) crystal planes. The crystallite size of the BST 50/50 film annealed at 640 °C is 18 nm, and this increases slightly to 25 nm for the film annealed at 800 °C, see Table 4.3. As the annealing temperature further increases to 900 °C the crystallite size increases to 63 nm. The values of the Lotgering factor are approximately 0.4 for the majority of the films, with the exception of the films annealed at 800 °C (0.06) and 900 °C (0.14), as shown in Table 4.3.

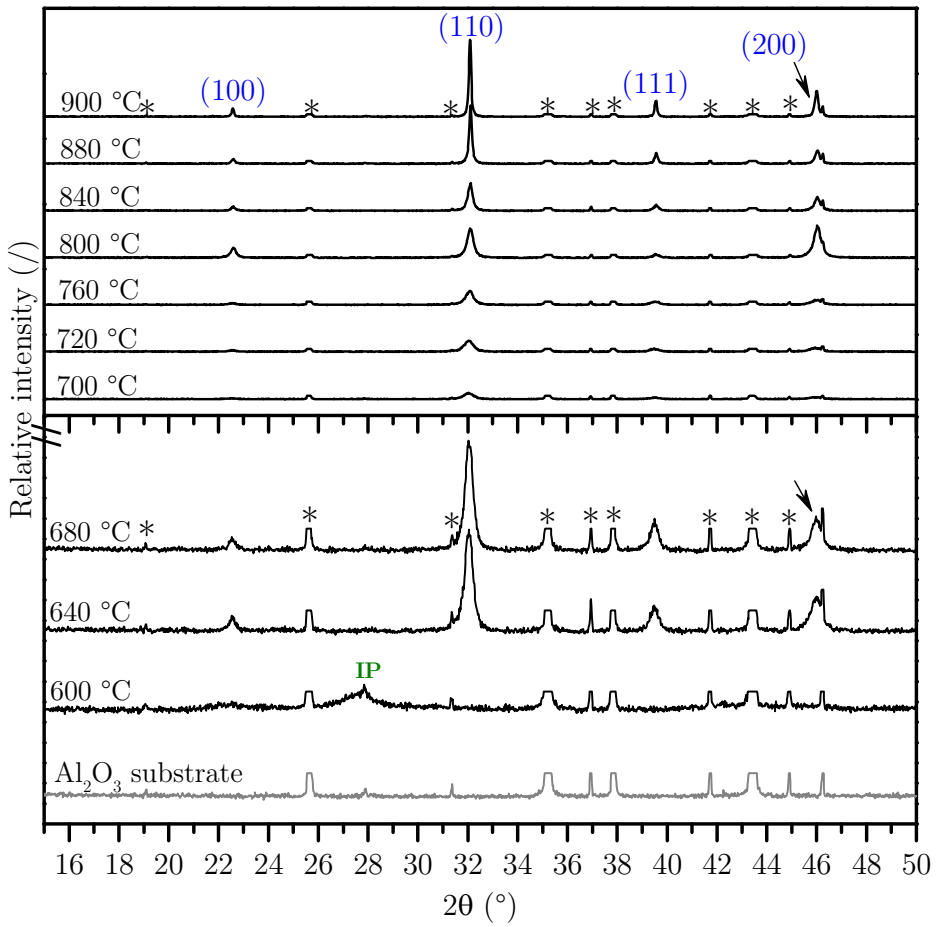


Figure 4.14: XRD patterns of the BST 50/50 films on alumina substrates annealed at temperatures between 600 °C and 900 °C. The peaks corresponding to the perovskite phase are denoted with the Miller indices [79]. The pattern of the alumina substrate is also shown as a reference. Note the change of the scale. * - subtracted peaks of the alumina substrate. IP – intermediate phase.

Table 4.3: The crystallite size and Lotgering factor $f_{(110)}$ of the BST 50/50 films annealed at temperatures between 640 °C and 900 °C.

T_{anneal} *(°C)*	*Crystallite size (nm)*	$f_{(110)}$
640	18	0.36
680	18	0.40
700	20	0.35
720	20	0.36
760	21	0.38
800	25	0.06
840	32	0.30
880	55	0.37
900	63	0.14

The FE-SEM cross-section micrographs of the representative BST 50/50 films annealed at temperatures between 600 °C and 800 °C are shown in Figure 4.15. The film annealed at 600 °C is 310 nm thick. No grains could be observed in the cross-section micrograph, confirming the predominantly amorphous phase composition, in agreement with the XRD analysis, shown in Figure 4.14. As the annealing temperature increases to 640 °C the FE-SEM analysis reveals that the BST 50/50 film is 300 nm thick and consists of grains that are approximately 10-20 nm large. With a further increase of the temperature from 680 °C to 720 °C the film thickness decreases from 300 nm to 260 nm. The grain size is between 20 nm and 30 nm for both films. We note that the average grain sizes of the BST 50/50 films annealed at temperatures lower than 800 °C were determined from the cross-section micrographs by the linear-intercept method, since the resolution of the surface microstructures was too low. But for the films annealed at temperatures above 800 °C, the average grain size was determined from the surface micrographs.

The granular microstructure also persists in the films annealed at 720 °C and 760 °C, as is clearly observed in Figure 4.15 d) and e). The films are 260 nm thick with grains that are approximately 30 nm in size. Some porosity concentrated at the interfaces between the individual layers is observed in the cross-section micrograph in Figure 4.15 e), in agreement with the observation of Gust et al. [51]. As the annealing temperature increases further to 800 °C the thickness of the film remains at 260 nm with equiaxed grains that are approximately 30 nm across, see Figure 4.15 f).

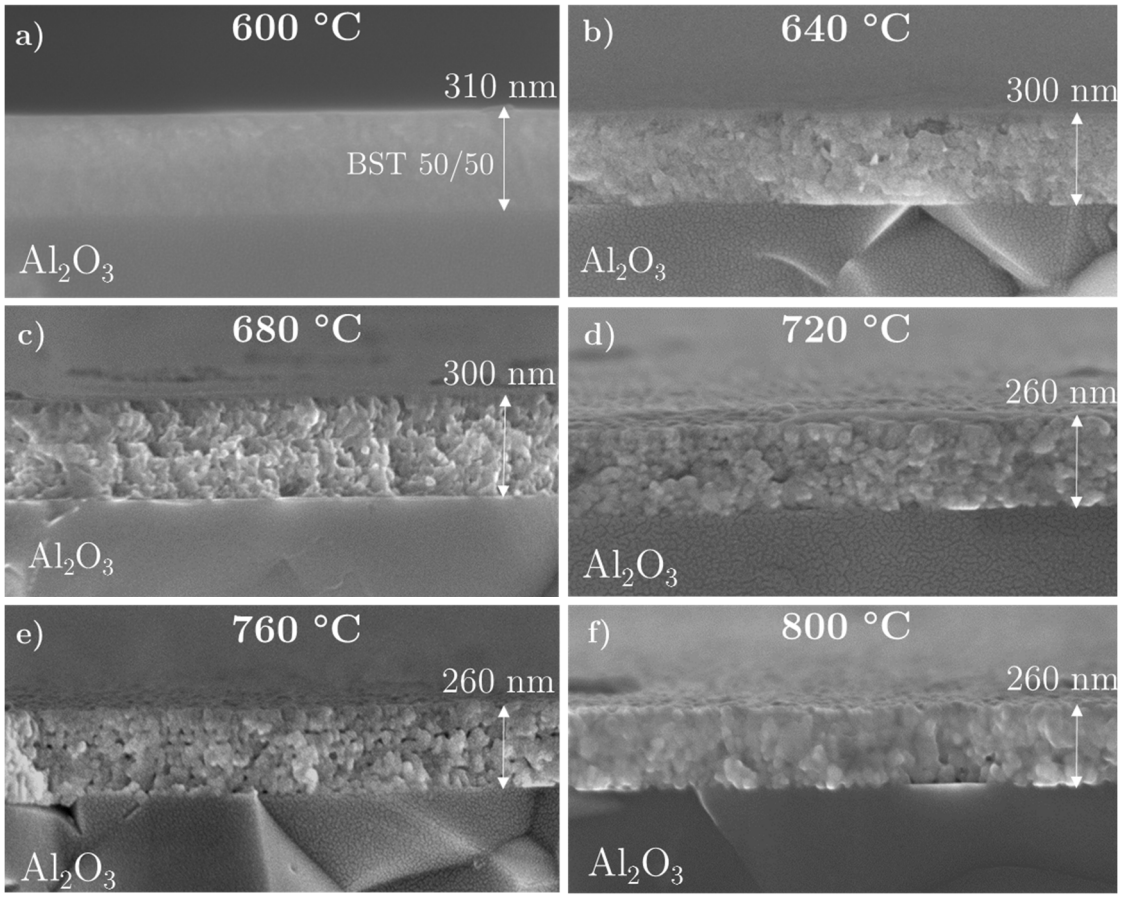


Figure 4.15: FE-SEM cross-section micrographs of the BST 50/50 films on alumina substrates annealed at a) 600 °C, b) 640 °C, c) 680 °C, d) 720 °C, e) 760 °C and f) 800 °C. The arrows denote the thicknesses of the films.

The TEM analysis of the cross-section microstructure of the BST 50/50 films annealed at 700 °C and 800 °C are presented in Figure 4.16. The microstructure of the BST 50/50 film annealed at 700 °C is uniform and consists of equiaxed grains that are approximately 10–20 nm large. Many grains are observed within one deposited layer. The film contains intergranular pores with a size close to the grain size, see the bright areas in Figure 4.16 a). The interface between the film and the alumina substrate, shown in Figure 4.16 b), and the grain boundaries, shown in Figure 4.16 c), are clean without any secondary phase. The same is also observed for the BST 50/50 film annealed at 800 °C, see Figure 4.16 e) and f).

The TEM analysis of the BST 50/50 film annealed at 800 °C shows that the film consists predominantly of equiaxed grains with sizes of ~30 nm, which is approximately in the range of thickness as a single deposited layer, see Figure 4.16 d).

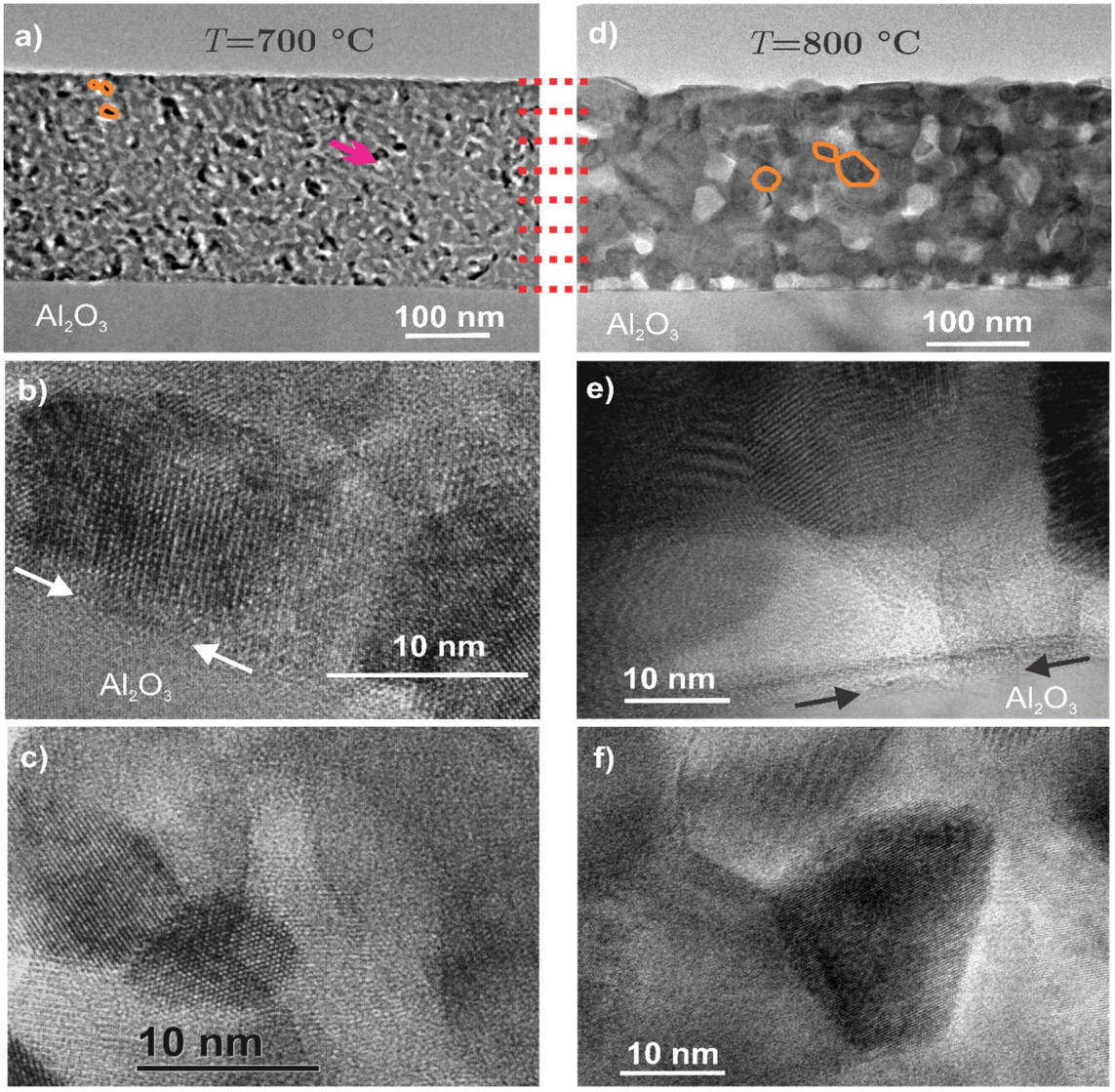


Figure 4.16: a) and d) bright-field TEM cross-section micrographs of the BST 50/50 films on alumina substrates annealed at 700 °C and 800 °C. The grains are encircled with full lines, the dotted lines mark the thickness of individual deposited layers and the arrow marks the pore in the film. TEM micrographs in b) and e) represent the interface between the film and alumina substrate (marked with arrows) and c) and f) show the grains and grain boundaries in the film at higher magnifications.

In Figure 4.17 the FE-SEM cross-section and corresponding surface micrographs of the BST 50/50 films annealed at 840 °C, 880 °C and 900 °C are presented. All the BST 50/50 films are approximately 250 nm thick. In the cross-section micrograph of the film annealed at 840 °C predominantly equiaxed grains that extend across one deposited layer are observed and some grains that extend across more than one layer could also be found. The average lateral grain size is approximately 40 nm and the pores that are approximately 10-20-nm large are observed in the surface micrograph, see Figure 4.17 b). As the annealing temperature increases to 880 °C some grains that extend from the bottom to the top of the film are observed in the cross-section microstructure in Figure 4.17 c). The columnar microstructure dominates as the annealing temperature further increases to 900 °C, as shown in Figure 4.17 e). The surface microstructures of the films annealed at 880 °C and 900 °C are dense and homogeneous with an average lateral grain size of approximately 90 nm. The origin of the formation of the columnar microstructure of the BST 50/50 films prepared by the multi-step annealing process at 900 °C is investigated and discussed in the next sub-chapter.

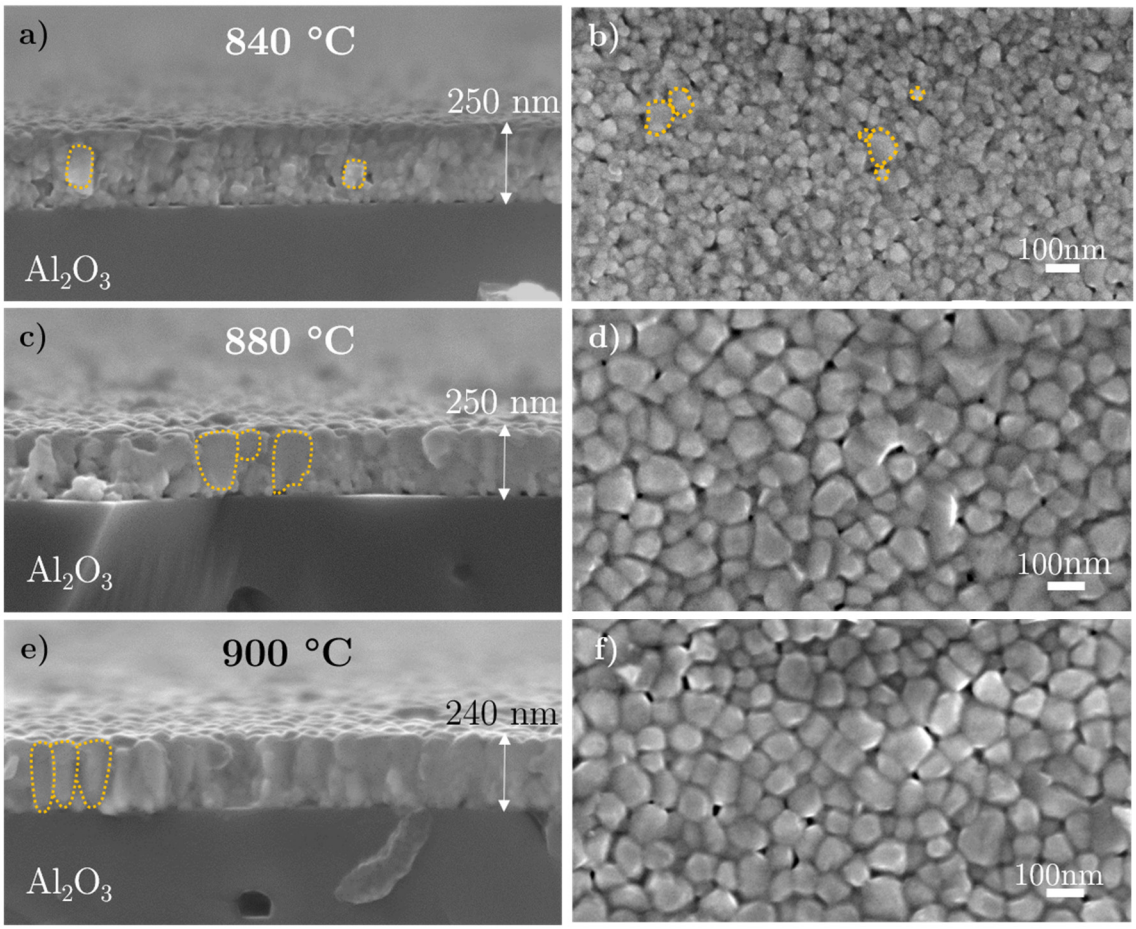


Figure 4.17: FE-SEM cross-section and surface micrographs of the BST 50/50 films on alumina substrates annealed at a), b) 840 °C, c), d) 880 °C and e), f) 900 °C. Arrows and corresponding values in nm denote the thickness of the films. Selected grains are encircled with dotted lines.

The film thicknesses and the average lateral grain sizes of the BST 50/50 films are plotted as a function of the annealing temperature in Figure 4.18. The thickness of the film annealed at 640 °C is approximately 300 nm, and as the annealing temperature increases above 720 °C a steep drop of the thickness to 260 nm is observed, indicating the densification of the films. With a further increase of the annealing temperature to 900 °C, the thickness only slightly decreases to 240 nm.

The average lateral grain size of the films annealed at between 640 °C and 680 °C is approximately 20 nm and this slightly increases to approximately 30 nm with an increasing annealing temperature to 760 °C. In these cases the microstructures of the films are granular with equiaxed grains smaller than the thickness of an individual deposited layer. A similar granular microstructure with grain sizes of a few tens of nm has been commonly observed in the case of solution-derived $BaTiO_3$, $SrTiO_3$ and BST thin films prepared by one-step or two-step annealing [17], [50], [53] and a few examples of the microstructures taken from the literature are shown in the Introduction, see Figure 1.15.

In the films annealed at 800 °C the lateral grain size is quite similar to the thickness of an individual layer. Upon annealing at 880 °C and 900 °C we observe a steep increase of the lateral grain size, reaching 80-90 nm, concurrent with the evolution of the predominantly columnar microstructure.

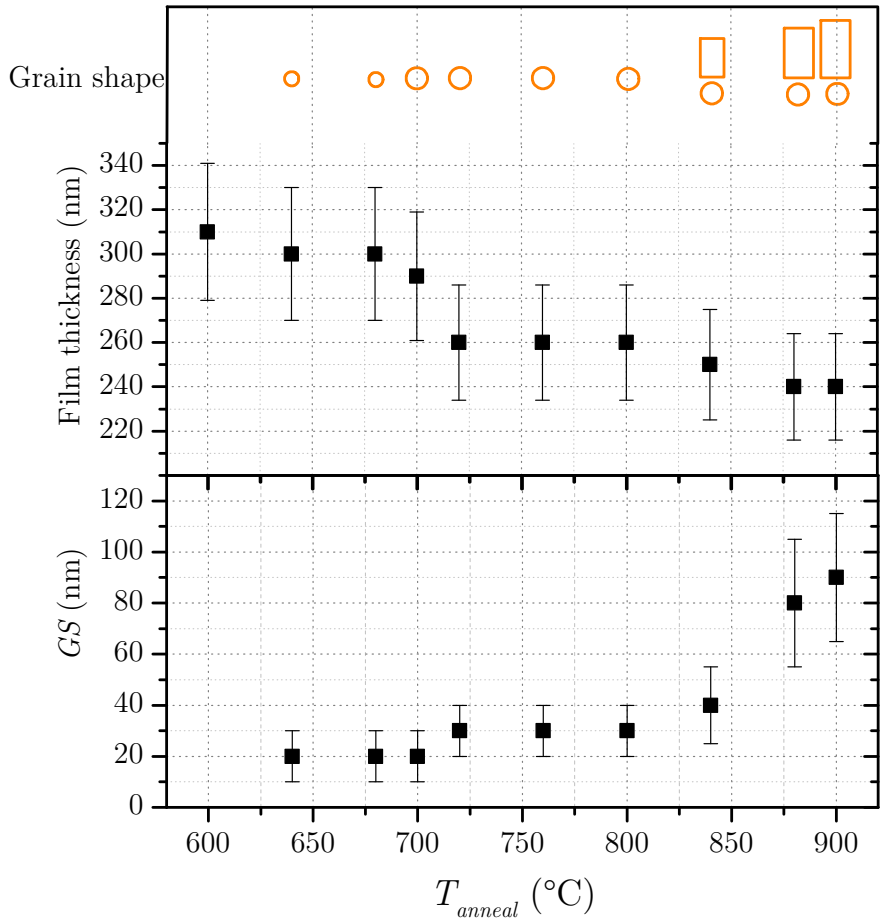


Figure 4.18: The film thickness and average grain size GS of the BST 50/50 films plotted as a function of the annealing temperature (T_{anneal}). The shape of the grains is added at the top of the graph. Circles represent equiaxed grains and rectangles represent columnar grains.

The observed changes in the average grain size and shape of the BST 50/50 films with increasing annealing temperature are attributed to the temperature-dependent nucleation and growth rates (see Introduction, Figure 1.8). In the case of the films annealed at lower temperatures, i.e., below 800 °C, a high nucleation rate and low grain growth rate result in the formation of many nuclei that grow until they impinge into each other. In these cases many equiaxed grains are formed within an individual deposited layer. In the case of the films annealed at higher temperatures, i.e., at/above 800 °C, a low nucleation rate results in the formation of fewer nuclei compared to the films annealed at lower temperatures. The nuclei grow with a higher rate and extend through one or multiple deposited layers, or even through all the layers, and form the predominantly columnar microstructure of the BST 50/50 films. These results are consistent with observations by Hoffmann et al. [50], who was the first to report the columnar microstructure of $BaTiO_3$, $SrTiO_3$ and BST thin films on platinized silicon substrates, obtained by the repeated deposition and annealing of very thin layers (multi-step). The authors explained that when the films were prepared from only 10-nm-thick deposited layers at 750 °C one grain extended through an individual layer. After the deposition and annealing of multiple layers the grains extended throughout the whole film thickness, forming the columnar microstructure of the films.

The change of the granular to a columnar microstructure with increasing annealing temperature was also observed for the solution-derived BST 70/30 thin films studied by Kageyama et al. [55]. The films prepared at 650 °C by the multi-step annealing process on $Pt(111)/BaTiO_3/Si(100)$ and $Pt(111)/MgO(100)$ substrates were approximately 300 nm thick and had granular microstructures with an average lateral grain size of approximately 20 nm. After annealing at 800 °C the average grain size increased to 100 nm and 150 nm, depending on the substrate. In these cases the grains grew through all the deposited layers and thus formed the columnar microstructure. The reported values of the grain sizes of the granular microstructures of the films studied by Kageyama et al. [55] agree well with our results, as well as the observed change from the granular to the columnar microstructure. However, for our BST 50/50 films a predominantly columnar microstructure is observed at slightly higher temperatures, i.e., at 880°C and 900 °C, which could arise from the differences in the compositions of the films, in the thickness of an individual deposited layer and/or due to different annealing conditions.

In summary, we find that the columnar microstructure is formed when the thickness of an individual layer is approximately 40 nm and when the films are annealed at/above 880 °C. But we wanted to test if the columnar microstructure forms when a film consisting of even thinner individual layers is prepared at a lower annealing temperature, such as at 700 °C. For this reason we prepared a BST film from the coating solution that was diluted from the initial molar concentration of 0.25 M to 0.125 M and by multiple deposition-annealing steps. The cross-section microstructure of such a film is presented in Figure 4.19 a). We found that the film consists of individual layers that are approximately 15 nm thick. Although we distinguished equiaxed grains of a few tens of nm across, we noticed that they are grouped in quite densely packed columns extending through the whole film thickness. The cross-section microstructure of the BST 50/50 film with the granular microstructure is included in Figure 4.19 b). This film was prepared from the 0.25-M solution at 700 °C. Such a comparison provides good evidence of the importance of the individual layer thickness in the development of the columnar microstructure.

In contrast, if the thickness of the layer is greatly increased upon annealing, which is achieved by repeating only the deposition-drying-pyrolysis steps, the resulting microstructure of a BST film is granular, notwithstanding the annealing temperature, as evidenced by the microstructures of the BST 50/50 films prepared by the two-step annealing process at 700 °C and 900 °C, see Figure 4.20.

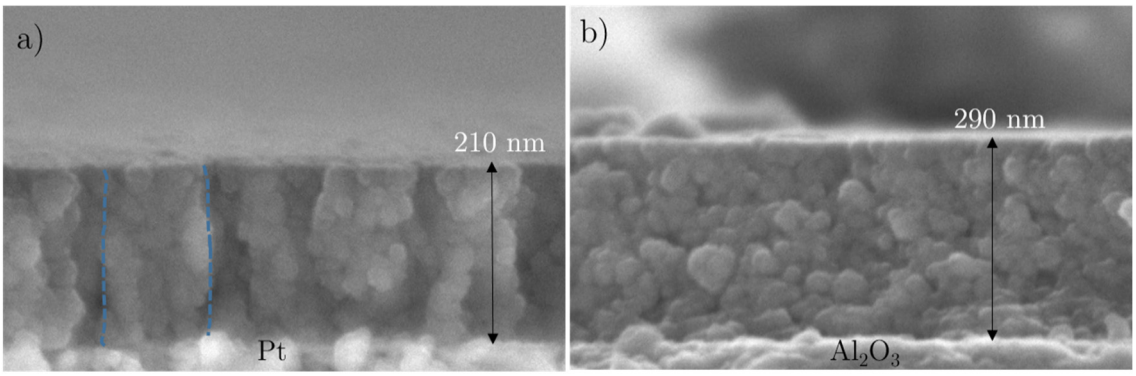


Figure 4.19: a) FE-SEM cross-section micrograph of the BST 30/70 thin film prepared by the multi-step annealing process at 700 °C on a Pt/Si substrate from the 0.125-M coating solution. The lines mark the shape of the columns, consisting of many equiaxed grains. b) FE-SEM cross-section micrograph of the BST 50/50 film prepared by the multi-step annealing process at 700 °C from the 0.25-M solution.

By comparing the microstructures of the BST 50/50 films prepared by the two-step and multi-step annealing process at 900 °C (compare Figure 4.20 b) and Figure 4.17 e)) we observe that the density of the latter is much higher, which is ascribed to the optimized processing conditions [50]. The same was also observed by Aygün et al. [56].

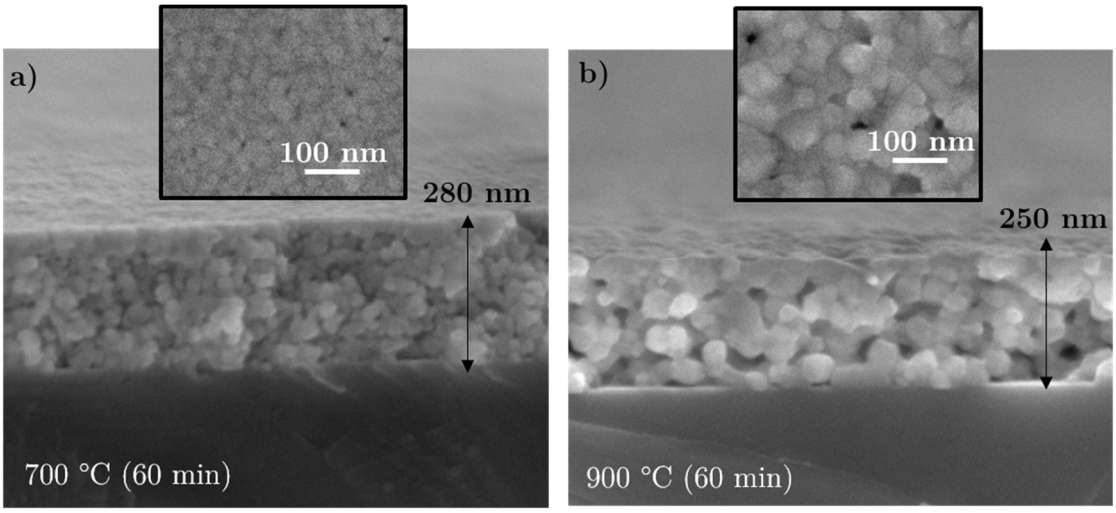


Figure 4.20: The FE-SEM cross-section micrographs of the BST 50/50 films prepared by the two-step annealing process at a) 700 °C and b) 900 °C. The time in the brackets denotes the annealing time of the six deposited layers. Insets show the surface microstructures of the corresponding films.

Schuler et al. [28] introduced the structural-zone model for solution-derived thin films. The model predicts the type of the microstructure according to the intrinsic crystallite size (ICS) or grain size, single-layer thickness (SLT) and the annealing temperature of the films. For selected values of the ICS/SLT ratio the microstructure of the films is granular, layered or columnar, as explained in the Introduction, Section 1.1.5. In analogy with the Schuler model we collected the literature data for different solution-derived $BaTiO_3$, $SrTiO_3$ and BST thin films and plotted them in Figure 1.18. Furthermore, we included the results of our BST 50/50 films in the latter graph to enable a comparison with the literature data, see Figure 4.21 a). We found that:

- The granular microstructure is obtained upon multi-step annealing of BST 50/50 films at temperatures between 640 °C and 720 °C (ICS<SLT). Between 760 °C and 800 °C, the grain size is approximately equal to the layer thickness (ICS≤SLT), the microstructure is predominantly granular, but in some parts we observe that the grains extend through more than one layer (layered microstructure). The ICS≪SLT for the films prepared by the two-step annealing process.
- The layered microstructure is observed in the film annealed at 840 °C, where ICS≅SLT.
- The columnar microstructure is characteristic for the films annealed at/above 880 °C, where ICS>SLT.

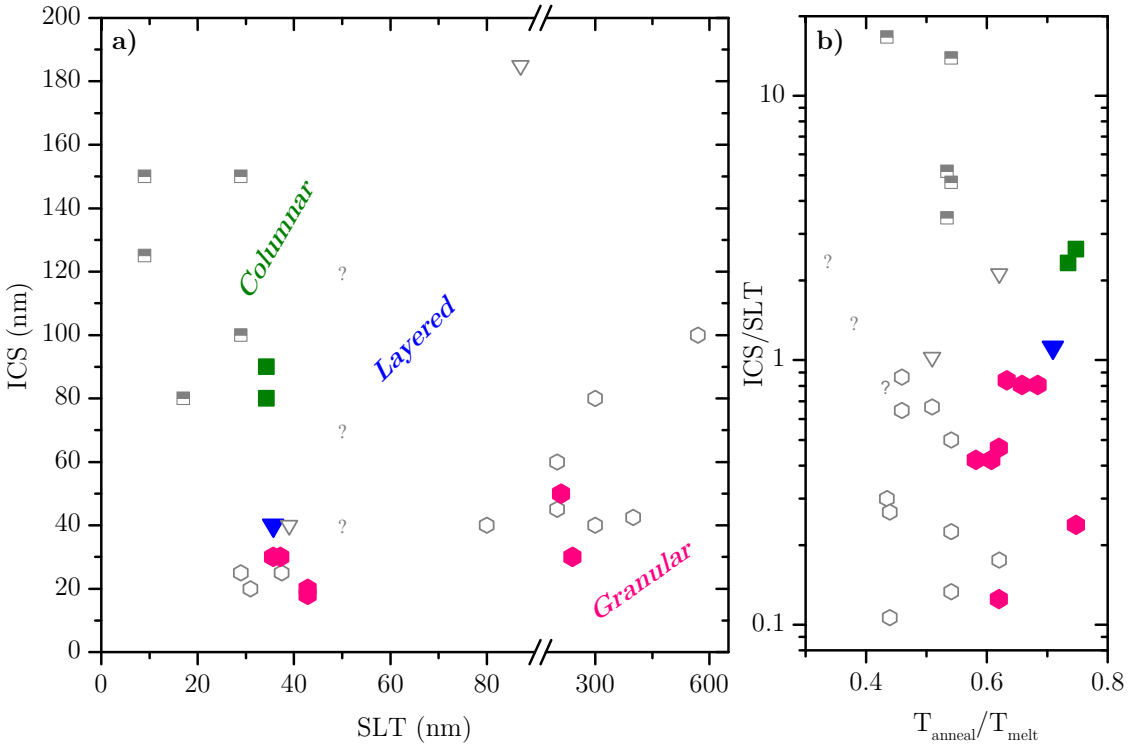


Figure 4.21: The structural-zone model for the solution-derived $BaTiO_3$, $SrTiO_3$ and BST thin films plotted as the intrinsic crystallite size (ICS) versus single-layer thickness (SLT) (open symbols), re-plotted from Figure 1.14. The results for the BST 50/50 thin films prepared by the multi-step and two-step annealing processes within this thesis are included (full symbols). Note that ICS is determined as the average lateral grain size of the films.

In the plot of ICS/SLT versus T_{anneal}/T_M shown in Figure 4.21 b) we distinguish three regions, each corresponding to a certain type of microstructure. The data points belonging to the granular microstructure cover a wide ICS/SLT range, from ~0.1 to ~1. In only one case we obtained a film with a layered microstructure, at ICS/SLT ~1.2. As our films were prepared in 40 °C intervals, we assume that the temperature window for such a microstructure to develop is relatively narrow. However, a precise boundary between the granular and layered microstructures could not be unambiguously determined. We note that under our processing conditions the columnar microstructure is obtained for an ICS/SLT ratio of ~2.5, which is noticeably lower than the literature data points. This difference can be explained by the much higher annealing temperatures used in our study, while the films reported in references [17], [50], [55] were annealed at temperatures not exceeding 800 °C.

4.2.2 Evolution of the Columnar Microstructure of $Ba_{0.5}Sr_{0.5}TiO_3$ Thin Films prepared at 900 °C

The evolution of the columnar microstructure of the BST 50/50 films was systematically studied after each of the seven layers was deposited, dried, pyrolyzed and annealed at 900 °C.

The first BST 50/50 layer was annealed at 900 °C for different times, i.e., 1 min, 5 min, 15 min, 30 min and 60 min, and the films are further denoted as 1L (annealing time). The XRD results obtained for the 1L BST 50/50 films are presented in Figure 4.22 and show that all the films crystallize in the perovskite phase and that a longer annealing time results in improved crystallinity.

The FE-SEM cross-section and surface micrographs of the 1L BST 50/50 films are presented in Figure 4.23. The 1L (1 min) film is ~50 nm thick and consists predominantly of columnar grains that extend through the whole film thickness. On the surface micrograph we observe that the grains are 20-30-nm large and that fine pores are present between the grains. With a longer annealing time, i.e., 5 min, the thickness of the film remains ~50 nm and the average lateral grain size of the 1L (5 min) film is between 30 nm and 40 nm. The porosity and pore size decrease. As the annealing time increases to 15 min and further to 60 min, the time does not have a major effect on the grain size and porosity; the surface microstructures of the 1L (15 min) and 1L (60 min) films are dense and uniform with average lateral grain sizes of 30-40 nm, see Figure 4.23 e)-h).

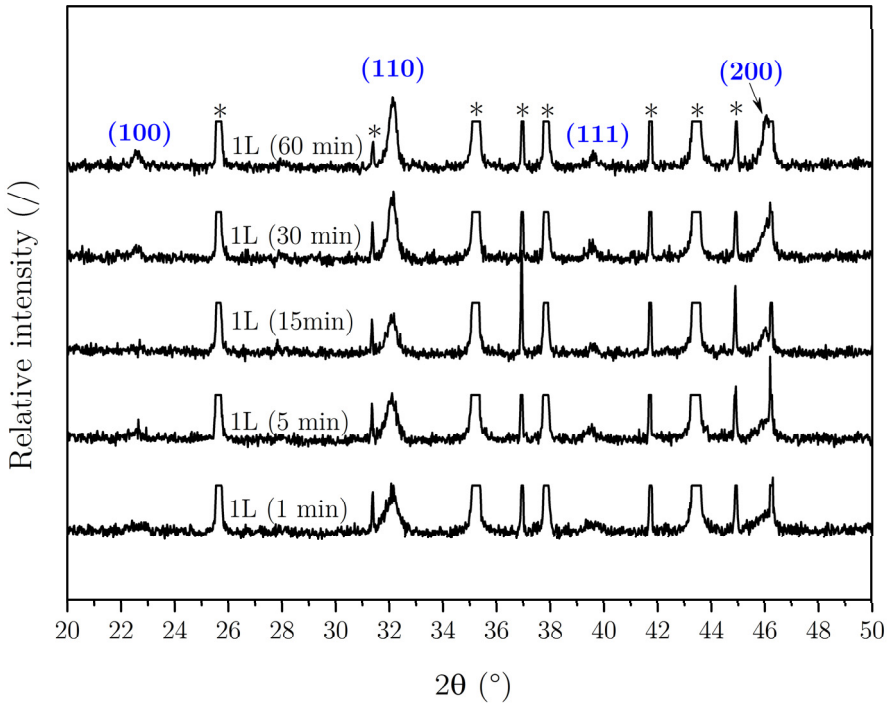


Figure 4.22: XRD patterns of the BST 50/50 1L films on alumina substrates annealed at 900 °C for 1 min to 60 min [95]. The peaks corresponding to the perovskite phase are denoted with the Miller indices [79]. * - subtracted peaks of the alumina substrate.

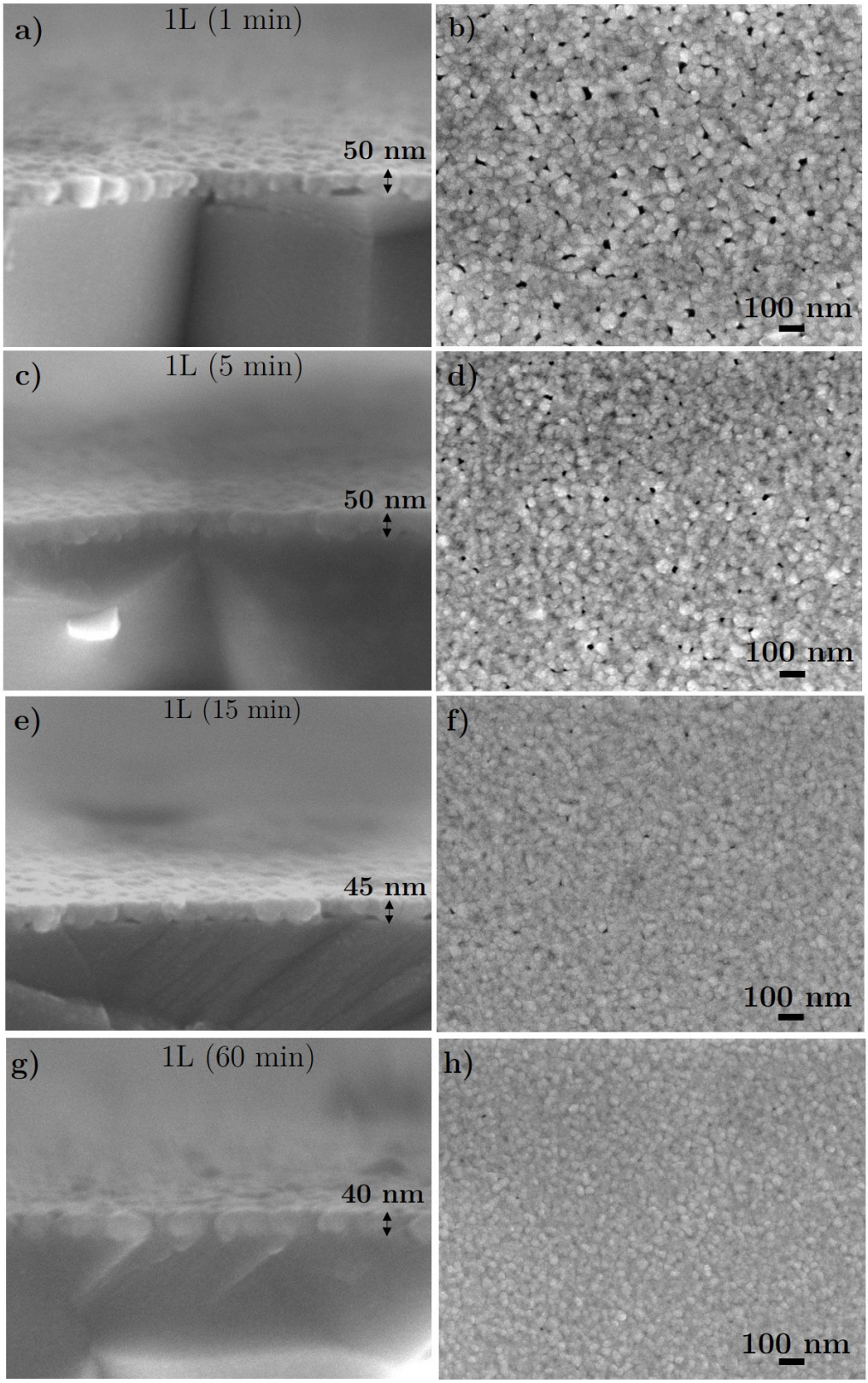


Figure 4.23: FE-SEM cross-section and surface micrographs of the 1L BST 50/50 films annealed at 900 °C for a), b) 1 min, c), d) 5 min, e), f) 15 min and g), h) 60 min [95]. The arrows denote the thicknesses of the films.

Since a dense and uniform microstructure is obtained when the 1L BST 50/50 film is annealed at 900 °C for 15 min we annealed the first layer in the case of all the thicker films for 15 min. In the case of the 2L BST 50/50 films the second deposited layer was annealed for 5 min and 60 min at 900 °C. Both films crystallize in the perovskite phase (the results are not shown here).

The FE-SEM cross-section and surface micrographs, presented in Figure 4.24, reveal that the films are 70-90-nm thick and have predominantly columnar microstructures, regardless of the time of annealing for the last deposited layer. A comparison of the surface microstructures of both films reveals that the average lateral grain size slightly increases with longer annealing times for the final deposited layer from ~30 nm to ~45 nm. In both films small intergranular pores are observed. Since no major differences are observed in the microstructures, i.e., grain size and shape, level of porosity, of the 2L (5 min) and 2L (60 min) films, an annealing time of 5 min was chosen for annealing of the intermediate layers when preparing thicker films.

The cross-section microstructure of the 2L (60 min) film was investigated with a scanning-transmission electron microscope (STEM), which revealed the predominantly columnar microstructure of the film with the width of the grains in the range of the film thickness, see Figure 4.25. Note that some smaller grains were also observed through the thickness of the film. The grain boundaries are clean, without any secondary phases. The results obtained with the STEM are in a good agreement with the FE-SEM analysis.

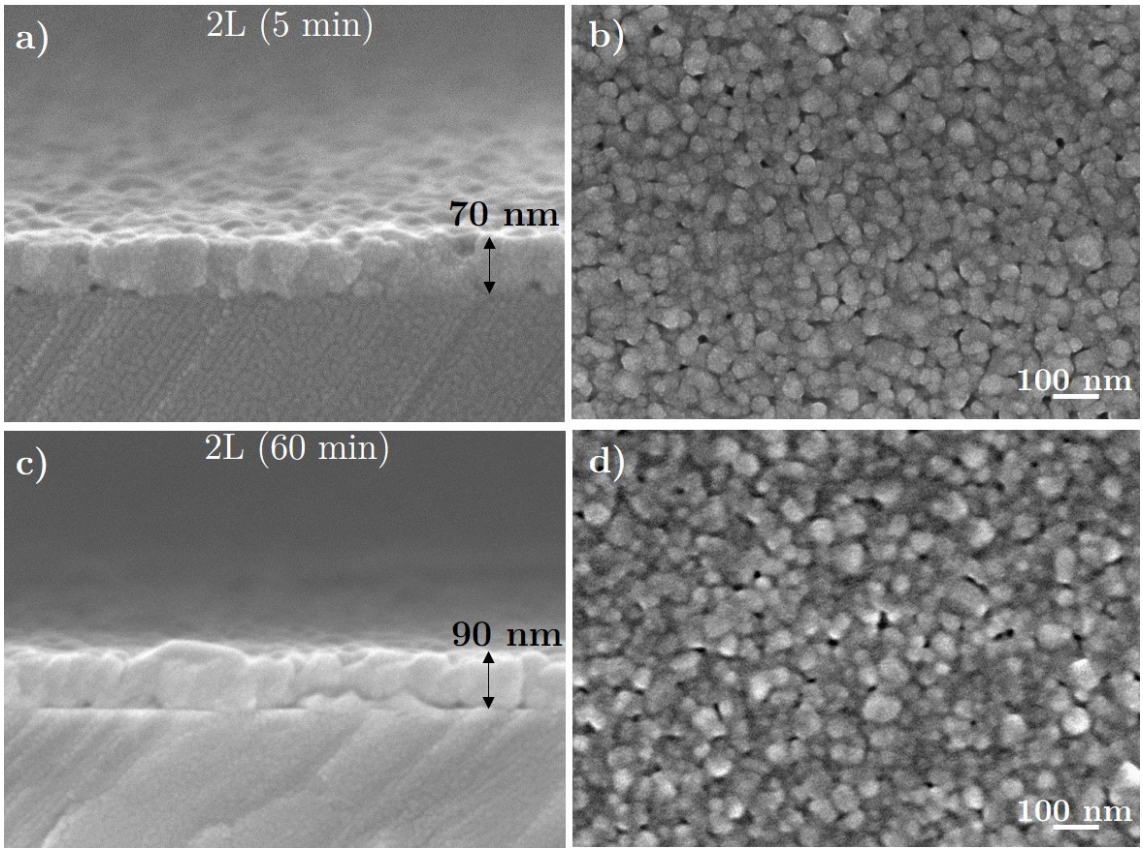


Figure 4.24: FE-SEM cross-section and surface micrographs of the a) and b) 2L BST 50/50 film annealed at 900 °C and the time of annealing of the last deposited layer a) and b) 5 min and c) and d) 60 min. The arrows denote the thicknesses of the films.

In Figure 4.25 b) a dark-field STEM micrograph of a representative columnar grain of the 2L (60 min) film is shown at a higher magnification. The interface between the two deposited layers, marked with the dotted horizontal line, is clearly seen. The crystal structure of the representative columnar grain was dark-field analyzed in selected areas marked with the numbered squares. The high-resolution high-angle annular dark-field STEM (HAADF-STEM) micrograph 1.) reveals that the interface between the alumina substrate and the film is flat with no detectable secondary phase.

The high-resolution HAADF-STEM micrograph 2.) belongs to the area on the interface between two deposited layers. It is clear that the crystal structure of the second deposited layer follows the crystal structure of the pre-existing BST 50/50 layer. The interface is clear and there are no crystal defects, such as dislocations, present in the film, which were observed in the literature for solution-derived $BaTiO_3$ and $SrTiO_3$ thin films [62]. However, some contrast change is observed across an interface, as shown by the annular dark-field (ADF) intensity profile in the inset of the figure. The change in the contrast of the ADF intensity is most probably due to the non-homogeneously distributed A-site atoms of the perovskite unit cell on the surface of the first deposited layer.

The surface of the 2L (60 min) film is clean, without any amorphous phase, as seen from the high-resolution HAADF-STEM micrograph of the selected area 3).

Homo-epitaxial growth of columnar grains in the case of the solution-derived $BaTiO_3$ and $SrTiO_3$ thin films was studied in the literature. Jia et al. [62] investigated the microstructure of columnar solution-derived $BaTiO_3$ and $SrTiO_3$ thin films prepared by a multi-step annealing process, as explained in the Introduction, Section 1.2.2.1. The thickness of an individual deposited layer was approximately 10 nm. The columnar grains were epitaxially grown on pre-existing grains. In addition, some smaller grains were also observed near the interface between the substrate and the film.

The homoepitaxially grown columnar grains in solution-derived thin films were also observed, for example, in indium tin oxide (ITO) thin films [96]. Dippel et al. [96] prepared ITO thin films on Si/SiO_2 substrates by the multi-step annealing process at 500 °C. The authors showed that when the thickness of an individual layer did not exceed 7-8 nm, columnar grains formed, which is consistent with the study by Hoffmann et al. [50].

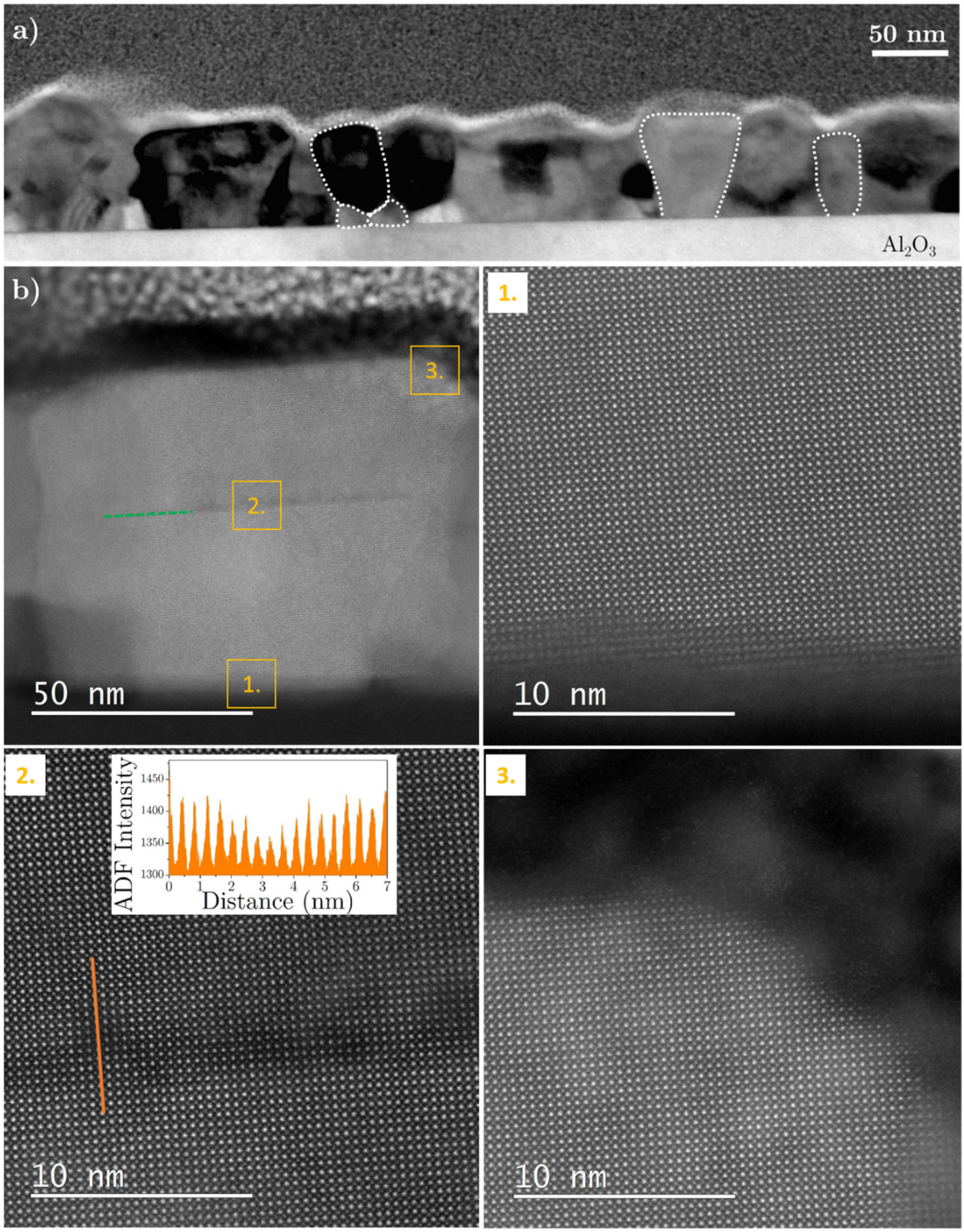


Figure 4.25: a) Cross-section bright-field TEM micrograph of the 2L (60 min) film. Individual grains are encircled with dotted lines. b) Dark-field STEM micrograph of a representative columnar grain and corresponding high-resolution HAADF-STEM micrographs of selected areas, marked with numbered squares. The dotted horizontal line shows the interface between two deposited layers. The annular dark-field (ADF) intensity profile, performed on the columns of the A-site atoms of the perovskite unit cell, in the 2nd area is included (marked with a vertical full line).

Later on, the microstructures of the BST 50/50 films consisting of three (3L) and up to six (6L) deposited layers with the time of annealing of the last deposited layer of 5 min and 60 min were investigated. XRD analyses (not shown here) confirmed that all the films crystallize in the perovskite phase. In the following text the FE-SEM results for the 3L and 6L films are shown.

The FE-SEM cross-section and surface micrographs of the 3L (5 min) and 3L (60 min) films are presented in Figure 4.26. As expected from the FE-SEM analysis of the 1L and 2L films (Figure 4.22 and Figure 4.24) the 3L films consist predominantly of columnar grains. Both 3L films, annealed for 5 min and 60 min, are approximately 115 nm thick and have dense and uniform surface microstructures. The time of annealing has no major effect on the average lateral grain size of the 3L films; in both cases it is ~55 nm. As the number of deposited layers increases from three to six, the 6L (5 min) film is approximately 200 nm thick and the predominantly columnar grains have an average lateral grain size of ~60 nm, as shown in Figure 4.27.

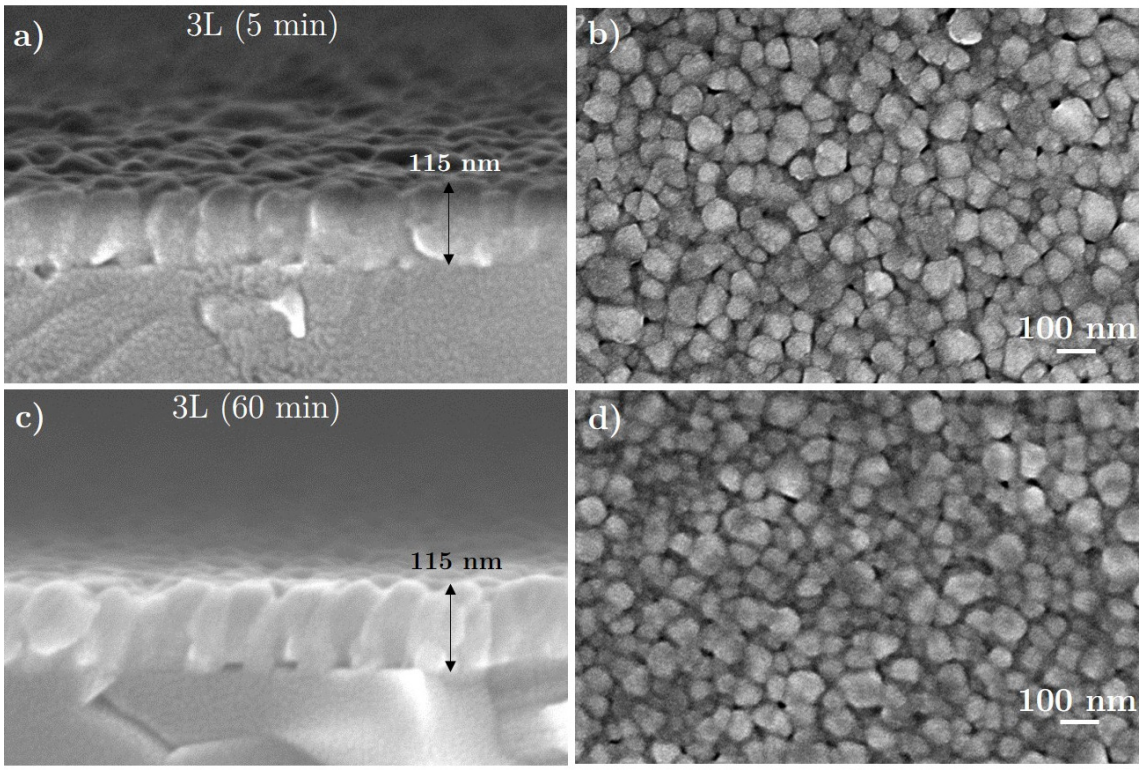


Figure 4.26: FE-SEM cross-section and surface micrographs of the BST 50/50 a), b) 3L (5 min) and c), d) 3L (60 min) films, annealed at 900 °C with different times of the annealing for the last deposited layer.

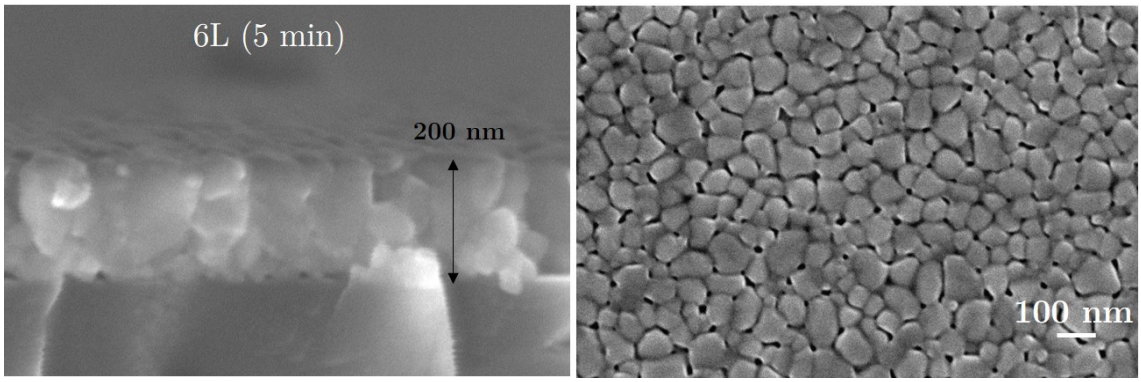


Figure 4.27: FE-SEM cross-section and surface micrographs of the 6L (5 min) film, annealed at 900 °C with the time of the annealing of the last deposited layer equal to 5 min.

In order to obtain a better insight into the development of the columnar microstructure, the grain growth during isothermal heating at 900 °C was studied for the films consisting of seven deposited layers. For consistency, the time of annealing for the first deposited layer was 15 min, and each intermediate layer was annealed for 5 min, as determined before. The 6L (5min) film (the microstructure presented in Figure 4.27) represents a "template" film for the deposition of the seventh layer, which was annealed at 900 °C for different times.

The XRD analysis of the 7L films (not shown here) revealed that upon annealing at 900 °C for different times, from 1 s to 60 min, all the 7L BST 50/50 films crystallize in the perovskite phase.

The FE-SEM cross-section and surface micrographs of the 7L BST 50/50 films are shown in Figure 4.28. After 1 s of annealing we discern in cross-section one grain, or in some places two grains, extending through the whole ~40-nm-thick layer, see Figure 4.28 a). The surface micrograph reveals that small grains with an average lateral grain size of 10-20 nm uniformly cover the template film. However, we can still discern the topography of the template films with clearly distinguishable grain boundaries.

After annealing for 1 min the boundary between the seventh layer and the template film is less evident on the level of FE-SEM. Still, we distinguish one grain per layer in some places. The surface microstructure consists of large grains of ~50 nm, with a population of much smaller grains of ~20-nm across located on their boundaries. We also observe pores located at the junctions of the large grains.

As the annealing time increases to 5 min and 60 min, the columnar microstructure with surface grooves in the cross-section micrographs is evident, see Figure 4.28 c) and d). The surface microstructure of the film annealed for 5 min consists of large grains of ~80 nm across. Fine pores between the grains are observed. By increasing the annealing time to 60 min, the grain size increases slightly to ~90 nm and the fraction of intergranular pores decreases.

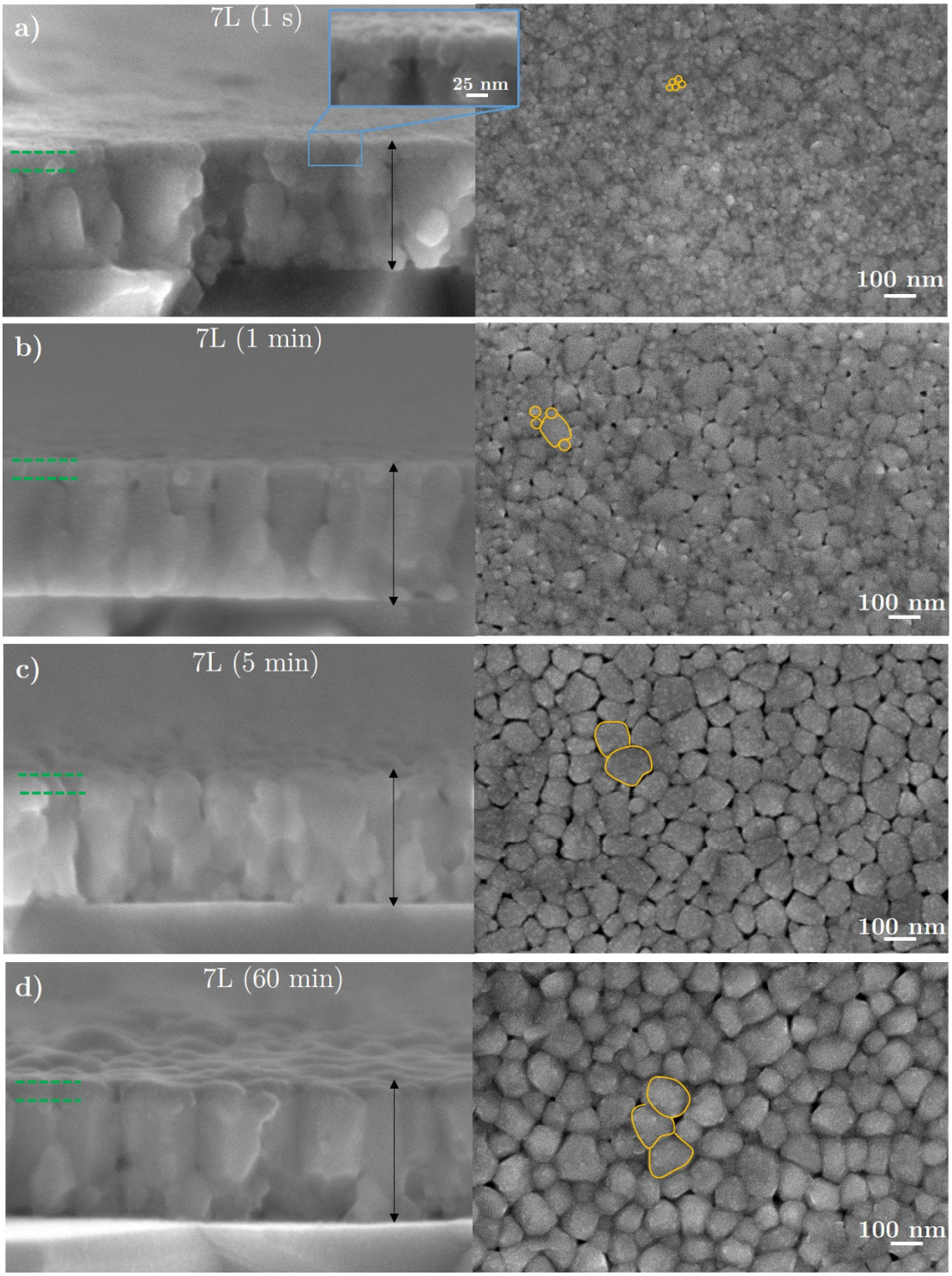


Figure 4.28: FE-SEM cross-section and surface micrographs of the BST 50/50 a) 7L (1 s), b) 7L (1 min), c) 7L (5 min) and d) 7L (60 min) films, annealed at 900 °C with different times of annealing for the last deposited layer. The arrows in the cross-section micrographs denote the thicknesses of the whole films and the horizontal dotted lines mark the thickness of the last deposited layer. The inset of the cross-section micrograph a) shows a part of the last deposited layer at a higher magnification. In the surface micrographs individual grains are encircled.

The surface microstructures of the 7L BST 50/50 films were also examined with an atomic force microscope (AFM). The surfaces of the films were scanned over a 1 µm × 1 µm area and the corresponding height and deflection topography micrographs are presented in Figure 4.29. For each film the images were obtained in different regions and they were found to be similar. The AFM micrographs of the template and the 7L films after different annealing times are consistent with the FE-SEM analysis, presented in Figure 4.27 and Figure 4.28.

The surface profiles, obtained from the topography height images over the length of 300 nm, are collected in Figure 4.30. Moreover, the vertical surface roughness, calculated for an area of 1 µm × 1 µm and expressed as the root-mean-square (RMS) roughness, is included.

On the profile curve of the template film each dome-shaped top corresponds to a single grain with an average lateral size of approximately 60 nm, which correlates well with the FE-SEM result. The boundaries between the columnar grains with pronounced grooves are marked with vertical dotted lines. The corresponding RMS value is 3.4 nm.

In the case of the 7L (1 s) film the surface profile contains the wave-like baseline that is less pronounced than in the template film, and which includes superimposed fine grooves, indicating the boundaries of the ~20 nm grains. The drop of the RMS value from 3.4 nm for the template film to 1.9 nm for the 7L (1 s) film is attributed to the film-deposition technique. When the precursor solution is spin-coated on the top of the template film with well-developed grains, it uniformly covers and flattens the surface. Grooving occurs upon crystallization and grain growth.

A similar wave-like surface profile is also observed for the 7L (1 min) and even more for the 7L (5 min) sample. The dome-shaped tops appear and they correspond well to the large grains determined by FE-SEM. With increasing time the fine grooving progressively disappears. The RMS values are about 2.5 nm.

The 7L (60 min) film topography consists of domes with diameters of approximately 90 nm, and with the RMS value of 5.6 nm.

In agreement with the study by Rost et al. [23] we ascribe the increase in the RMS value with increasing annealing time to the grain growth. As explained in the Introduction, Section 1.1.4, the authors investigated the surface of polycrystalline Au thin films upon growth using a scanning-tunneling microscope (STM). The RMS increases in parallel with the grain size due to the balancing of the surface energy and the grain-boundary energy where the boundaries intersect the surface of the film, resulting in the formation of the grooves that increase the surface roughness.

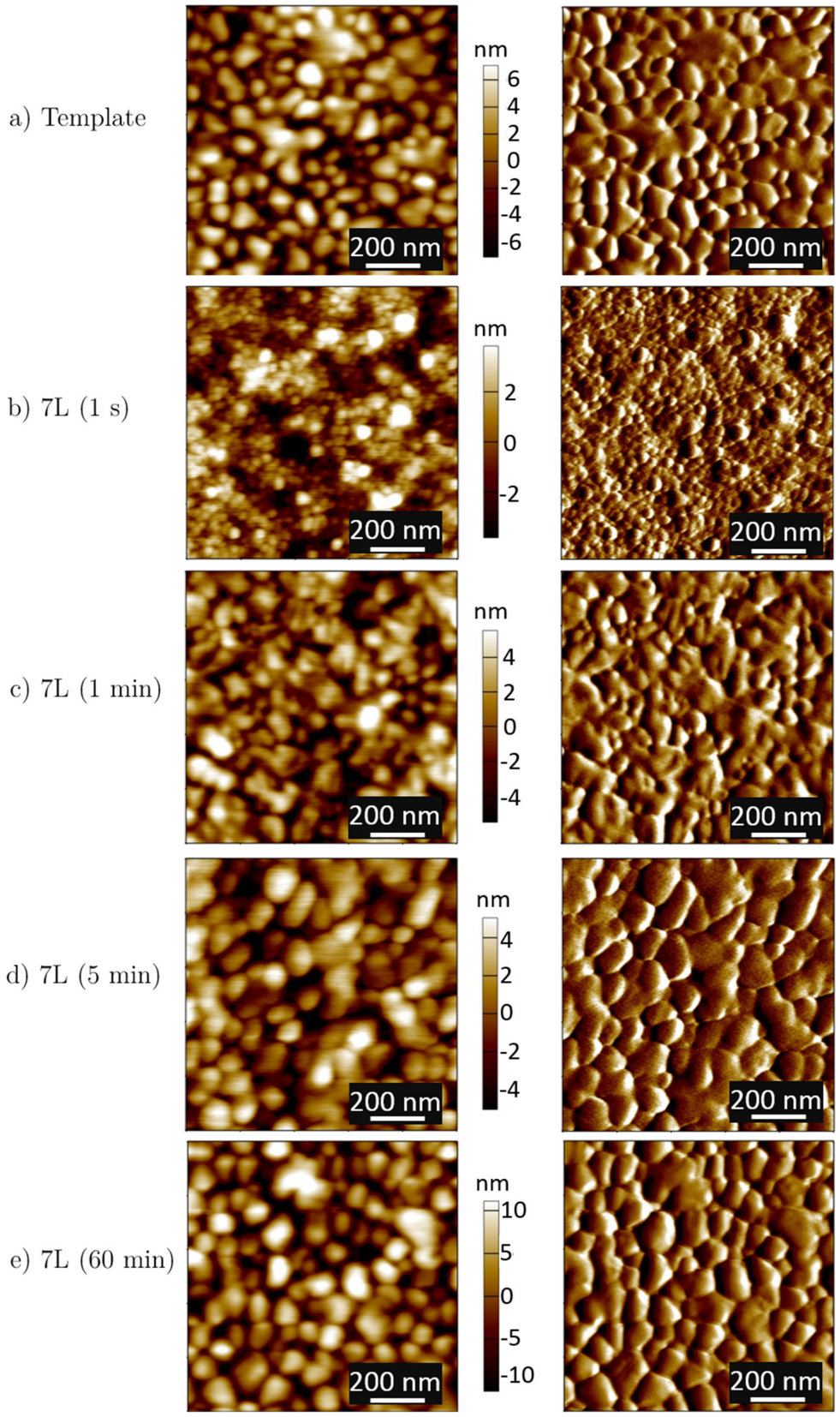


Figure 4.29: AFM topography images (left: height, right: deflection) of the template, 7L (1 s), 7L (1 min), 7L (5 min) and 7L (60 min) films.

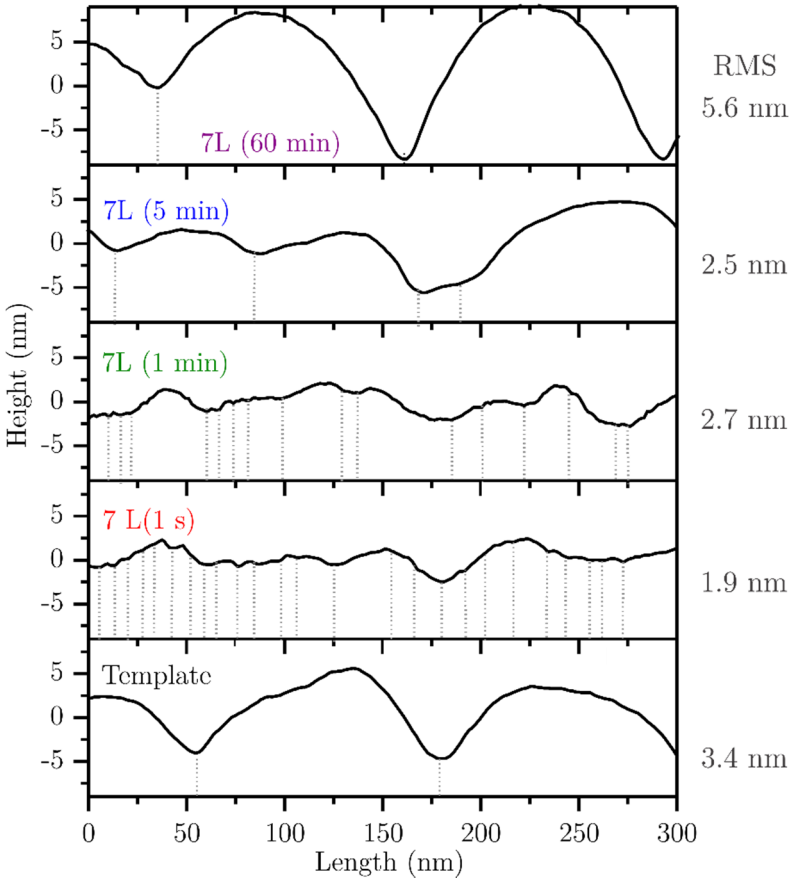


Figure 4.30: AFM surface profiles of the template film, 7L (1 s), 7L (1 min), 7L (5 min) and 7L (60 min) films. Vertical lines represent the grain boundaries. The root-mean-square (RMS) roughness calculated for an area of 1 µm × 1 µm shown in Figure 4.29.

The microstructure of our 7L (60 min) film was investigated by STEM and the corresponding micrographs are collected in Figure 4.31. In agreement with the FE-SEM cross-section micrographs the cross-section bright-field TEM analysis revealed a predominantly columnar microstructure of the film (see Figure 4.31 a)). The grain boundaries are clean, without any secondary phases. The width of the columns is approximately 90 nm, which is consistent with the average lateral grain size determined on the FE-SEM surface micrographs. The interface between the alumina substrate and the film is flat, and without any interfacial layers. However, some amorphous regions are found on the interface between the substrate and the film, as marked with the dotted lines in the bright-field and dark-field STEM micrographs (see Figure 4.31 b) and c)).

At the junction of the grain boundaries and the surface, there are grooves that developed as a consequence of the energy balance between the grain boundary and the surface [20]. In Figure 4.31 b) and c) bright- and dark-field STEM micrographs of a representative columnar grain of the film are shown, where the boundaries between seven deposited layers can be discerned. The high-resolution HAADF-STEM micrographs of the crystal structure of the columnar grain and the boundary between individual layers are shown in Figure 4.31 (1.) and (2.). The analysis reveals no crystal defects within the individual layers. However we observe the contrast change in the high-resolution HAADF-STEM micrograph (1.) at the interface between two deposited layers, which is ascribed to the non-homogeneous distribution of the Ba and Sr atoms. Such a contrast change was also found in the 2L (60 min) film, see Figure 4.25.

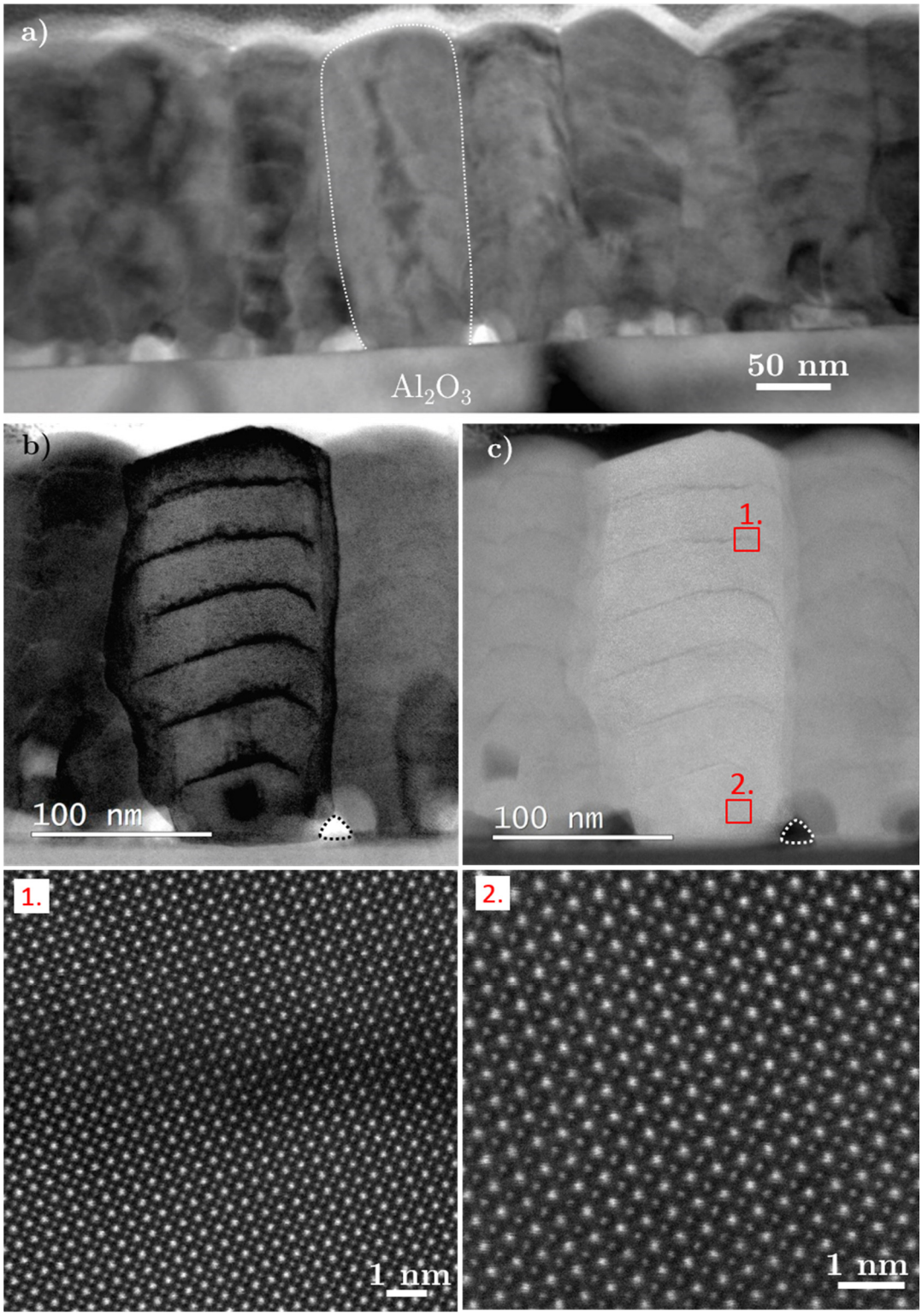


Figure 4.31: a) Bright-field TEM cross-section micrograph of the 7L (60 min) BST 50/50 film annealed at 900 °C. The columnar grain is encircled. b) Bright-field STEM and c) dark-field STEM micrographs showing a representative columnar grain. The dotted lines mark the porous area on the interface between the film and the substrate. High-resolution HAADF-STEM images (1.) and (2.) show the crystal lattice of the columnar grain in the areas as marked in c).

The STEM analysis confirmed that the crystal structure of the underlying BST 50/50 layer continues as the next deposited layer is annealed, regardless of the number of the deposited layers in the 900 °C, multi-step annealing process. Such homo-epitaxial growth within one columnar grain is consistent with Jia et al. [62], see also Section 1.2.2.1.

In Figure 4.32 the average lateral grain size of the BST 50/50 films prepared by the multi-step annealing process at 900 °C is plotted as a function of the number of deposited layers. In all cases the last deposited layer was annealed for 60 min. We observe that by increasing the number of deposited layers the average lateral grain size increases from ~35 nm for the 1L film, which is 40 nm thick, to almost 90 nm for the 6L film, which is 210 nm thick.

But for the case of seven deposited layers, corresponding to a film thickness of 240 nm, the average lateral grain size does not change. We showed previously that even by increasing the film thickness to 600 nm the grain size only slightly increases to ~100 nm, see Figure 4.8. This phenomenon may be related to the stress-relaxation mechanism. The BST 50/50 films with thicknesses less than 210 nm are under a significant tensile stress, which is induced in the films due to the difference in the thermal expansion coefficients of the film and the alumina substrate upon annealing. At the critical film thickness, ≥210 nm in our case, the stress relaxes via crack formation. We assume that the cracks hinder the grain growth in thin films with thicknesses above the critical value.

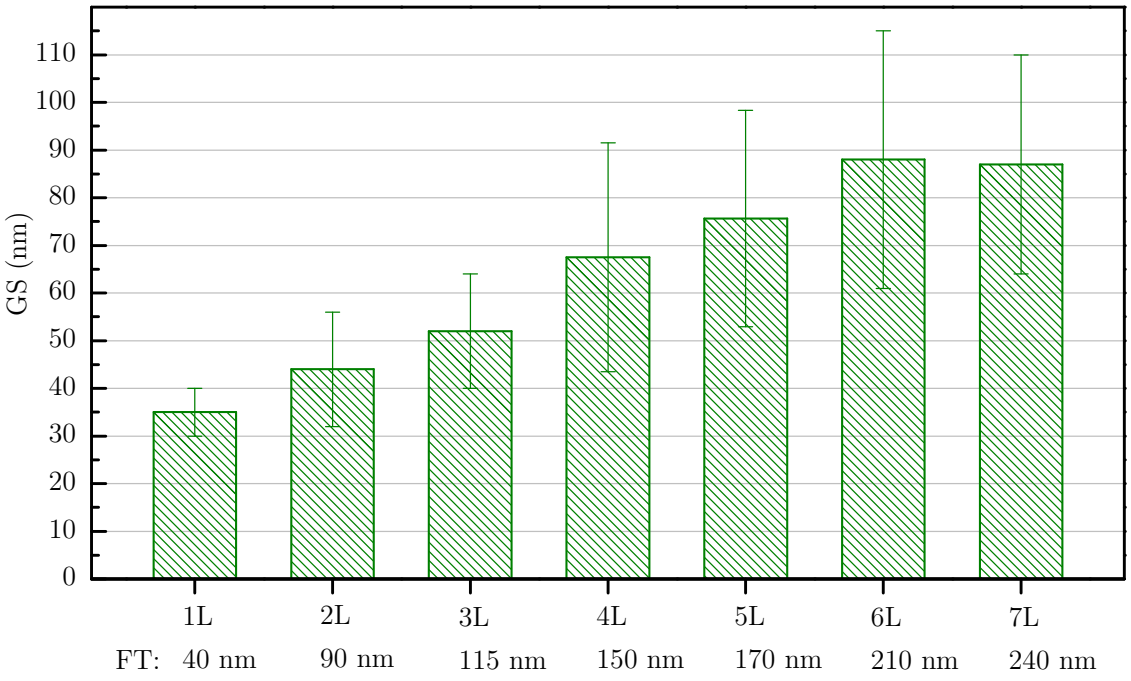


Figure 4.32: The average lateral grain size of the BST 50/50 films plotted as a function of the number of layers and the corresponding thicknesses of the films (FT). The time of the final annealing at 900 °C was, in all cases, 60 min.

In general, the grain-size dependence on the film thickness was explained as the specimen-thickness effect by Mullins et al. [20], see Section 1.1.4. The grain growth is controlled by the balance between the surface energy of neighboring grains and the energy of the grain boundaries, resulting in the formation of grooves. Stech et al. [22] observed that the grain growth in titania thin films stops when the average grain size is in the range of the film thickness. Palmer et al. [21] showed that the grain growth stops when the average grain size is ~2.5 times higher than the film thickness. This value agrees well with the modelled grain size at stagnation by Frost et al. [24], where the ratio of the grain size to the film thickness is 2.9.

We plotted the ratio of the average lateral grain size and film thickness (GS/FT) as a function of the number of deposited layers, or film thickness, in Figure 4.33 a). The GS/FT ratio is the highest, 0.7, for the 1L film and it decreases to 0.49 for the 2L film. With further increase of the film thickness the GS/FT ratio only slightly decreases, reaching a value of 0.42 for the 6L film. The lateral grain size is smaller than the film thickness and this difference is even more pronounced with an increasing film thickness. This observation is in contrast to the literature data, showing that the grain-growth suppression occurs when the GS/FT$\leq$2.5 [20], [21], [22].

In addition, we plotted the ratio of the average lateral grain size and the single layer thickness (GS/SLT), see Figure 4.33 b). For the 1L film the GS/SLT$\approx$1. With an increasing number of deposited layers up to 6L the GS/SLT ratio is increasing, meaning that the lateral grain size is progressively larger than the thickness of an individual layer. The obtained values correspond well to the values obtained by Mullins et al. [20], Stech et al. [22] and Palmer et al. [21]. We note that for the 7L film the GS/FT and GS/SLT ratios do not fully follow the relation obtained for the thinner films, which could be tentatively related to the presence of nano-cracks, as explained earlier.

To verify whether the BST 50/50 film microstructures are stable after the multi-step annealing at 900 °C, 60 min, selected films were additionally annealed for 480 min and the resulting FE-SEM micrographs are presented in Figure 4.34. The microstructures of the 2L and 4L films reveal well-developed columnar grains with respective average lateral grain sizes of 50 nm and 70 nm. These values are almost the same as the grain sizes of the respective films, annealed for 60 min, compare Figure 4.24 c), d), confirming that the respective microstructures are in thermodynamic equilibrium already after 60 min.

We ascribe the contradiction in results with respect to the above references to the different annealing processes of the films. In the mentioned studies the films were annealed in one step, while in our case each deposited layer is annealed separately. Consequently, each subsequent layer is deposited on the pre-existing polycrystalline layer, which represents a template layer for the next deposit. In our case, however, the GS/SLT ratio is increasing, but we do observe a region of grain-growth stagnation for the 2L–6L films, where the GS/FT $\approx$ 0.45, with the exception of the thinnest 1L film.

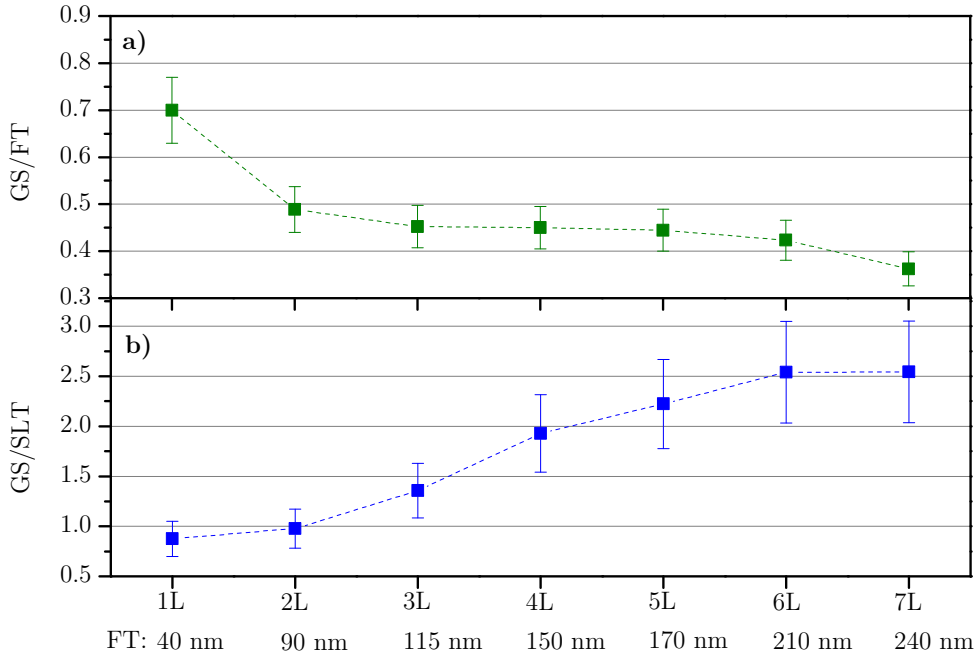


Figure 4.33: a) The ratio of the average lateral grain size (GS) and the film thickness (FT) plotted versus the number of deposited BST 50/50 layers. b) GS/SLT ratio plotted as a function of the number of deposited layers. The time of the final annealing at 900 °C was in all cases 60 min.

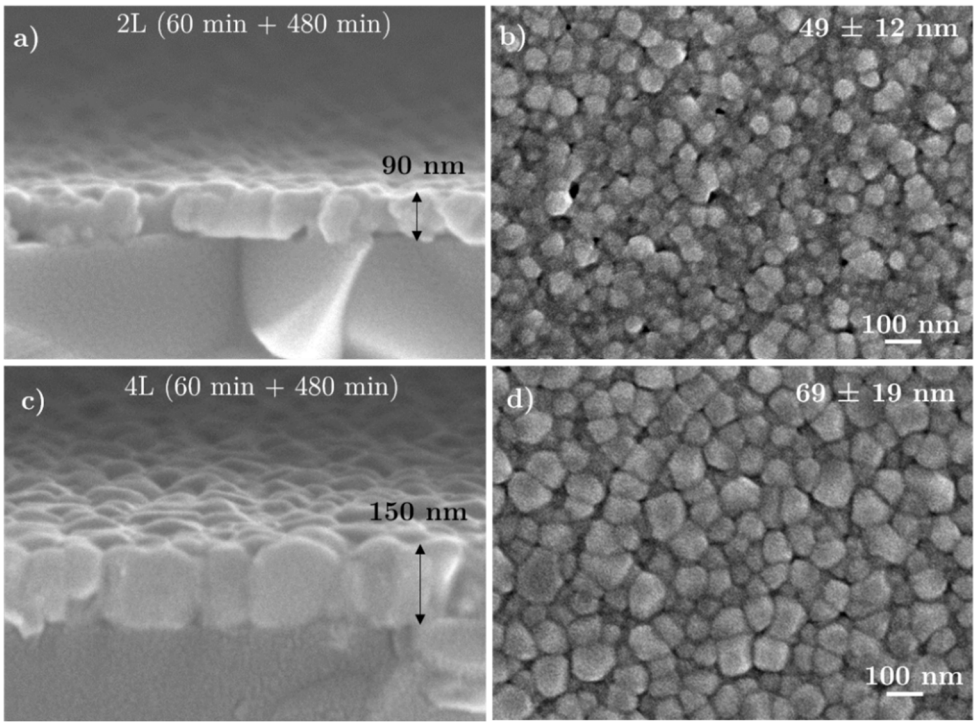


Figure 4.34: FE-SEM cross-section and surface micrographs of the a), b) 2L (60 min + 480 min) and 4L (60 min + 480 min) films, annealed at 900 °C with the time of the annealing for the last deposited layer being 60 min and additionally 480 min.

Chapter 5

Summary and Conclusions

In the thesis we report on and discuss the dielectric properties of solution-derived $Ba_{0.5}Sr_{0.5}TiO_3$ (BST 50/50) thin films, their crystallization and the evolution of their microstructures. The studied films were prepared from a solution of alkaline-earth acetates and Ti-butoxide in acetic acid/2-methoxyethanol solvents with the C_M=0.25 on polycrystalline alumina substrates. After spin-coating the films were dried, pyrolyzed and heated in a rapid thermal annealing furnace. In the case of the multi-step annealing, the deposition-drying-pyrolysis-annealing steps were repeated for each deposited layer until the final thickness was achieved.

The BST 50/50 thin films with thicknesses between 90 nm and 600 nm that were multi-step annealed at 900 °C were studied in the first part. The 90-nm- and 600-nm-thick films consisted of, respectively, two and eighteen deposited layers with an average thickness of 35-40 nm. All the films had predominantly columnar microstructures, as determined with a field-emission scanning electron microscope (FE-SEM). The average lateral (i.e., in-plane) grain size of the thinnest, 90-nm-thick, film was 45 nm and it increased to ~80 nm for the 170-nm-thick film. With a further increase of the thickness to 600 nm the lateral grain size only slightly increased.

The X-ray diffraction (XRD) analysis showed that upon annealing all the BST 50/50 films crystallized in a pure perovskite phase. We applied a two-dimensional XRD method for a determination of the stress state in the films and found that the in-plane d-spacing increased with increasing tilting angle, i.e., the angle between the film normal and the tilt of the sample. This increase indicated the presence of the biaxial tensile stress in the films, which was due to the thermal-expansion mismatch between the film and the substrate. The magnitude of the tensile stress was 344 MPa and 378 MPa for the 90-nm- and 170-nm-thick films, respectively. With a further increase of the thickness the stress decreased, as discussed below.

Measurements of the room-temperature dielectric properties showed a non-monotonic thickness dependence, which could be divided into three groups. We note that the dielectric permittivity at 10 and 15 GHz showed the same trend as at 100 kHz, but with slightly lower values. The dielectric permittivity for the thinnest, 90-nm-thick film was 650 at 100 kHz, and it increased to 1250 for the 170-nm-thick film. Here, the increase of the grain size with increasing film thickness coincided with the increase of the permittivity. We explain such behavior as the dielectric grain-size effect [63].

In the next thickness range, between 170 nm and 240 nm, the grain size almost did not change and also the permittivity only slightly increased with an increasing film thickness. In parallel, a strong decrease of the initially high value of the tensile residual stress occurred, indicating some stress relaxation. The decrease of the stress became even more pronounced as the thickness increased further from 240 nm to 600 nm. Here, the grain size

remained almost unchanged, while the permittivity value strongly decreased to ~800. The drop of the tensile stress with the film thickness, to ~120 MPa for the 400- and 600-nm-thick films, indicates a progressive stress relaxation, which occurred in the films via the formation of intergranular cracks in the thicker films. The reduction of the dielectric permittivity of the films in this thickness range is connected to the presence of intergranular cracks and can be explained with the brick-wall model.

The temperature-dependent dielectric permittivity measured at 5 kHz showed a broad maximum between 300 K and 150 K for the thinnest, 90-nm-thick films. With an increase of the thickness the maximum became more pronounced and its position decreased from 277 K for the 170-nm-thick film to 250 K for the 600-nm-thick film. Down-shifting of the permittivity maximum with increasing film thickness was also observed in the GHz range and showed a strong resemblance to the decrease of the tensile residual stress. Our results are in a good qualitative agreement with the phenomenological theory and experimental observations of the permittivity maximum dependence on the biaxial strain in polycrystalline $BaTiO_3$ thin films [91], [92].

The tunability of the dielectric permittivity in the voltage range from -40 V to +40 V was 2.2 for the 90-nm-thick film, and it reached almost 4 for the films with thicknesses between 115 nm and 170 nm. Such high tunability values are attributed to the high values of permittivity and also a high level of tensile stress in the respective films. With a further film-thickness increase the tunability showed a similar trend as observed for the dielectric permittivity, dropping to ~1.9 for the 600-nm-thick film.

In the first part of the thesis we showed that the film thickness, the grain size and the presence of residual thermal stress strongly influence the dielectric properties of the BST 50/50 thin films. We note that the room-temperature dielectric permittivity of the films with thicknesses ≤240 nm in both the kHz and GHz ranges is high compared to the values reported for BST films with a similar composition, film thickness and grain size, regardless of the deposition method and the electrode configuration [40], [48], [57]; e.g., 1350 at 100 kHz for the 240-nm-thick film. We connect the good dielectric properties of the films to the optimized processing conditions, i.e., the separation of the drying-pyrolysis-rapid thermal annealing steps for the efficient removal of organics and an annealing temperature of 900 °C, which resulted in dense and predominately columnar microstructures.

In the second part we studied the crystallization and evolution of the microstructure of BST 50/50 films consisting of seven deposited layers and multi-step annealed at temperatures between 600 °C and 900 °C. According to XRD the films crystallized into a pure perovskite phase at ~640 °C. The microstructure of the ~310-nm-thick film annealed at 640 °C consisted of equiaxed grains that were ~20 nm across, as evidenced by FE-SEM. As the annealing temperature increased to 720 °C the film thickness decreased to ~260 nm and the size of the equiaxed grains increased to ~30 nm. With a further increase of the annealing temperature the thickness of the films remained almost unchanged.

The average lateral grain size of the film annealed at 800 °C was ~40 nm, reaching the thickness of individual deposited layers. The transmission electron microscopy analysis of the films annealed at 700 °C and 800 °C confirmed the absence of any secondary phases on the grain boundaries or at the interface between the film and the substrate.

Upon multi-step annealing of the films at 840 °C, the average lateral grain size was ~40 nm, but from the cross-section microstructural analysis it was evident that some grains extended through a few deposited layers. Upon annealing at/above 880 °C the films consisted of predominantly columnar grains, i.e., grains extending across the whole film thickness, with an average lateral size of ~90 nm.

We compared our results with the structural zone model for solution-derived thin films, which distinguishes three types of microstructure according to their crystallite (grain) size

(ICS), single layer thickness (SLT) and annealing temperature [28, 29]. Depending on the ICS/SLT ratio, the microstructure is granular, i.e., consisting of fine equiaxed grains, (ICS<SLT), layered (ICS≈SLT), or columnar (ICS>SLT). We found that under our experimental conditions, the granular microstructure developed for ~0.1 ≤ICS/SLT≤ ~1. The layered microstructure was found only at ICS/SLT~1.2; according to the literature such a microstructure was only rarely observed in $BaTiO_3$, $SrTiO_3$ or BST films. The columnar microstructure was obtained for an ICS/SLT ratio of ~2.5, which is lower than the literature data (3.5–16.7, see Appendix A) and could be explained by the high annealing temperature used in our study, 900 °C.

We studied the evolution of the columnar microstructure of BST 50/50 films upon multi-step annealing at 900 °C. The films were composed of up to seven layers. We observed that the time of annealing, 5 min or 60 min, did not noticeably influence the microstructure of the respective films. The microstructure of the film consisting of one deposited layer, which was ~40 nm thick, was columnar with an average lateral grain size of ~30 nm. With an increasing number of deposited layers, from two up to six, the columnar microstructure persisted and the average lateral grain size progressively increased to ~80 nm.

When the seventh deposited layer was annealed for 1 s, it consisted of one grain, or in some places of two grains per layer thickness (~40 nm). The average lateral grain size was 10-20 nm and it gradually increased to ~90 nm as the annealing time increased to 60 min. At the same time, the root-mean-square roughness (RMS) increased from 1.9 nm to 5.6 nm for 1 s and 60 min annealing time, respectively. The increased RMS values corresponded to progressively more pronounced grooving as the lateral grain size was increasing. We note that the formation of grooves is a consequence of the balancing of the surface energy and the grain-boundary energy where the grain boundaries intersect the surface of a film [20, 23].

The cross-section microstructure of the film, prepared by multi-step annealing of seven deposited layers at 900 °C for 60 min was investigated with the scanning-transmission electron microscope. No secondary phase was found on the grain boundaries or at the interface between the film and the alumina substrate. The analysis of an individual columnar grain confirmed that the crystal structure of the underlying layer continued as the next deposited layer was annealed, regardless of the number of the deposited layers; meaning that the growth within an individual grain proceeded homo-epitaxially.

In summary, we showed in this part of the Thesis that at our experimental conditions the BST 50/50 films crystallize in perovskite phase upon multi-step annealing at/above 640 °C. The microstructure of the films is granular upon annealing at temperatures ≤800 °C, while at temperatures ≥ 880 °C the microstructure is predominantly columnar. The evolution of different types of microstructure depends on the ratio between the grain size and the thickness of individual deposited layers, in agreement with the structural zone model for solution-derived thin films. The evolution of the columnar microstructure upon annealing at 900 °C proceeds via crystallization and growth of fine, equiaxed grains of 10-20 nm across within an individual, ~40 nm thick layer on top of preexisting columnar grains followed by homo-epitaxial overgrowth within each grain.

Appendix A

Data for Structural Zone Model for Solution-Derived $BaTiO_3$, $SrTiO_3$ and BST Thin Films

In table A.1 we collected the data for different solution-derived $BaTiO_3$, $SrTiO_3$ and BST thin films from the literature. In the Introduction, Section 1.2.2, the collected data is plotted as the intrinsic crystallite size (ICS) versus the single layer thickness (SLT) and the ICS/SLT ratio versus the ratio of the annealing temperature and the melting temperature (T_{anneal}/T_M), according to the structural zone model for solution-derived thin films, as proposed by Schuler et al. [28].

Table A.1: Data for different $BaTiO_3$, $SrTiO_3$ and BST thin films. (O-S – one-step, T-S – two-step and M-S – multi-step annealing, T_{anneal} – annealing temperature, ICS – intrinsic crystallite size, SLT – single layer thickness)

Material	*Annealing, T_{anneal} (°C)*	*Microstructure*	*Thickness (nm)*	*No. of deposits*	*Grain size (nm)*	*ICS (nm)*	*SLT (nm)*	*ICS/SLT*	*Ref.*
STO	M-S, 750	Columnar	200	22	100-200	150	9	16.7	[50]-1
BTO	M-S, 750		200	22	100-150	125	9	13.9	[50]-2
BST 70/30	M-S, 800		300	8	150	150	29	5.2	[55]-1
BTO	MS, 750		204	12	30-50	80	17	4.7	[17]-1
BST 70/30	M-S, 800		300	8	100	100	29	3.5	[55]-2
STO	M-S, 700	Layered?	250	5	120	120	50	2.4	[51]-1
BTO	M-S, 900	Layered	520	6	185	185	87	2.1	[56]-1
BST 50/50	M-S, 700	Layered?	250	5	70	70	50	1.4	[51]-2
BST 70/30	M-S, 750	Layered	300	8	40	40	38	1.0	[55]-3
BTO	M-S, 700	Layered?	250	5	40	40	50	0.8	[51]-3
BST 70/30	M-S, 650	Granular	230	8	25	25	29	0.8	[55]-4
BST 70/30	M-S, 750		300	8	25	25	38	0.7	[55]-5
BST 70/30	M-S, 650		250	8	20	20	31	0.6	[55]-6
BTO	O-S, 750		240	3	30-50	40	80	0.5	[17]-2
STO	O-S, 750		200	6	40-80	60	200	0.3	[50]-3
BST 30/70	T-S, 700		300	6	80	80	300	0.3	[53]-1
BTO	O-S, 750		200	6	40-50	45	200	0.2	[50]-4
BTO	O-S, 900		570	6	100	100	570	0.2	[56]-2
BST 30/70	T-S, 700		400	6	40-45	42.5	400	0.1	[53]-2
BTO	O-S, 750		300	5	20-60	40	300	0.1	[49]-1

Appendix B

Analysis of the Residual Stress in Thin Films Using 2D XRD Method

In terms of the scale at which the stresses are balanced, the residual stresses can be categorized into microscopic and macroscopic. The former appear in the range from 1 nm to 100 nm and are typically caused by crystal defects, such as dislocations, stacking faults and clusters of interstitials. Macroscopic stresses correspond to the average of the strains in ranges as large as from several 100 µm to the mm-scale [82].

The residual macroscopic stresses that may be present in thin films are further divided into two broad categories, growth or intrinsic stresses and induced or extrinsic stresses [74]. Growth stresses arise during the growth on substrates or adjacent layers. The mechanisms behind their appearance are cluster coalescence, grain growth, incorporation of impurities, etc. The second category of the stresses arises from the external factors in the physical environment of the film material. In the case of the solution-derived films, the thermal stress is the most commonly present external stress. It is induced due to the mismatch in the thermal expansion coefficients of the substrate and the film during cooling from the high processing temperatures [74]. Its presence strongly modifies the functional properties of the films, as discussed for the case of the dielectric properties of the BST films in the Introduction to this thesis, Section 1.2.2.2. For this reason a careful investigation of the stress state in the films is needed.

B.1 Basic relations

The stress σ_{ij} in a thin film on a substrate in the coordination system $S_1S_2S_3$ (as shown schematically in Figure B.1) is described by the matrix, which contains nine components [82]:

$$\sigma_{ij=}\begin{bmatrix}\sigma_{11} & \sigma_{12} & \sigma_{13}\\ \sigma_{21} & \sigma_{22} & \sigma_{23}\\ \sigma_{31} & \sigma_{32} & \sigma_{33}\end{bmatrix}. \tag{B.1}$$

For the case of isotropic materials, there are only two independent elastic constants, the Young's modulus E and the Poisson's ratio ν, which are sufficient to describe the stress and strain ε_{ij} relations of the material:

$$\begin{aligned}\sigma_{11} &= \varepsilon_{11}E + \nu(\sigma_{22} + \sigma_{33}),\\ \sigma_{22} &= \varepsilon_{22}E + \nu(\sigma_{33} + \sigma_{11}),\\ \sigma_{33} &= \varepsilon_{33}E + \nu(\sigma_{11} + \sigma_{22}),\end{aligned} \tag{B.2}$$

$$\sigma_{12} = \frac{\varepsilon_{12}E}{(1+\nu)},$$
$$\sigma_{23} = \frac{\varepsilon_{23}E}{(1+\nu)},$$
$$\sigma_{31} = \frac{\varepsilon_{31}E}{(1+\nu)},$$
$$\sigma_{21} = \frac{\varepsilon_{21}E}{(1+\nu)},$$
$$\sigma_{32} = \frac{\varepsilon_{32}E}{(1+\nu)},$$
$$\sigma_{13} = \frac{\varepsilon_{13}E}{(1+\nu)}.$$

Under equilibrium the shear components must maintain the relation:

$$\sigma_{12} = \sigma_{21},\ \sigma_{13} = \sigma_{31} \text{ and } \sigma_{23} = \sigma_{32}. \tag{B.3}$$

Since the film is clamped on the substrate the stress acts only along two axes (S_1 and S_2, see Figure B.1) in the plane of the film and the stress perpendicular to the free surface is zero, $\sigma_{33} = 0$. In this case we speak about biaxial stress. In the case of equibiaxial stress $\sigma_{11} = \sigma_{22}$, there are no in-plane (S_1 -S_2) shear components [82].

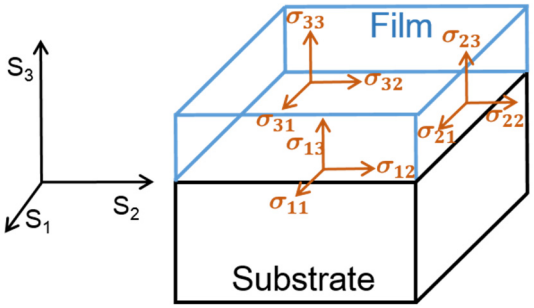


Figure B.1: Stress components (σ_{ij}) in thin film on the substrate.

B.2 Strain determination by the conventional XRD

In addition to the phase identification, texture measurement and a determination of the crystallinity of the materials, X-ray diffraction (XRD) is also used for a determination of the residual stress in the films. The microscopic strain can be determined based on the broadening of the diffraction peaks [97], while the macroscopic stress causes their shifting. In this chapter we only discuss the determination of the macroscopic stress in the films by XRD.

The strain in the crystalline film causes changes in the lattice parameters d in comparison to the value of the unstressed crystal, d_0, which provide a measure of the elastic strain components in the film. In the conventional stress measurement by XRD, with a point or line detector, the intensity of the scattered X-ray beam is monitored as a function of the diffraction angle 2θ around a chosen diffraction peak for several orientations. The orientations are defined by the angle ϕ, which is the angle of rotation of the sample along its normal (S_3), and ψ, which is the tilting angle from the sample's normal within a plane defined by L and S_3, as schematically presented in Figure B.2. The determined 2θ shift of the diffraction peak, measured by XRD, corresponds to the strain in the specific direction [74], [82], [98].

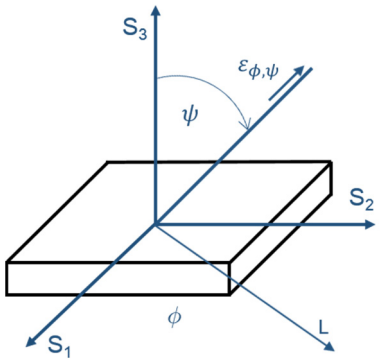


Figure B.2: Schematic presentation of the strain-measurement geometry in the conventional X-ray diffraction for the sample coordinates $S_1S_2S_3$ [82].

An example of the experimental results obtained by the conventional XRD for the (110) diffraction peak of a BST 50/50 film is schematically shown in Figure B.3. A shift of the diffraction peak towards the lower 2θ values with the increasing tilting angle indicates that the in-plane unit cell is becoming larger and the residual stress is tensile (Figure B.3 a)). On the other hand, in Figure B.3 b), the diffraction peak shifts towards higher 2θ angles, because the in-plane unit cell is getting smaller due to the compressive stress.

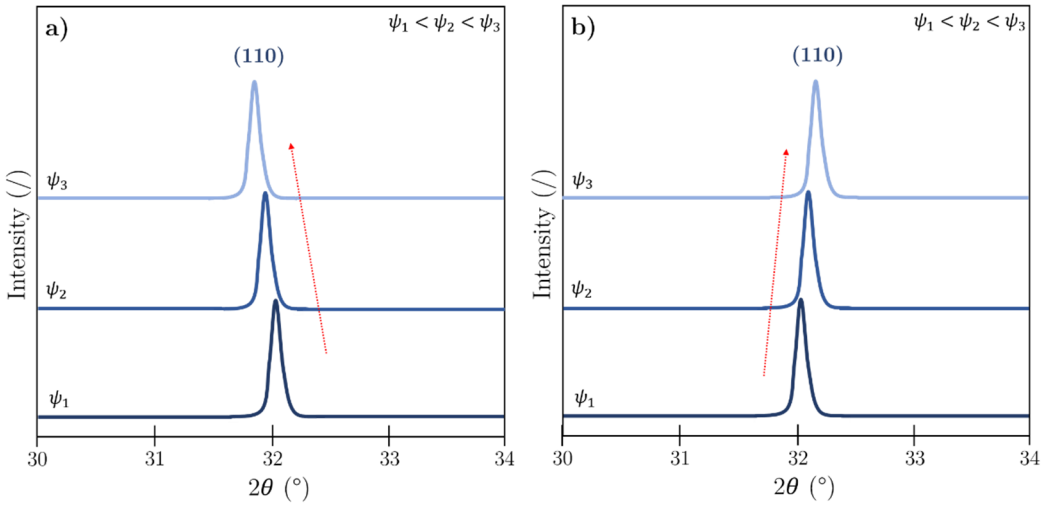


Figure B.3: Schematics of the XRD pattern of the (110) diffraction peak of the BST 50/50 film, obtained from the measurement by conventional XRD. Shifting of the peak position due to the a) tensile and b) compressive stress.

The measured normal stress σ_ϕ and shear stress τ_ϕ are then given by the stress-tensor components in the sample coordinates $S_1S_2S_3$ by:

$$\begin{aligned} \sigma_\phi &= (\sigma_{11}\, cos^2\,\phi + \sigma_{22}\, sin^2\,\phi + \tau_{12}\, sin\, 2\phi) \\ \tau_\phi &= (\sigma_{13}\, cos\,\phi + \sigma_{23}\, sin\,\phi). \end{aligned} \tag{B.4}$$

Taking into account the stress and strain relations (Eq. (B.2)) for an equibiaxial stress we have:

$$\varepsilon_{\phi\psi} = \tfrac{1+\nu}{E}\sigma_\phi\, sin^2\,\psi - \tfrac{2\nu}{E}(\sigma_{11}). \tag{B.5}$$

The above equation shows that the measured strain is a linear function of $sin^2\,\psi$. By taking the first derivative with respect to $sin^2\,\psi$ we obtain:

$$\frac{\partial \varepsilon_{\phi\psi}}{\partial sin^2\,\psi} = \frac{1+\nu}{E}\sigma_\phi = m, \tag{B.6}$$

where m is the slope in the $\varepsilon_{\phi\psi}$- $sin^2\,\psi$ plot as shown schematically in Figure B.4.

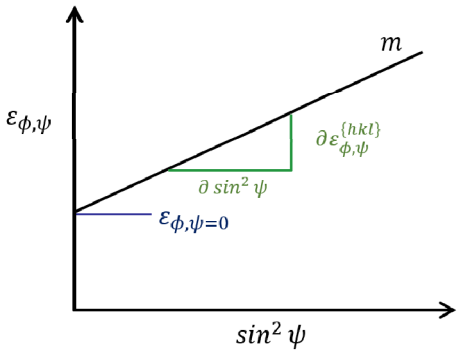


Figure B.4: The $\varepsilon_{\phi\psi}$- $\sin^2\,\psi$ plot obtained during the XRD-strain measurement of the sample with tensile biaxial residual stress. *After* [82].

Then we have

$$\sigma_\phi = \frac{mE}{1+\upsilon} \tag{B.7}$$

or

$$\sigma_\phi = \frac{E}{(1+\upsilon)\,sin^2\,\psi}\left(\frac{d_\psi - d_0}{d_0}\right). \tag{B.8}$$

This method is called the $sin^2\,\psi$ method and is often used for a determination of the residual stress according to the slope of the $\varepsilon_{\phi\psi}$- $sin^2\,\psi$ curve [82], [98].

More complex dependences of the strain on the ψ-angle are observed when the stress state deviates from ideal situations. In the case when the ε_{13} and/or ε_{23} are not zero, the splitting of the curve appears when the measurement is performed with an increasing or decreasing ψ-angle (see Figure B.5 a)). In the case of the stress gradient and/or composition gradient within the investigated material the $\varepsilon_{\phi,\psi}$-$sin^2\,\psi$ curve is non-linear, while it oscillates in the case of the textured film.

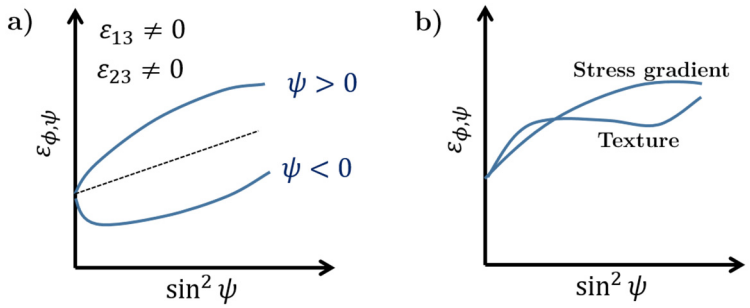


Figure B.5: The $\varepsilon_{\phi\psi}$- $\sin^2\,\psi$ curves for non-ideal situations. In the case a) ψ –splitting occurs due to the shear stress, while in the case b) the curve is non linear due to texture, stress gradient and/or composition gradient within the investigated material. *After* [82].

B.3 Strain and stress determination by the 2D-XRD

Two-dimensional (2D) XRD refers to X-ray diffraction with a 2D detector, corresponding 2D image processing and 2D diffraction pattern manipulation and interpretation. As presented in Figure B.6, for the 2D-XRD system, the incident X-ray beam lies along the rotation axis of the cones. The γ-angle is the angle from the origin in the 6 o'clock direction, with the rotation axis along the incident beam and is used to define the direction of the diffracted beam on the cone, while the ω-angle is the angle between the incident beam and the surface of the film [82], [98].

Diffracted beams from a polycrystalline material form a series of cones (diffraction rings), which correspond to a specific family of crystal planes. In the diffraction cones from an unstressed polycrystalline sample the 2θ is independent of the γ angle. When the material is under stress a change in d-spacings causes a shift in the diffraction patterns. In the case of the 2D detector the change is seen as the distortion of diffraction cones, as is schematically presented in Figure B.6 The 2θ for the stressed material then becomes a function of γ and the sample rotation [98]–[100].

An example of the 2D-XRD diffractogram obtained for a BST 50/50 film prepared on a polycrystalline alumina substrate is presented in Figure B.7 a). The conventional diffraction profile can be calculated from the 2D image by the integration within a given γ-range, as is schematically shown in Figure B.7 b). The 2θ peak position for each γ-range can be determined from the diffraction profile using one of the many available peak-fitting methods [82], [99].

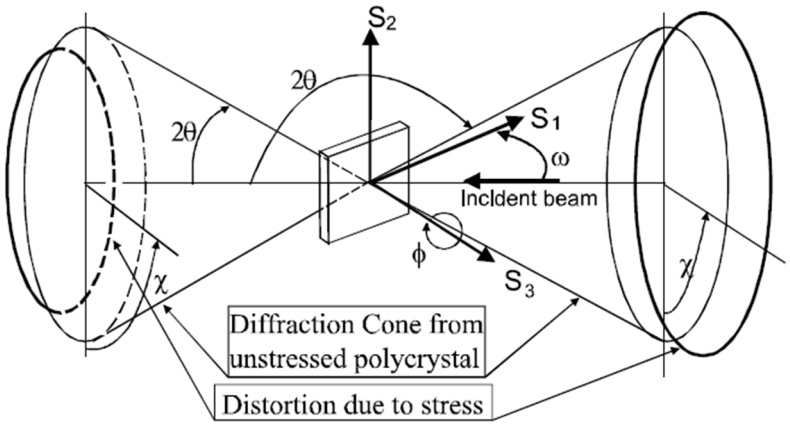


Figure B.6: Schematic presentation of a 2D-XRD system with diffraction cones from an unstressed polycrystalline sample and the diffraction cones, that are distorted by the stress [99].

Since in the case of the 2D XRD method a large part of the diffraction ring is used for the stress calculation it contains far more data points than a conventional diffraction pattern. The stress measurement is performed with a high sensitivity, high accuracy and requires much less time for data collection since a large portion of the diffraction ring is measured during each exposure. It is also a suitable method for samples with large grains or texture. However, the advantages of the 2D detector cannot be fully exploited if the data interpretation and analysis methods are simply inherited from the conventional XRD theory [100]. Therefore, the 2D fundamental equation, giving the relationship between the stress tensor and the diffraction cone distortion is needed, as is shown for the biaxial-stress-state example in the text below.

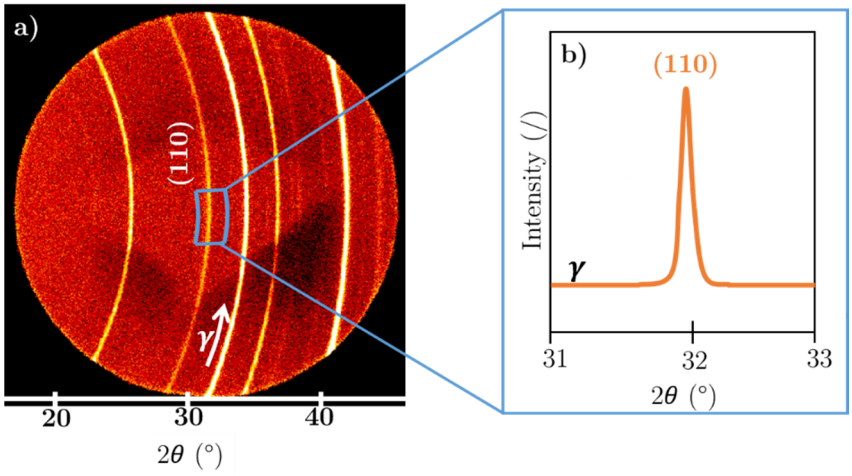


Figure B.7: a) Debye diffraction rings collected in a -62 ° to -116 ° γ-range using an area detector for a BST 50/50 film on a polycrystalline alumina substrate. b) Conventional XRD pattern in a narrow 2θ region around the (110) diffraction peak obtained with the integration within the shown γ-range.

One of the main sources of the error in the stress-determination using XRD is the inaccurate zero-stress value of the lattice parameter d_0 (or $2\theta_0$), which arises, for example, from the variation in composition. The faulty stress, caused by the error in the $2\theta_0$, can be intentionally introduced into the stress matrix (Eq. (B.1)). Since it is orientation independent it is referred to as the pseudohydrostatic stress σ_{ph} [82]. The stress tensor is then expressed as:

$$\sigma_{ij=}\begin{bmatrix}\sigma_{11} & \sigma_{12} & \sigma_{13}\\ \sigma_{21} & \sigma_{22} & \sigma_{23}\\ \sigma_{31} & \sigma_{32} & 0\end{bmatrix}+\begin{bmatrix}\sigma_{ph} & 0 & 0\\ 0 & \sigma_{ph} & 0\\ 0 & 0 & \sigma_{ph}\end{bmatrix}=\begin{bmatrix}\sigma_{11}+\sigma_{ph} & \sigma_{12} & \sigma_{13}\\ \sigma_{21} & \sigma_{22}+\sigma_{ph} & \sigma_{23}\\ \sigma_{31} & \sigma_{32} & \sigma_{ph}\end{bmatrix} \quad \text{(B.9)}$$

and the 2D fundamental equation under the equilibrium ($\sigma_{12}=\sigma_{21}$, $\sigma_{13}=\sigma_{31}$ and $\sigma_{23}=\sigma_{32}$), can be written as:

$$p_{11}(\sigma_{11}+\sigma_{ph})+p_{12}\sigma_{12}+p_{22}(\sigma_{22}+\sigma_{ph})+p_{13}\sigma_{13}+p_{23}\sigma_{23}+p_{33}(\sigma_{33}+\sigma_{ph})=ln(\tfrac{sin\,\theta_0}{sin\,\theta}), \quad \text{(B.10)}$$

where p_{ij} are the stress coefficients given by:

$$p_{ij}=\begin{cases}(1/E)(1+\nu)h_i^2-\nu) & if\ i=j\\ (1/E)(1+\nu)h_ih_j & if\ i\neq j\end{cases}. \quad \text{(B.11)}$$

The direction of the stress is given by the unit vector with the tensor components h_{ij}.

Since $\sigma_{33}=0$, the determined stress value in this direction corresponds to the pseudohydrostatic stress, representing an error and can be easily substracted from the total value (see Eq. (B.9)) [82].

In the case of the biaxial stress state the fundamental equation simplifies to:

$$p_{11}\sigma_{11}+p_{12}\sigma_{12}+p_{22}\sigma_{22}+p_{ph}\sigma_{ph}=ln(\tfrac{sin\,\theta_0}{sin\,\theta}), \quad \text{(B.12)}$$

and for the equi-biaxial stress to [82]:

$$(p_{11}+p_{22})\sigma+p_{ph}\sigma_{ph}=ln(\tfrac{sin\,\theta_0}{sin\,\theta}). \quad \text{(B.13)}$$

References

[1] P. Erhart, "Film deposition methods," in *Nanoelectronics and Information Technology Advanced Electronic Materials and Novel Devices*, 2nd ed., R. Waser, Ed. Winheim, Germany: WILEY-VCH Verlag GmbH & Co. KGaA, 2003, pp. 201–221.

[2] R. W. Schwartz, T. Schneller, R. Waser, and H. Dobberstein, "Chemical solution deposition of ferroelectric thin films," in *Chemical Processing of Ceramics*, 2nd ed., B. Lee and S. Komerneni, Eds. Boca Raton, Florida: Taylor & Francis Group, 2005, pp. 713–742.

[3] R. W. Schwartz, T. Schneller, and R. Waser, "Chemical solution deposition of electronic oxide films," *Comptes Rendus Chimie*, vol. 7, no. 5, pp. 433–461, 2004.

[4] R. W. Schwartz, "Chemical solution deposition of perovskite thin films," *Chemistry of Materials*, vol. 9, no. 11, pp. 2325–2340, 1997.

[5] C. J. Brinker and G. W. Scherer, *Sol Gel Science: The Physics and Chemistry of Sol-Gel Processing*. New York, USA: Academic Press, Inc., 1990.

[6] R. W. Schwartz, "Chemical solution deposition — basic principles," in *Solution Processing of Inorganic Materials*, D. M. Mitzi, Ed. New Jersey, USA: John Wiley & Sons, Inc., 2009, pp. 33–76.

[7] N. Bassiri-Gharb, Y. Bastani, and A. Bernal, "Chemical solution growth of ferroelectric oxide thin films and nanostructures," *Chemical Society Reviews*, vol. 43, no. 7, pp. 2125–2140, 2014.

[8] T. Schneller, "Simple alkoxide based precursor systems," in *Chemical Solution Deposition of Functional Oxide Thin Films*, T. Schneller, R. Waser, M. Kosec, and D. Payne, Eds. Wien, Austria: Springer-Verlag, 2013, pp. 3–28.

[9] T. Schneller and D. Griesche, "Carboxylate based precursor systems," in *Chemical Solution Deposition of Functional Oxide Thin Films*, T. Schneller, R. Waser, M. Kosec, and D. Payne, Eds. Wien, Austria: Springer-Verlag, 2013, pp. 29–49.

[10] B. Malič, S. Glinšek, T. Schneller, and M. Kosec, "Mixed metallo-organic precursor systems," in *Chemical Solution Deposition of Functional Oxide Thin Films*, T. Schneller, R. Waser, M. Kosec, and D. Payne, Eds. Wien, Austria: Springer-Verlag, 2013, pp. 51–69.

[11] D. P. Birnie III, "Spin coating: art and science," in *Chemical Solution Deposition of Functional Oxide Thin Films*, T. Schneller, R. Waser, M. Kosec, and D. Payne, Eds. Wien, Austria: Springer-Verlag, 2013, pp. 263–274.

[12] R. W. Schwartz and M. Narayanan, "Thermodynamics and heating processes," in *Chemical Solution Deposition of Functional Oxide Thin Films*, T. Schneller, R.

Waser, M. Kosec, and D. Payne, Eds. Wien, Austria: Springer-Verlag, 2013, pp. 343–382.

[13] J. W. Mullin, *Crystallization*, 4th ed. Oxford, England: Butterworth-Heinemann, 2001.

[14] C. V. Thompson, "Grain growth in thin films," *Annual Review of Materials Science*, vol. 20, pp. 245–268, 1990.

[15] C. V. Thompson, "Structure evolution during processing of polycrystalline films," *Annual Review of Materials Science*, vol. 30, pp. 159–190, 2000.

[16] W. D. Kingery, H. K. Bowen, and D. R. Uhlmann, "Grain Growth, Sintering, and Vitrification," in *Introduction to ceramics*, 2nd ed., W. D. Kingery, H. K. Bowen, and D. R. Uhlmann, Eds. New York, USA: John Wiley & Sons, Inc., 1976, pp. 448–515.

[17] R. W. Schwartz, P. G. Clem, J. A. Voigt, E. R. Byhoff, M. Van Stry, T. J. Headley, and N. A. Missert, "Control of microstructure and orientation in solution-deposited $BaTiO_3$ and $SrTiO_3$ thin films," *Journal of the American Ceramic Society*, vol. 82, no. 9, pp. 2359–2367, 1999.

[18] B. Malič, M. Mandeljc, G. Dražić, M. Škarabot, I. Muševič, and M. Kosec, "Strategy for low-temperature crystallization of titanium-rich PZT thin films by chemical solution deposition," *Integrated Ferroelectrics*, vol. 100, no. 1, pp. 285–296, 2008.

[19] C. V. Thompson, "Secondary grain growth in thin films of semiconductors: theoretical aspects," *Journal of Applied Physics*, vol. 58, no. 2, pp. 763–772, 1985.

[20] W. W. Mullins, "The effect of thermal grooving on grain boundary motion," *Acta Metallurgica*, vol. 6, no. 6, pp. 414–427, 1958.

[21] J. E. Palmer, C. V. Thompson, and H. I. Smith, "Grain growth and grain size distributions in thin germanium films," *Journal of Applied Physics*, vol. 62, no. 6, pp. 2492–2497, 1987.

[22] M. Stech, P. Reynders, and J. Rödel, "Constrained film sintering of nanocrystalline TiO_2," *Journal of the American Ceramic Society*, vol. 83, no. 8, pp. 1889–1896, 2000.

[23] M. J. Rost, D. A. Quist, and J. W. M. Frenken, "Grains, growth, and grooving," *Physical Review Letters*, vol. 91, no. 2, pp. 026101–1–4, 2003.

[24] H. J. Frost, C. V. Thompson, and D. T. Walton, "Simulation of thin film grain structures-I. Grain growth stagnation," *Acta Metallurgica et Materialia*, vol. 38, no. 8, pp. 1455–1462, 1990.

[25] J. H. Brophy, R. M. Rose, and J. Wulff, *Structure and Properties of Materials: Thermodynamics of Structure*. New York, USA: John Wiley & Sons, Inc., 1964.

[26] J. A. Thornton, "High rate thick film growth," *Annual Review of Material Science*, vol. 7, pp. 239–260, 1977.

[27] J. A. Thornton, "Influence of apparatus geometry and deposition conditions on the structure and topography of thick sputtered coatings," *Journal of Vacuum Science and Technology*, vol. 11, no. 4, pp. 666–670, 1974.

[28] T. Schuler, T. Krajewski, I. Grobelsek, and M. A. Aegerter, "A microstructural zone model for the morphology of sol-gel coatings," *Journal of Sol-Gel Science and Technology*, vol. 31, no. 1, pp. 235–239, 2004.

[29] T. Schuler, T. Krajewski, I. Grobelsek, and M. A. Aegerter, "Influence of structure zone model parameters on the electrical properties of ZnO:Al sol-gel coatings," *Thin Solid Films*, vol. 502, no. 1–2, pp. 67–71, 2006.

[30] J. A. Basmajian and R. C. Devries, "Phase equilibria in the system $BaTiO_3$-$SrTiO_3$," *Journal of American Ceramic Society*, vol. 40, no. 11, pp. 373–376, 1957.

[31] S. Gevorgian, *Ferroelectrics in Microwave Devices, Circuits and Systems: Physics, Modelling, Fabrication and Measurements*. London, England: Springer-Verlag, 2009.

[32] D. Damjanovic, "Ferroelectric, dielectric and piezoelectric properties of ferroelectric thin films and ceramics," *Reports on Progress in Physics*, vol. 61, pp. 1267–1324, 1998.

[33] B. Jaffe, W. R. Cook, and H. Jaffe, "Barium Titanate," in *Piezoelectric Ceramics*, J. P. Roberts and P. Popper, Eds. London: Academic Press, Inc., 1971, pp. 53–114.

[34] J. H. Haeni, P. Irvin, W. Chang, R. Uecker, P. Reiche, Y. L. Li, S. Choudhury, W. Tian, M. E. Hawley, B. Craigo, a K. Tagantsev, X. Q. Pan, S. K. Streiffer, L. Q. Chen, S. W. Kirchoefer, J. Levy, and D. G. Schlom, "Room-temperature ferroelectricity in strained $SrTiO_3$," *Nature*, vol. 430, pp. 758–761, 2004.

[35] V. Skoromets, S. Glinšek, V. Bovtun, M. Kempa, J. Petzelt, S. Kamba, B. Malič, M. Kosec, and P. Kužel, "Ferroelectric phase transition in polycrystalline $KTaO_3$ thin film revealed by terahertz spectroscopy," *Applied Physics Letters*, vol. 99, no. 5, pp. 052908–1–3, 2011.

[36] T. Mitsui, S. Nomura, M. Adachi, J. Harada, T. Ikeda, E. Nakamura, E. Sawaguchi, T. Shigenari, Y. Shiozoaki, I. Tatsuzaki, K. Toyoda, T. Yamada, K. Gesi, Y. Makita, M. Marutake, T. Shisoaki, and K. Wakino, *Landolt-Bornstein. Numerical Data and Funtional Relationships in Science and Technology. Group III: Crystal and Solid State Physics. Ferroelectrics and Related Substances: Oxides*. Berlin, Germany: Springer-Verlag, 1981.

[37] M. J. Lancaster, J. Powell, and A. Porch, "Thin-film ferroelectric microwave devices," *Superconductor Science and Technology*, vol. 11, no. 11, pp. 1323–1334, 1999.

[38] A. K. Tagantsev, V. O. Sherman, K. F. Astafiev, J. Venkatesh, and N. Setter, "Ferroelectric Materials for Microwave Tunable Applications," *Journal of Electroceramics*, vol. 11, no. 1, pp. 5–66, 2004.

[39] P. Bao, T. J. Jackson, X. Wang, and M. J. Lancaster, "Barium strontium titanate thin film varactors for room-temperature microwave device applications," *Journal of Physics D: Applied Physics*, vol. 41, no. 6, pp. 063001–1–21, 2008.

[40] W. Lee, H. Kim, S. Yoon, W. Lee, and H. Kim, "Microstructure dependence of electrical properties of $Ba_{0.5}Sr_{0.5}TiO_3$," *Journal of Applied Physics*, vol. 80, no. 10, pp. 5891–5894, 1996.

[41] P. Padmini, T. R. Taylor, M. J. Lefevre, A. S. Nagra, R. A. York, and J. S. Speck, "Realization of high tunability barium strontium titanate thin films by rf magnetron sputtering," *Applied Physics Letters*, vol. 75, no. 20, pp. 3186–3188, 1999.

[42] T. R. Taylor, P. J. Hansen, B. Acikel, N. Pervez, R. A. York, S. K. Streiffer, and J. S. Speck, "Impact of thermal strain on the dielectric constant of sputtered barium strontium titanate thin films," *Applied Physics Letters*, vol. 80, no. 11, pp. 1978–

1980, 2002.

[43] N. K. Pervez, P. J. Hansen, and R. A. York, "High tunability barium strontium titanate thin films for rf circuit applications," *Applied Physics Letters*, vol. 85, no. 2004, pp. 4451–4453, 2004.

[44] S. Ito, H. Funakubo, I. P. Koutsaroff, M. Zelner, and A. Cervin-Lawry, "Effect of the thermal expansion matching on the dielectric tunability of (100)-one-axis-oriented $(Ba_{0.5}Sr_{0.5})TiO_3$," *Applied Physics Letters*, vol. 90, no. 14, pp. 142910–1–3, 2007.

[45] C. B. Parker, J. P. Maria, and A. I. Kingon, "Temperature and thickness dependent permittivity of (Ba,Sr)TiO_3 thin films," *Applied Physics Letters*, vol. 81, no. 2, pp. 340–342, 2002.

[46] L. J. Sinnamon, M. M. Saad, R. M. Bowman, and J. M. Gregg, "Exploring grain size as a cause for 'dead-layer' effects in thin film capacitors," *Applied Physics Letters*, vol. 81, no. 4, pp. 703–705, 2002.

[47] S. E. Moon, E. K. Kim, M. H. Kwak, H. C. Ryu, Y. T. Kim, K. Y. Kang, S. J. Lee, and W. J. Kim, "Orientation dependent microwave dielectric properties of ferroelectric $Ba_{1-x}Sr_xTiO_3$ thin films," *Applied Physics Letters*, vol. 83, no. 11, pp. 2166–2168, 2003.

[48] E. A. Fardin, A. S. Holland, K. Ghorbani, E. K. Akdogan, W. K. Simon, A. Safari, and J. Y. Wang, "Polycrystalline $Ba_{0.6}Sr_{0.4}TiO_3$ thin films on r-plane sapphire: Effect of film thickness on strain and dielectric properties," *Applied Physics Letters*, vol. 89, no. 18, pp. 182907–1–3, 2006.

[49] M. C. Gust, N. D. Evans, L. A. Momoda, and M. L. Mecartney, "In-situ transmission electron microscopy crystallization studies of sol – gel-derived barium titanate thin films," *Journal of the American Ceramic Society*, vol. 80, no. 11, pp. 2828–2836, 1997.

[50] S. Hoffmann and R. Waser, "Control of the morphology of CSD-prepared (Ba,Sr)TiO_3 thin films," *Journal of the European Ceramic Society*, vol. 19, no. 6–7, pp. 1339–1343, 1999.

[51] M. C. Gust, L. A. Momoda, N. D. Evans, and M. L. Mecartney, "Crystallization of sol–gel-derived barium strontium titanate thin films," *Journal of the American Ceramic Society*, vol. 84, no. 5, pp. 1087–1092, 2001.

[52] J. T. Dawley and P. G. Clem, "Dielectric properties of random and <100> oriented $SrTiO_3$ and (Ba,Sr)TiO_3 thin films fabricated on <100> nickel tapes," *Applied Physics Letters*, vol. 81, no. 16, pp. 3028–3030, 2002.

[53] B. Malič, I. Boerasu, M. Mandeljc, M. Kosec, V. Sherman, T. Yamada, N. Setter, and M. Vukadinovic, "Processing and dielectric characterization of $Ba_{0.3}Sr_{0.7}TiO_3$ thin films on alumina substrates," *Journal of the European Ceramic Society*, vol. 27, no. 8–9, pp. 2945–2948, 2007.

[54] S. M. Aygün, P. Daniels, W. Borland, and J. P. Maria, "In situ methods to explore microstructure evolution in CSD thin films," *Journal of Materials Research*, vol. 25, no. 3, pp. 427–436, 2009.

[55] K. Kageyama, T. Hosokura, T. Nakaiso, and H. Takagi, "Dielectric properties of (Ba,Sr)TiO_3 thin films with varied microstructures prepared by the chemical

solution deposition method for thin-film capacitors and ferroelectric varactors.," *IEEE transactions on ultrasonics, ferroelectrics, and frequency control*, vol. 57, no. 10, pp. 2198–204, 2010.

[56] S. M. Aygün, J. F. Ihlefeld, W. J. Borland, and J.-P. Maria, "Permittivity scaling in $Ba_{1-x}Sr_xTiO_3$ thin films and ceramics," *Journal of Applied Physics*, vol. 109, no. 3, pp. 034108–1–5, 2011.

[57] D. Levasseur, H. B. El-Shaarawi, S. Pacchini, A. Rousseau, S. Payan, G. Guegan, and M. Maglione, "Systematic investigation of the annealing temperature and composition effects on the dielectric properties of sol–gel $Ba_xSr_{1-x}TiO_3$ thin films," *Journal of the European Ceramic Society*, vol. 33, no. 1, pp. 139–146, 2013.

[58] U. Hasenkox, S. Hoffmann, and R. Waser, "Influence of Precursor Chemistry on the Formation of $MTiO_3$ (M=Ba,Sr) Ceramic Thin Films," *Journal of Sol-Gel Science and Technology*, vol. 12, pp. 67–79, 1998.

[59] S. Jang, B. Choi, and H. M. Jang, "Phase-formation kinetics of xerogel and electrical properties of sol-gel-derived $Ba_xSr_{1-x}TiO_3$ thin films," *Journal of Materials Research*, vol. 12, no. 5, pp. 1327–1334, 1997.

[60] S. Halder, T. Schneller, and R. Waser, "Crystallization temperature limit of (Ba,Sr)TiO_3 thin films prepared by a non oxocarbonate phase forming CSD route," *Journal of Sol-Gel Science and Technology*, vol. 33, no. 3, pp. 299–306, 2005.

[61] F. M. Pontes, E. Longo, E. R. Leite, and J. A. Varela, "Study of the dielectric and ferroelectric properties of chemically processed $Ba_xSr_{1-x}TiO_3$ thin films," *Thin Solid Films*, vol. 386, no. 1, pp. 91–98, 2001.

[62] C. Jia and K. Urban, "Microstructure of columnar-grained $SrTiO_3$ and $BaTiO_3$ thin films prepared by chemical solution deposition," *Journal of Materials Research*, vol. 13, no. 8, pp. 2206–2217, 1998.

[63] M. H. Frey, Z. Xu, P. Han, and D. A. Payne, "The role of interfaces on an apparent grain size effect on the dielectric properties for ferroelectric barium titanate ceramics," *Ferroelectrics*, vol. 206–207, pp. 337–353, 1998.

[64] J. Petzelt, "Dielectric grain-size effect in high-permittivity ceramics," *Ferroelectrics*, vol. 400, no. 1, pp. 117–134, 2010.

[65] K. Kageyama, A. Sakurai, A. Ando, and Y. Sakabe, "Thickness effects on microwave properties of (Ba,Sr)TiO_3 films for frequency agile technologies," *Journal of the European Ceramic Society*, vol. 26, no. 10–11, pp. 1873–1877, 2006.

[66] J. F. Ihlefeld, W. J. Borland, and J.-P. Maria, "Synthesis and properties of barium titanate thin films on copper substrates," *Materials Research Society Symposium Proceedings*, vol. 905, pp. 1–11, 2006.

[67] J. F. Ihlefeld, A. M. Vodnick, S. P. Baker, W. J. Borland, and J.-P. Maria, "Extrinsic scaling effects on the dielectric response of ferroelectric thin films," *Journal of Applied Physics*, vol. 103, no. 7, pp. 074112–1–6, 2008.

[68] T. Horikawa, "Dielectric properties of $(Ba_xSr_{1-x})TiO_3$ thin films deposited by RF sputtering," *Japanese Journal of Applied Physics*, vol. 32, no. 9B, pp. 4126–4130, 1993.

[69] T. Ostapchuk, J. Petzelt, I. Rychetský, V. Porokhonskyy, B. Malič, M. Kosec, and P. Vilarinho, "Influence of porosity on the dielectric response and central-mode

dynamics in $PbZrO_3$ ceramics," *Ferroelectrics*, vol. 298, no. 1, pp. 211–218, 2004.

[70] E. R. Leite, A. M. Scotch, A. Khan, T. Li, H. M. Chan, M. P. Harmer, S. F. Liu, and S. E. Park, "Chemical heterogeneity in PMN-35PT ceramics and effects on dielectric and piezoelectric properties," *Journal of the American Ceramic Society*, vol. 85, no. 12, pp. 3018–3024, 2002.

[71] S. Ito, K. Takahashi, S. Okamoto, I. P. Koutsaroff, A. Cervin-Lawry, and H. Funakubo, "Orientation dependence of epitaxial and one-axis-oriented $(Ba_{0.5}Sr_{0.5})TiO_3$ films prepared by RF magnetron sputtering," *Japanese Journal of Applied Physics*, vol. 44, no. 9B, pp. 6881–6884, 2005.

[72] G. Han, J. Ryu, W.-H. Yoon, J.-J. Choi, B.-D. Hahn, J.-W. Kim, D.-S. Park, C. W. Ahn, S. Priya, and D.-Y. Jeong, "Stress-controlled $Pb(Zr_{0.52}Ti_{0.48})O_3$ thick films by thermal expansion mismatch between substrate and $Pb(Zr_{0.52}Ti_{0.48})O_3$ film," *Journal of Applied Physics*, vol. 110, no. 12, pp. 124101–1–5, 2011.

[73] T. M. Shaw, Z. Suo, M. Huang, E. Liniger, R. B. Laibowitz, and J. D. Baniecki, "The effect of stress on the dielectric properties of barium strontium titanate thin films," *Applied Physics Letters*, vol. 75, no. 14, pp. 2129–2131, 1999.

[74] L. B. Freund and S. Suresh, *Thin Film Materials: Stress, Defect Formation and Surface Evolution*. Cambridge, England: Cambridge University Press, 2003.

[75] A. Sharma, Z.-G. Ban, S. P. Alpay, and J. V. Mantese, "The role of thermally-induced internal stresses on the tunability of textured barium strontium titanate films," *Applied Physics Letters*, vol. 85, no. 6, pp. 985–987, 2004.

[76] B. Malič, "Alkoksidna sol-gel sinteza materialov v sistemu PbO-ZrO_2-TiO_2," Doctoral dissertation, University of Ljubljana, Ljubljana, 1995.

[77] "Polished Substrates For Thin FIlm Applications," 2015. [Online]. Available: http://www.coorstek.com/resource-library/library/8510-1083_polished_substrates.pdf. [Accessed: 01-Dec-2015].

[78] "PDF 01-071-1241." JCPDS-International Center for Diffraction Data, Newton Square, 2002.

[79] "PDF 00-039-1395." JCPDS-International Center for Diffraction Data, Newton Square, 2002.

[80] "PDF-ICDD, PCPDFWin Version 2.2, International Center for Diffraction Data, 2002." .

[81] F. K. Lotgering, "Topotactical reactions with ferrimagnetic oxides having hexagonal crystal structures—I," *Journal of Inorganic and Nuclear Chemistry*, vol. 9, no. 2, pp. 113–123, 1959.

[82] B. B. He, "Stress Measurements," in *Two-Dimensional X-Ray Diffraction*, 1st ed., B. B. He, Ed. Hoboken, USA: John Wiley & Sons, 2009, pp. 249–328.

[83] T. H. Fang, W. J. Chang, C. M. Lin, L. W. Ji, Y. S. Chang, and Y. J. Hsiao, "Effect of annealing on the structural and mechanical properties of $Ba_{0.7}Sr_{0.3}TiO_3$ thin films," *Materials Science and Engineering A*, vol. 426, no. 1, pp. 157–161, 2006.

[84] O. G. Vendik, S. P. Zubko, and M. A. Nikol'skii, "Modeling and calculation of the capacitance of a planar capacitor containing a ferroelectric thin film," *Technical Physics*, vol. 44, no. 4, pp. 349–355, 1999.

[85] M. Vukadinovič, B. Malič, M. Kosec, and D. Križaj, "Modelling and characterization

of thin film planar capacitors: inherent errors and limits of applicability of partial capacitance methods," *Measurement Science and Technology*, vol. 20, no. 11, pp. 115106–1–11, 2009.

[86] C. D. Easton, M. V Jacob, and J. Krupka, "Non-destructive complex permittivity measurement of low permittivity thin film materials," *Measurement Science and Technology*, vol. 18, no. 9, pp. 2869–2877, 2007.

[87] Z. G. Ban and S. P. Alpay, "Phase diagrams and dielectric response of epitaxial barium strontium titanate films: A theoretical analysis," *Journal of Applied Physics*, vol. 91, no. 11, pp. 9288–9296, 2002.

[88] I. Rychetský, J. Petzelt, and T. Ostapchuk, "Grain-boundary and crack effects on the dielectric response of high-permittivity films and ceramics," *Journal of Applied Physics*, vol. 81, p. 4224, 2002.

[89] O. G. Vendik and S. P. Zubko, "Ferroelectric phase transition and maximum dielectric permittivity of displacement type ferroelectrics ($Ba_xSr_{1-x}TiO_3$)," *Journal of Applied Physics*, vol. 88, no. 9, pp. 5343–5350, 2000.

[90] N. A. Pertsev, A. G. Zembilgotov, and A. K. Tagantsev, "Effect of mechanical boundary conditions on phase diagrams of epitaxial ferroelectric thin films," *Physical Review Letters*, vol. 80, no. 9, pp. 1988–1991, 1998.

[91] D. T. Harris, M. J. Burch, J. F. Ihlefeld, P. G. Lam, J. Li, E. C. Dickey, and J. P. Maria, "Realizing strain enhanced dielectric properties in $BaTiO_3$ films by liquid phase assisted growth," *Applied Physics Letters*, vol. 103, no. 1, pp. 012904–1–5, 2013.

[92] X. H. Zhu, L. P. Yong, H. F. Tian, W. Peng, J. Q. Li, and D. N. Zheng, "The origin of the weak ferroelectric-like hysteresis effect in paraelectric $Ba_{0.5}Sr_{0.5}TiO_3$ thin films grown epitaxially on $LaAlO_3$," *Journal of Physics: Condensed Matter*, vol. 18, no. 19, pp. 4709–4718, 2006.

[93] F. Pontes, E. Leite, and E. Longo, "Effects of the postannealing atmosphere on the dielectric properties of (Ba,Sr)TiO_3 capacitors: Evidence of an interfacial space charge layer," *Applied Physics Letters*, vol. 76, no. 2000, pp. 2433–2435, 2000.

[94] H. W. Jang, A. Kumar, S. Denev, M. D. Biegalski, P. Maksymovych, C. W. Bark, C. T. Nelson, C. M. Folkman, S. H. Baek, N. Balke, C. M. Brooks, D. A. Tenne, D. G. Schlom, L. Q. Chen, X. Q. Pan, S. V. Kalinin, V. Gopalan, and C. B. Eom, "Ferroelectricity in strain-free $SrTiO_3$ thin films," *Physical Review Letters*, vol. 104, no. 19, pp. 197601–1–4, 2010.

[95] M. Peterkovič, "Influence of the annealing conditions on the microstructure of solution-derived $Ba_{0.5}Sr_{0.5}TiO_3$ thin films," Diploma thesis, University of Ljubljana, Ljubljana, 2015.

[96] A. C. Dippel, T. Schneller, P. Gerber, and R. Waser, "Morphology control of highly-transparent indium tin oxide thin films prepared by a chlorine-reduced metallo-organic decomposition technique," *Thin Solid Films*, vol. 515, no. 7–8, pp. 3797–3801, 2007.

[97] G. K. Williamson and W. H. Hall, "X-ray line broadening from filed aluminium and wolfram," *Acta Metallurgica*, vol. 1, no. 1, pp. 22–31, 1953.

[98] M. Fitzpatrick, A. Fry, P. Holdway, F. Kandil, J. Shackleton, and L. Suominen,

"Determination of Residual Stresses by X-ray Diffraction - Issue 2," *Measurement Good Practice Guide No. 52*, 2005. [Online]. Available: http://www.npl.co.uk/upload/pdf/Determination_of_Residual_Stresses_by_X-ray_Diffraction_-_Issue_2.pdf. [Accessed: 01-Oct-2014].

[99] B. B. He and S. L. Kingsley, "Strain and Stress Measurements with a Two-Dimensional Detector," *JCPDS-International Centre for Diffraction Data 1999*, pp. 501–508, 1999.

[100] B. B. He, U. Preckwinkel, and S. L. Kingsley, "Fundamentals of two-dimensional X-ray diffraction (XRD^2)," *JCPDS-International Centre for Diffraction Data 2000, Advances in X-ray Analysis*, vol. 43, pp. 1–7, 2009.

Bibliography

Publications Related to the Thesis

Journal Articles

S. Glinšek, T. Pečnik, V. Cindro, B. Kmet, B. Rožič and B. Malič, "Role of the microstructure in the neutron and gamma-ray irradiation stability of solution-derived $Ba_{0.5}Sr_{0.5}TiO_3$ thin films", *Acta materialia,* vol. 88, pp. 34-40, 2015.

V. Furlan, S. Glinšek, B. Kmet, T. Pečnik, B. Malič and M. Vidmar, "Influence of numerical method and geometry used by Maxwell's equation solvers on simulations of ferroelectric thin-film capacitors", *IEEE Transactions on Evolutionary Computation,* vol. 63, no. 3, pp. 891-896, 2015.

T. Pečnik, S. Glinšek, B. Kmet, B. Malič, "Combined effects of thickness, grain size and residual stress on the dielectric properties of $Ba_{0.5}Sr_{0.5}TiO_3$ thin films", *Journal of alloys and compounds,* vol. 646, pp. 766-772, 2015.

T. Pečnik, A. Eršte, A. Matavž, V. Bobnar, M. Ivanov, J. Banys, F. Xiang, Hong Wang, B. Malič and S. Glinšek, " Dielectric dynamics of the polycrystalline $Ba_{0.5}Sr_{0.5}TiO_3$ thin films", *Europhysics Letters,* vol. 114, no. 4, pp. 47009-p1-p5, 2016.

Published scientific conference paper

T. Pečnik, S. Glinšek, B. Kmet and B. Malič, "Microstructure and kHz- and GHz- range dielectric properties of polycrystalline $Ba_{0.5}Sr_{0.5}TiO_3$ thin films," in *International Ultrasonics Symposium (IUS), Joint IEEE International Symposium on the Applications of Ferroelectrics (ISAF) and Piezoresponse Force Microscopy and Nanoscale Phenomena in Polar Materials (PMF), Joint International Frequency Control Symposium (IFCS) and European Frequency and Time Forum (EFTF),* Prague, Czech Republic*:* Joint UFFC, EFTF and PFM Symposium, 2013.

T. Pečnik, S. Glinšek, B. Kmet, R. C. Frunză, and B. Malič, "Solution derived $Ba_{0.5}Sr_{0.5}TiO_3$ thin films on polycrystalline alumina substrates," in *49th International Conference on Microelectronics, Devices and Materials & theWorkshop on Digital Electronic Systems, Proceedings*, Kranjska Gora, Slovenia: MIDEM - Society for Microelectronics, Electronic Components and Materials, 2013.

T. Pečnik, S. Glinšek, B. Kmet and B. Malič, "Microstructure and dielectric properties of $Ba_xSr_{1-x}TiO_3$ (x=0.5-0.3) thin films," in *50th International Conference on Microelectronics, Devices and Materials, Proceedings, Ljubljana Slovenia:* MIDEM - Society for Microelectronics, Electronic Components and Materials, 2014.

Published scientific conference contribution - abstract

T. Pečnik, S. Glinšek, B. Kmet and B. Malič, "Microstructure and kHz- and GHz- range dielectric properties of polycrystalline $Ba_{0.5}Sr_{0.5}TiO_3$ thin films," in *International Ultrasonics Symposium (IUS), Joint IEEE International Symposium on the Applications of Ferroelectrics (ISAF) and Piezoresponse Force Microscopy and Nanoscale Phenomena in Polar Materials (PMF), Joint International Frequency Control Symposium (IFCS) and European Frequency and Time Forum (EFTF),* Prague, Czech Republic: Joint UFFC, EFTF and PFM Symposium, 2013.

B. Malič, S. Glinšek, B. Kmet, T. Pečnik, V. Furlan and M. Vidmar, "Microstructure and dielectric properties of solution-derived $Ba_{0.5}Sr_{0.5}TiO_3$ thin film varactors for microwave patch antenna", in *Materials Science & Technology 2013, Montreal, Quebec, Canada:* The American Ceramic Society, 2013.

T. Pečnik, S. Glinšek, B. Kmet, R. C. Frunză, and B. Malič, "Solution derived $Ba_{0.5}Sr_{0.5}TiO_3$ thin films on polycrystalline alumina substrates," in *49th International Conference on Microelectronics, Devices and Materials & theWorkshop on Digital Electronic Systems, Proceedings*, Kranjska Gora, Slovenia: MIDEM - Society for Microelectronics, Electronic Components and Materials, 2013.

T. Pečnik, S. Glinšek, B. Kmet, R. C. Frunză, and B. Malič, "Microstructural analysis of $Ba_{0.5}Sr_{0.5}TiO_3$ thin films on polycrystalline alumina," in *Workshop of all working groups: "Advances in Ferroelectric and Multiferroics" of the MP0904 COST action: Single-and multiphase ferroeics and multiferoics with restricted geometries,* Praque, Czech Republic: Academy of Sciences of the Czech Republic, 2013.

T. Pečnik, S. Glinšek, B. Kmet, M. Ivanov, J. Banys and B. Malič, "Influence of microstructure and dilectric properties of solution derived $Ba_{0.5}Sr_{0.5}TiO_3$ thin films," in *COST MP0904 Single- and Multiphase Ferroics and multiferroics with restricted geometries (SIMUFER), Book of abstracts,* Genoa, Italy: CNR-IENI = Institute for Energetics and Interphases, 2014.

T. Pečnik, S. Glinšek, B. Kmet and B. Malič, "Effect of film thickness on microstructure and dielectric properties of $Ba_{0.5}Sr_{0.5}TiO_3$ thin films prepared by chemical solution deposition," in *E-MRS 2014 Spring Meeting,* Lille, France: European Materials Research Society, 2014.

B. Malič, S. Glinšek, B. Kmet, T. Pečnik, V. Furlan and M. Vidmar, "$Ba_{0.5}Sr_{0.5}TiO_3$ thin film capacitors for microwave antenna," in *Electronic Materials and Applications 2014, EMA 2014,* Orlano, Florida: The American Ceramic Society, 2014.

T. Pečnik, S. Glinšek, B. Kmet, R. C. Frunză, and B. Malič,"Analysis of microstructure of $Ba_{0.5}Sr_{0.5}TiO_3$ thin films on polycrystalline alumina," in *8th Young Researchers' Day, Program and abstract book,* Ljubljana Slovenia: Institut Jožef Stefan, 2014.

T. Pečnik, S. Glinšek, B. Kmet and B. Malič, "Influence of the rapid thermal annealing temperature on the microstructure and dielectric properties of solution-derived $Ba_{0.5}Sr_{0.5}TiO_3$ thin films," in *9th Young researchers' day, Program and abstract book,* Ljubljana Slovenia: Institut Jožef Stefan, 2015.

T. Pečnik, S. Glinšek and B. Malič, "Effect of the rapid thermal annealing temperature on the microstucture and dielectric properties of solutin-derived $Ba_{0.5}Sr_{0.5}TiO_3$ thin films," in *[MP1308 COST action] TO-BE Spring meeting 2015, Book of abstracts,* Aveiro, Portugal: Universidade de Aveiro, 2015.

T. Pečnik, S. Glinšek and B. Malič, "Tayloring the microstructure and dielectric properties of solution-derived $Ba_{0.5}Sr_{0.5}TiO_3$ thin films," in *Piezo 2015: Electroceramics for End-Users VIII, Program,* Maribor, Slovenia, 2015.

T. Pečnik, S. Glinšek, B. Kmet and B. Malič, "Dielectric properties of the solution-derived $Ba_{0.5}Sr_{0.5}TiO_3$ thin films," in *23rd International Conference on Materials and Technology, Program and book of abstracts,* Portorož, Slovenia: Inštitut za kovinske materiale in tehnologije, 2015.

Invited lecture at foreign university

T. Pečnik**,** »Solution-derived $Ba_{0.5}Sr_{0.5}TiO_3$ thin films«, Vilnius: Vilnius University, Faculty of Physics, 2013.

Biography

I was born on the 10th of January 1989 in Maribor. After finishing the Gymnasium in Ruše in 2007 I enrolled in the Chemical Technology programme at the Faculty of Chemistry and Chemical Engineering, University of Maribor, Slovenia. In 2010 I started receiving a "Jožef Stefan" Institute scholarship. In 2011 I did the student practice at the Electronic Ceramics Department and graduated in July 2012. The diploma thesis entitled "*Crystallization and evolution of microstructure of $K_{0.5}Na_{0.5}NbO_3$ – $SrTiO_3$ thin films prepared by chemical solution deposition*" was also carried out at the Electronic Ceramics Department, under the supervision of Prof. Barbara Malič. In December 2012 I started to work as a Young Researcher at the "Jožef Stefan" Institute and enrolled in the Nanosciences and Nanotechnologies postgraduate programme at the Jožef Stefan International Postgraduate School. My research at the Institute mainly focuses on the preparation of solution-derived alkaline-earth titanate thin films, characterization of microstructure and dielectric properties.

Attendance at workshops and courses:

- "Workshop on Structural Characterization", CoE Namaste, Rogla, Slovenia, 7. – 8. 11. 2011 .
- "Single and multiphase ferroics and multiferroics with restricted geometries" workshop at the Institute of Physics AS CR, Prague, Czech Republic, July 21, 2013.
- "Adhesion Science and Technology Course" in Bled, Slovenia, 2. - 3. 12. 2013.
- Visit to the Faculty of Physics during "Short Term Scientific Mission" (COST MP0904) at the Vilnius University, Vilnius, Lithuania, 10. 11. - 23. 11. 2013.
- "Radio communications", a three-day course at the Faculty of Electrical Engineering, University of Ljubljana, Ljubljana, Slovenia, 24. - 26. 9. 2014.

Award:
Best oral presentation of work entitled *Dielectric Properties of the Solution-Derived $Ba_{0.5}Sr_{0.5}TiO_3$ Thin Films,* given in the frame of 23rd International Conference on Materials and Technology, Portorož, September, 2015.